

# University of St Andrews



Full metadata for this thesis is available in  
St Andrews Research Repository  
at:

<http://research-repository.st-andrews.ac.uk/>

This thesis is protected by original copyright

INFRARED STUDIES OF SEMICONDUCTORS

A thesis presented by  
Melinda Holtzman  
to the  
University of St. Andrews  
in application for the Degree of  
Master of Science.



Th  
9617

### Declaration

I hereby certify that this thesis has been composed by me, and is a record of work done by me, and has not previously been presented for a Higher Degree. The research was carried out in the Physical Sciences Laboratory of St. Salvator's College, in the University of St. Andrews, under the supervision of Professor R. A. Stradling.

I certify that Melinda Holtzman has spent seven terms research work in the laboratories of the School of Physical Science, University of St. Andrews, under my direction, that she has fulfilled the conditions of the Resolution of the University Court, 1974, No. 2, and that she is qualified to submit the accompanying thesis in application for the Degree of Master of Science.

Research Supervisor

## Table of Contents

Page	i.	Abstract
	1.	Section I: Introduction
	8.	Section II: Background theory
	26.	Section III: Experimental methods
	31.	Section IV: Results on cyclotron emission in germanium
	49.	Section V: Cyclotron resonance experiments
	58.	Section VI: Comparison of linewidths in cyclotron emission and absorption
	64.	Section VII: Laser annealing
	72.	Section VIII: Experiments in laser annealing
	92.	Section IX: Conclusion
	94.	Appendix A
	96.	References

## Abstract

Cyclotron emission experiments are carried out on germanium and some III-V compounds. A pulsed electric field excites electrons into the upper Landau levels of a semiconductor in a magnetic field by impact ionization, and emission is observed as the electrons relax back to the lower levels by radiative transitions. The emission is observed with a GaAs narrowband photoconductive detector. The relation of intensity and linewidth with electric field is studied. The narrowest linewidth obtained, in a germanium sample with an impurity concentration of  $2 \times 10^{12} \text{ cm}^{-3}$ , is  $.4 \text{ cm}^{-1}$ .

Cyclotron resonance is observed in the same Ge sample, and the variation of linewidth with pulsed electric field studied. A  $\langle \tau \rangle$  of  $8 \times 10^{-11}$  seconds is found at an electric field of about 50 V/cm. It is found that the absorption linewidths are narrower than the emission linewidths by a factor of eight. The difference in linewidths is explained by considering the broadening mechanisms which are dominant at the two frequencies involved. In cyclotron resonance, at 110 GHz., the broadening can be explained by acoustic phonon scattering given an electron temperature of about  $50^\circ\text{K}$ . It would take a temperature of  $3000^\circ\text{K}$  to account for the emission linewidth by this means. The cyclotron emission linewidth can be explained by broadening due to non-parabolicity given an electron temperature of about  $90^\circ\text{K}$ , whereas it would take a temperature of over  $1000^\circ\text{K}$  to account for the resonance linewidth this way. We estimate that temperatures of 10 -  $100^\circ\text{K}$  are to be expected.

Some optical experiments are carried out on ion-implanted, laser annealed silicon and GaAs. In Si, it is found that the optical thick-

ness changes by approximately 1% after annealing. In one GaAs sample, the plasma frequency is found to be  $450 \text{ cm}^{-1}$ , giving a carrier concentration of  $1.9 \times 10^{18} \text{ cm}^{-3}$ . For a given implantation of  $10^{15} \text{ cm}^{-2}$  and assuming 10% electrical activity, this gives the implantation depth as  $.5 \text{ }\mu\text{m}$ .

An experiment is carried out to investigate one of the central-cell lines in GaAs. A sample is thermally annealed to introduce vacancies. The spectra indicate that a central-cell line due to vacancies may be present.

#### Acknowledgements

I would like to thank Professor R. A. Stradling for his patient and unflagging help in this project. I would also like to thank Mr. R. H. Mitchell and the members of the workshop and cryogenics department for their help and cooperation. I am grateful to the C. V. D. for the grant to do this project.

## Cyclotron Emission in Germanium

### Section I: Introduction

The electrical properties of semiconductors are dominated by the presence of shallow impurities. The energy gap between the valence and conduction bands of a semiconductor ranges from .2 eV for InSb to about 1.4 eV for InP and GaAs. Shallow impurities present in these semiconductors typically have binding energies of .01 to .1 eV. These impurities, therefore, are easily excited into the nearest band, and are the main source of charge carriers. Much of semiconductor technology today is based on methods of controlling the type, amount and location of impurities introduced into crystals.

One of the most important techniques for studying shallow impurity states is far-infrared spectroscopy. Far-infrared (FIR) radiation has the energy required to induce transitions between ground and excited impurity states (about 1 to 25 meV). There is therefore a great deal of interest in sources of FIR radiation. Molecular gas lasers have been available for many years, giving high intensity FIR radiation at a fixed wavelength, and some tunable FIR laser sources have been developed in the last ten years. One method mixes two laser beams in a non-linear crystal, giving a difference signal in the FIR (1). Other methods involve using dye lasers (2), or CO<sub>2</sub> lasers tuned with an intracavity grating (3). High intensity radiation is not needed for spectroscopic studies, however, the important considerations being spectral resolution and tunability. Fourier transform spectroscopy gives high resolution, tunability over a wide range and moderate power output. The drawback of this system is its expense. The aim of this project is to develop a tunable source of FIR radiation which can be used in a spec-

trometer system which is simple to set up and to use. The source of this radiation is the radiative recombination of impact ionized electrons between the Landau levels of a semiconductor in a magnetic field, known as cyclotron emission.

### Conduction band states in a magnetic field

In the presence of a magnetic field, the energy states of the conduction band are quantized in the direction perpendicular to the field. If the field is in the z-direction, then the energy states  $\mathcal{E}_n$  are given by:

$$\mathcal{E}_n = \frac{\hbar^2 k_z^2}{2m^*} + (n + \frac{1}{2}) \hbar \omega_c.$$

In the z-direction, the electron motion is undisturbed, while in the x-y plane the electrons circle in orbits around the field vector with cyclotron frequency  $\omega_c$ , where:

$$\omega_c = \frac{eB}{m^*}.$$

The result is a helical motion. In k-space, the energy states can be described as concentric cylinders with separation  $\hbar \omega_c$ . These states are called Landau levels. A semiconductor in a magnetic field will experience a resonant absorption of energy from radiation at a frequency equal to the cyclotron frequency. This absorption is known as cyclotron resonance.

To derive the expression for  $\mathcal{E}_n$ , we represent a magnetic field in the z-direction by its vector potential:

$$\underline{A} = (0, xB, 0).$$

The Hamiltonian is:

$$H = \frac{1}{2m^*} (\underline{p} + e\underline{A})^2$$

where  $\underline{p}$  is the momentum operator  $\underline{p} = -i\hbar\nabla$ . The addition of the field

brings in a term involving  $x$ , so we write the wave function as:

$$\Psi = e^{i(k_y y + k_z z)} \psi(x).$$

The Schrodinger equation is now:

$$H\Psi = \frac{1}{2}m^* (-i\hbar\nabla + e\mathbf{A})^2\Psi = \varepsilon\Psi$$

which becomes:

$$\frac{\hbar^2}{2m^*} [\psi''(x) - (k_y^2 + k_z^2)\psi(x)] + \frac{eBx}{2m^*} (eBx + 2\hbar k_y)\psi(x)$$

We can write:

$$\frac{\hbar^2 k_y^2}{2m^*} + \frac{e^2 B^2 x^2}{2m^*} + \frac{\hbar e B k_y x}{2m^*} = \frac{m^* \omega_c^2}{2} (x + x_0)^2$$

where:

$$\omega_c = \frac{eB}{m^*} \quad \text{and} \quad x_0 = \frac{\hbar k_y}{eB}.$$

The equation then becomes:

$$\frac{\hbar^2}{2m^*} \psi''(x) + \frac{m^* \omega_c^2}{2} (x + x_0)^2 \psi(x) = (\varepsilon - \frac{\hbar^2 k_z^2}{2m^*}) \psi(x)$$

which is the equation in  $x$  for a harmonic oscillator with energy levels:

$$\varepsilon_n = \frac{\hbar^2 k_z^2}{2m^*} + (n + \frac{1}{2}) \hbar \omega_c.$$

### Hydrogenic model of impurities

For the theoretical treatment of shallow impurity states, we consider the case of a donor impurity which has a single extra electron compared with the host atoms, for example a group V element in a group IV semiconductor. The theory is considerably simplified by assuming that the extra electron is in a very large orbit around the impurity ion. Over these large distances, the positive ion can be assumed to have a simple Coulomb potential:

$$V = \frac{e}{\epsilon r}.$$

The Schrodinger equation in this case is:

$$\left(\frac{\hbar^2}{2m^*}\nabla^2 - \frac{e^2}{\epsilon r}\right) F(r) = \mathcal{E}F(r),$$

though the kinetic energy term will be more complicated for materials with complex band structures. The situation is the same as a simple hydrogen atom with two differences: the potential energy is reduced by the value of the dielectric constant  $\epsilon$ , and the electron mass used is the effective mass  $m^*$  rather than the free electron mass  $m_0$ . The result is hydrogen-like energy states:

$$-\mathcal{E} = \frac{R^*}{n^2}$$

where the effective Rydberg  $R^*$  is the same as the hydrogenic Rydberg scaled down by  $\epsilon$  and  $m^*$ :

$$R^* = \frac{(m^*/m_0)}{\epsilon^2} R.$$

The impurity states are labelled by analogy to the hydrogenic atomic states, for example the ground state is 1s, the first excited state is 2p, etc. The electron has an effective ground state radius  $a^*$ , related to the Bohr radius  $a_0$  by:

$$a^* = a_0 \frac{\epsilon}{(m^*/m_0)}.$$

For GaAs the values are roughly  $m^*/m_0 = .07$  and  $\epsilon = 13$ . This gives  $\mathcal{E} = 5.6$  meV and  $a^* = 93 \text{ \AA}$ , so the impurity states given by this model have a low binding energy and large orbits, as assumed.

The wave functions  $F(r)$  are simply hydrogen-like wave functions:

$$F(r) = \frac{1}{\sqrt{\pi a^{*3}}} \exp(-r/a^*).$$

They are slowly-varying, and only have an effect over large distances, on the order of  $a^*$ . Over short distances, this model does not hold.

The potential of the impurity ion is not a simple Coulomb potential close to the ion, and the concept of a dielectric constant breaks down. Locally, the electron can be described as being in a Bloch state:

$$\phi(\mathbf{r}) = u(\mathbf{r})e^{i\mathbf{k}\cdot\mathbf{r}}$$

where  $u(\mathbf{r})$  is a rapidly varying periodic function which resembles an atomic wave function near the nucleus. The functions  $\phi(\mathbf{r})$  and  $F(\mathbf{r})$  will be degenerate in semiconductors with degenerate energy bands (germanium, for example, has four equivalent minima in the conduction band). Kohn (4) has shown that the total wave function will be the sum of linear combinations of  $\phi(\mathbf{r})$  and  $F(\mathbf{r})$ :

$$\Psi(\mathbf{r}) = \sum_{j=1}^N \alpha_j \phi_j(\mathbf{r}) F_j(\mathbf{r})$$

where  $N$  is the number of equivalent minima in the conduction band. This only holds if the Bloch functions used have small  $k$ -values ( $\lesssim \frac{1}{a^*}$ ). This condition is satisfied because the wave functions are extended in real space ( $a^*$  is large), and so are compressed in  $k$ -space. Over a short range, therefore, the electron behavior is described by  $\phi(\mathbf{r})$ , and over a long range it is modulated by  $F(\mathbf{r})$ .

Close to the impurity ion, the potential will vary slightly depending on which particular impurity is present. If the transition spectra are looked at in high enough resolution, different lines may be seen corresponding to different impurities. This is the "central cell" effect, and has been used to identify contaminants in some III-V compounds.(5) This will be discussed further in section VIII.

In a magnetic field, the splitting of the hydrogen-like impurity states is analogous to the Zeeman splitting of atomic states. In

the photoconductivity spectra of GaAs in figure 1.1, it can be seen that the  $1s \rightarrow 2p$  and  $1s \rightarrow 3p$  transitions separate for magnetic quantum number  $m = 0, +1, \text{ and } -1$ . The separation of the energy levels for  $m = +1$  and  $m = -1$  is equal to  $\hbar\omega_c$ , and the separation of the peaks due to the transitions to these levels has been used to measure  $m^*$ . (6)

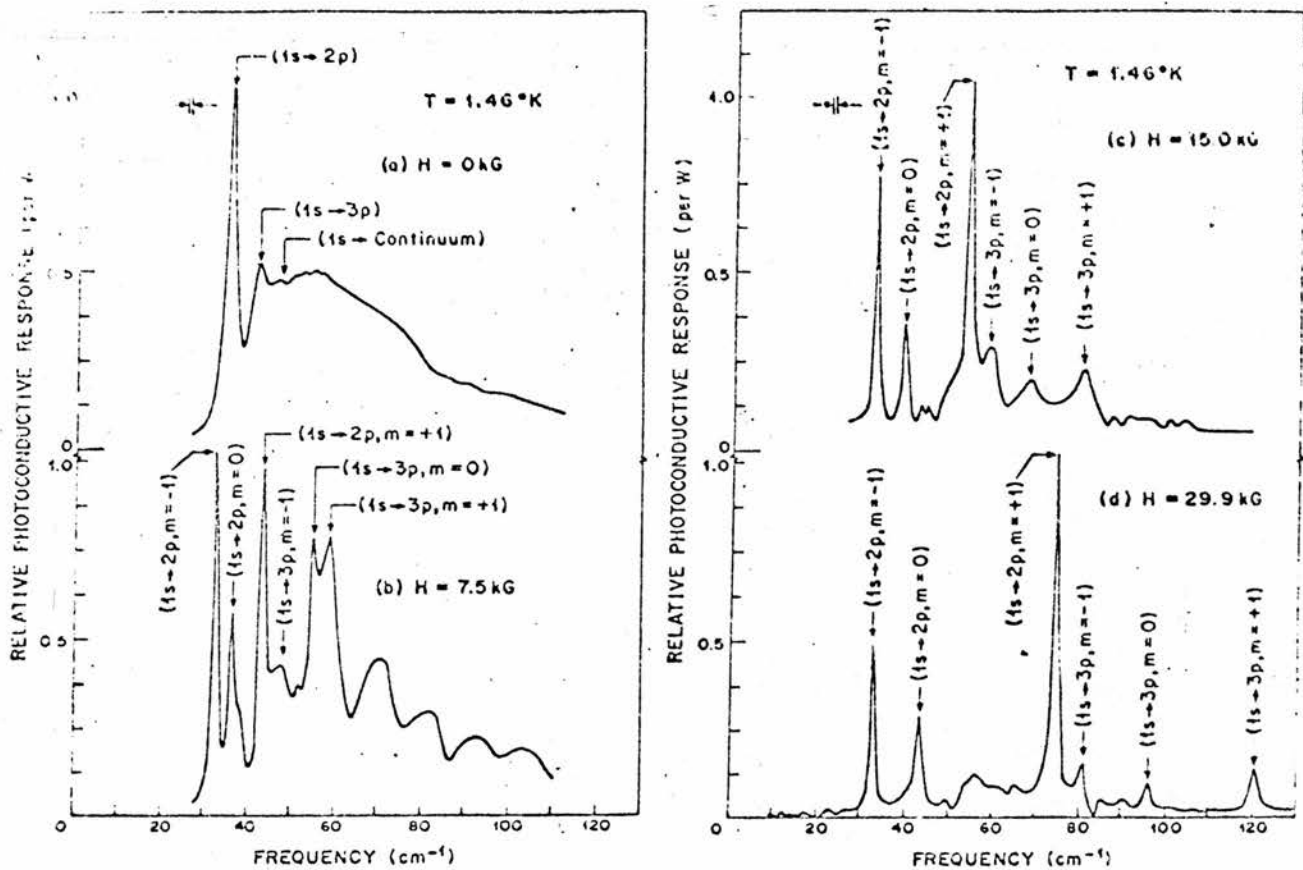


FIG. 1. Spectral response of the extrinsic photoconductivity of high-purity GaAs at 1.46°K at  $H = 0$  (Fig. 1a),  $H = 7.5$  kG (Fig. 1b),  $H = 15.0$  (Fig. 1c) and  $H = 29.9$  kG (Fig. 1d).

Figure 1.1

Photoconductivity spectra of GaAs with magnetic fields from 0 to 3 Tesla.

## Section II: Background Theory

### Cyclotron Emission

In this project, we use the emission from electronic transitions between the Landau levels of a semiconductor as a source of radiation. Normally, all conduction electrons present at 4.2°K are in the lowest Landau level and the impurity ground state. By applying an electric field of several volts per centimeter the electrons are excited into higher Landau levels and emission is observed between neighboring levels. The radiation is emitted with the cyclotron frequency:

$$\omega_c = \frac{eB}{m^*}.$$

With a small effective mass and a fairly large magnetic field, the cyclotron frequency is in the far-infrared region of the spectrum. For example, if  $m^* = .07 m_0$  (GaAs) and  $B = 5$  T, then  $\omega_c$  corresponds to a wavelength of 140 microns. Since the cyclotron frequency is proportional to the magnetic field, the radiation can be tuned continuously simply by sweeping the field. The range over which the emission can be tuned is from 50 to about 500 microns.

Using the emission between Landau levels as a tunable far-infrared source was first proposed by Lax in 1960 (7). Cyclotron emission was first observed by Gornik in 1972 (8) and Kubayashi, et. al., in 1973 (9). Gornik observed a power output of about  $10^{-8}$  Watts in InSb, and a linewidth of a few wavenumbers. Since then, cyclotron emission has been extensively studied in both InSb and GaAs by Gornik and other groups (10 - 12, for example) and has also been investigated in HgCdTe (13) and InP (14). We have looked at cyclotron emission in Ge here in St. Andrews. Optically excited cyclotron emission has been studied (15), as has emission from Si inversion layers in Si-MOSFET devices (16). Recent results have given power outputs of up to 1  $\mu$ W in GaAs and InSb and a linewidth

of less than  $1 \text{ cm}^{-1}$  in GaAs. Our results here indicate a linewidth of  $.4 \text{ cm}^{-1}$  for Ge. By comparison, a typical Fourier transform spectrometer has a power output of  $10^{-8} \text{ W}$  and a resolution as good as  $.04 \text{ cm}^{-1}$ .

### Materials for Cyclotron Emission

The material which would be the best source of radiation is one which optimizes three properties of the emission: wide range of tuning, narrow linewidth and high intensity. The first is limited by two factors. In the long wavelength, low magnetic field limit, the separation between the Landau levels is comparable to the broadening of the levels and the sharply-peaked emission is lost. This happens at about  $500 \mu\text{m}$ , which corresponds to about  $.3 \text{ T}$  in InSb,  $1.5 \text{ T}$  in GaAs and  $1.7 \text{ T}$  in Ge. In the short wavelength, high field limit (about  $50 \mu\text{m}$ ), the emission is strongly reduced above the optical phonon energy. This occurs at about  $3 \text{ T}$  in InSb,  $22 \text{ T}$  in GaAs and  $26 \text{ T}$  in Ge. Figure 2.1 shows the intensity of the emission signal in InSb between 0 and  $3 \text{ T}$ .<sup>(10)</sup> Also, the lower the effective mass, the lower the magnetic field needed to produce a given frequency. For example, GaAs, with an effective mass of about  $.07 m_0$ , can emit radiation with a wavelength of  $100 \mu\text{m}$  with a field of  $7 \text{ T}$ . HgCdTe, with an effective mass of  $.006 m_0$ , can emit radiation of  $100 \mu\text{m}$  at  $.5 \text{ T}$ . A graph of frequency (in  $\text{cm}^{-1}$ ) against magnetic field is shown in figure 2.2 for several semiconductors. (11)

The linewidth of the emission depends on two main factors. One is the dominant scattering mechanism, which in semiconductors at low temperatures is ionized impurity scattering. In this case, the linewidth is proportional to the square root of the ionized impurity concentration. This relation has been tested in several semiconductors by Cornik, et. al., (14) and is shown in figure 2.3 for InP and GaAs. The second factor is

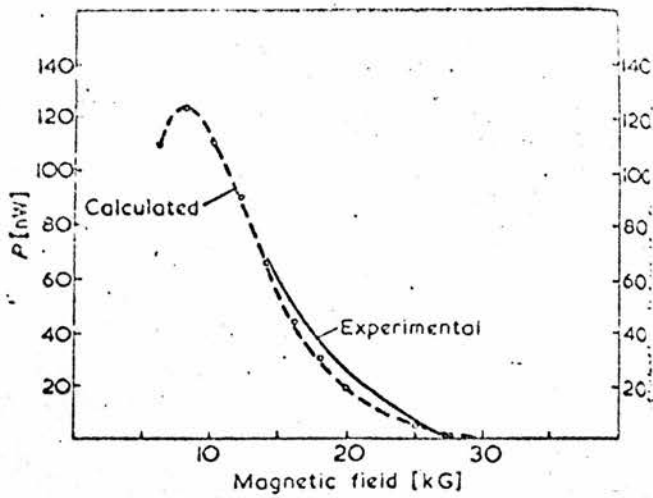


Figure 2.1

Intensity of emission signal in InSb between 0 and 3 T.

Fig.2 Comparison of the calculated intensity (Table 1) with the photo-conductive signal of a Ge (Ga) detector (divided by its spectral response <sup>15</sup>) for n-InSb

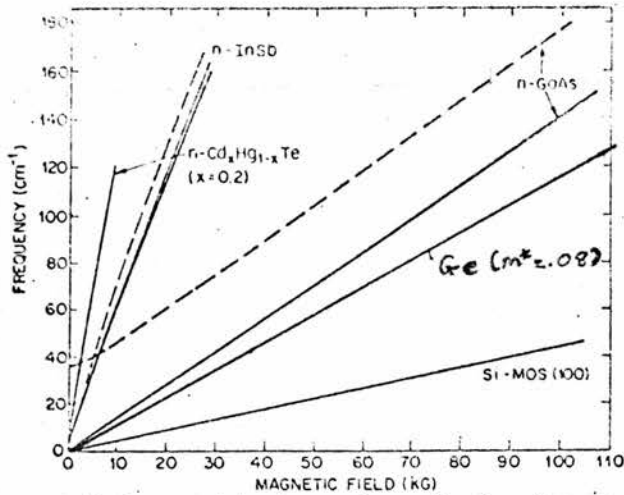


Figure 2.2

Frequency vs. magnetic field for several semiconductors.

Fig. 1. Cyclotron emission frequencies as a function of magnetic field for different semiconductors. The dashed line indicates the frequency of associated impurity transitions.

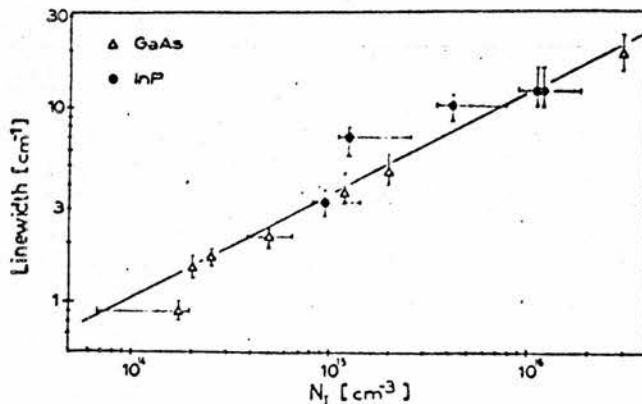


Figure 2.3

Emission linewidth vs. ionized impurity concentration for GaAs and InP.

Fig.4: Emission linewidth as a function of total ionized impurity concentration as derived from the mobility analysis for GaAs and InP. The full curve show the  $\Delta\omega \propto N_I$  dependence.

non-parabolicity of the conduction band, which causes the separation of the Landau levels to decrease with increasing energy. This means that if several Landau levels are occupied, then the emission line will be broadened on the low energy side. Non-parabolicity can also have an effect when only one excited Landau level is filled, because the energy separation between the levels can vary in k-space. Non-parabolicity can be a large effect in the smaller gap materials (InSb and HgCdTe) and is a small effect in the larger gap materials (GaAs and InP). (10)

The emission line can also be broadened by self-absorption if the sample is too thick. The relation for the self-absorption to be negligible is:

$$\alpha d \ll 1$$

where  $\alpha$  is the absorption coefficient and  $d$  is the sample thickness.

Figure 2.4 shows the effect of self-absorption for  $\alpha d$  between .5 and 2.2. (17)

In a thin sample, the main contribution to the emission comes from the  $1^+$  to  $0^+$  Landau level transition. When the sample is thick, this line is the most strongly self-absorbed. Thus the weaker  $1^-$  to  $0^-$  Landau level transition is enhanced, as is the impurity transition associated with the first and zero<sup>th</sup> Landau levels.

In deriving the expression for the power output, Gornik has shown the power to be nearly independent of the type of semiconductor used. (10) The total emitted power is given by:

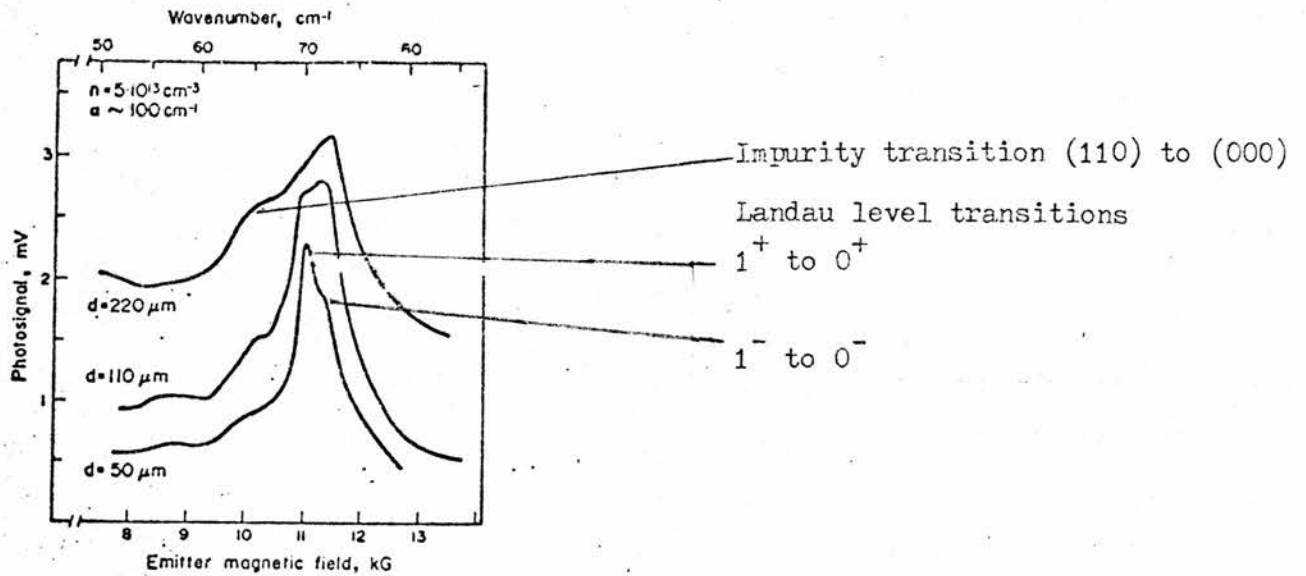
$$P = FR\hbar\omega_c V$$

where  $F$  = probability of escape of light for a non-directional emission:

$$F = \left(1 + \frac{\alpha V}{AT}\right)^{-1}$$

$T$  = transmission coefficient,  $\alpha$  = absorption coefficient,  $V$  = sample volume,  $A$  = sample area,  $R$  = emission rate per unit volume. Assuming a Maxwell-Boltzmann distribution in the conduction band,  $R$  is given by:

Tunable far-infrared InSb-source



2. Photoconductive signal of  $n$ -GaAs at 30 kG vs emitter magnetic field for sample thicknesses of 220, 110 and 50  $\mu\text{m}$ .

Figure 2.4 Emission signal from samples of different thicknesses.

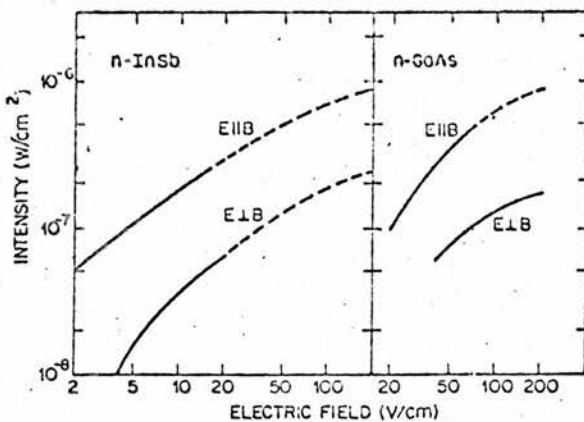


Fig. 4. Emission intensity versus applied electric field  $E$  for longitudinal ( $E \parallel B$ ) and transverse ( $E \perp B$ ) configuration [14]. The emission frequency is  $100 \text{ cm}^{-1}$ . Range of CW operation (full curves) pulsed operation (dashed curves).

Figure 2.5

Emission intensity of GaAs and InSb in longitudinal and transverse configurations.

$$R = n(1 - e^{-\alpha}) \sum_N W e^{-\alpha N}$$

where  $n$  = concentration of carriers,  $N$  = number of Landau levels and  $\alpha = \hbar\omega_c/kT_e$  where  $T_e$  is the electron temperature.  $W$  is the spontaneous transition probability, given by:

$$W = \frac{\eta^2 e^2 \mu_0 \omega_c^3}{3c\hbar\pi} l^2 N \text{ sec}^{-1}$$

where  $\eta$  is the refractive index and  $l$  is the cyclotron orbit radius.

Now, the sum in  $R$  converges to:

$$\frac{e^\alpha}{(e^\alpha - 1)^2}$$

If  $\alpha$  is greater than 1 ( $\alpha$  will usually be about 1 here), then

$$(1 - e^{-\alpha}) \frac{e^\alpha}{(e^\alpha - 1)^2} \sim \frac{1}{\alpha}$$

to first order. If  $\alpha$  is large, then

$$F \sim \frac{AT}{V\alpha} \text{ and also } \alpha \propto \frac{\omega_c l^2 n}{\eta}$$

Combining these expression gives:

$$P \propto AT\eta^2 \omega_c^2 T_e$$

For transmission from a semiconductor to a vacuum,

$$T = \frac{1}{\eta^2} \left(1 - \frac{(\eta - 1)^2}{(\eta + 1)^2}\right)$$

Therefore,

$$P \propto AT_e \omega_c^2 \left(1 - \frac{(\eta - 1)^2}{(\eta + 1)^2}\right)$$

The power emitted will thus be the same for semiconductors with the same refractive index, electron temperature, cyclotron frequency and area.

Gornik has also shown that the output power is several times higher in a longitudinal rather than transverse orientation. (12)

(figure 2.5). This is because of the greater resistance of the sample in the transverse configuration in a magnetic field.

Another consideration is that different electric fields are needed to break down the different materials when the carriers are frozen out into the impurity states. This field depends on the donor ionization energy of the material, which is related to the effective mass and the dielectric constant by:

$$\epsilon_0 \propto \frac{m^*}{\epsilon^2}$$

These values are about .6 meV for InSb, 5 meV for GaAs, 7 meV for InP and 9 meV for Ge.

From these points it can be seen that while InSb has the advantage of a small effective mass so that small electric and magnetic fields can be used, it has the disadvantage of non-parabolicity. GaAs and InP have negligible non-parabolicity, but require higher electric fields for breakdown and higher magnetic fields for emission at a given frequency. Ge needs higher electric and magnetic fields, and also has the complication of a multi-valley conduction band. This means that unless the sample is oriented with the magnetic field in the  $\langle 100 \rangle$  direction, the emission will be at several different frequencies and the electric field heating will be different for the different valleys. An advantage of Ge is that it is not a polar material, so the optical phonon relaxation will not be as strong an interaction as it is in other materials. However, the most decisive factor in choosing a material for cyclotron emission is the purity of the sample, which makes Ge the most suitable material available today.

## Hot Electron Theory

When an electric field is applied to the sample, the electrons are excited into higher Landau levels by impact ionization. If the electron concentration is sufficient, electron-acoustic phonon interactions are weak and the energy from the electric field is stored in the electron system. In this case, the electrons are effectively decoupled from the lattice and can be described by a Maxwell-Boltzmann distribution with an effective electron temperature  $T_e$ . The distribution  $f(\mathcal{E})$  is described by:

$$f(\mathcal{E}) \propto \exp(-\mathcal{E}/kT_e).$$

The electron temperature is considerably higher than the lattice temperature and the electrons are called "hot".

Numerical calculations of hot electron distribution functions for InSb have been done by Yamada and Kurosawa.<sup>(18)</sup> They assumed that the energy transferred in the frequent scattering events is small and approximate the process by a diffusion equation. At low electric fields, the distribution function corresponds to a Maxwell-Boltzmann distribution with temperature  $T_e$ . At higher electric fields, as the electron energy nears the optical phonon energy, deviations from the Maxwell-Boltzmann distribution are observed. The distribution is cut off at the optical phonon energy.

Gornik has measured electron temperatures to be considerably lower than those predicted by the Yamada and Kurosawa theory (19). The explanation is that electron-electron scattering knocks electrons above the optical phonon energy and so, by enhancing the optical phonon relaxation, reduces the electron heating. Therefore, as the electric field is increased, the electron heating decreases (figure 2.6). Figure 2.7 shows

Fig. 6: Electron temperature versus total electric field at 0.55T. n-InSb samples: • 2Cl3; Δ 8N13. The theoretical results according to Partl et al.<sup>18</sup> are given by the full curve for 2Cl3 and the dashed curve for 8N13. Neglecting e-e scattering gives curve labeled YK.

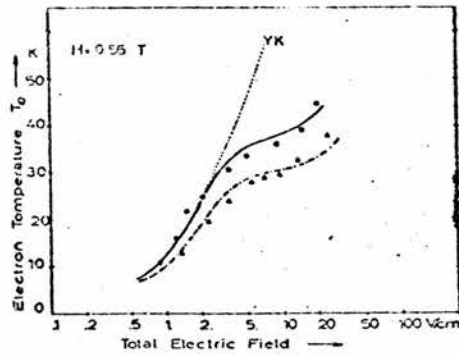


Figure 2.6

Theoretical and experimental electron temperatures vs. electric field.

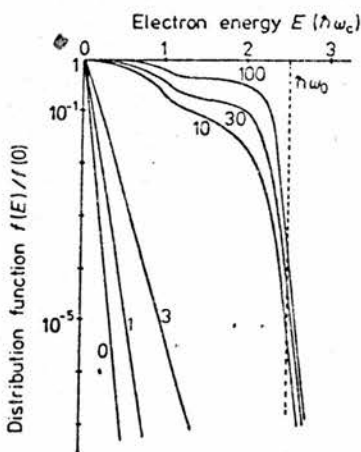


Figure 3. Distribution function  $f(E)$  for different  $F_{tot}$  (in  $V/cm^{-1}$ )  $H = 12$  kG,  $n_{imp} = 7 \times 10^{14} cm^{-3}$ ,  $T_0 = 4.2$  K,  $\Gamma = 10$  K, but for  $n_e = 0$ .

Figure 2.7a

Distribution functions calculated without electron-electron scattering.

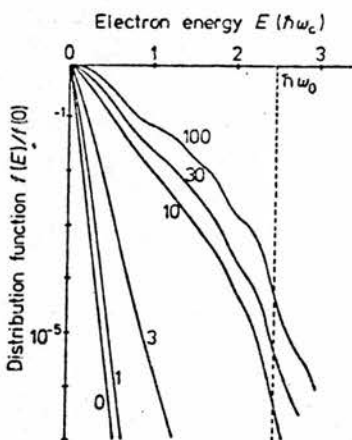


Figure 2. Distribution functions  $f(E)$  for different  $F_{tot}$  (in  $V/cm^{-1}$ ).  $H = 12$  kG,  $n_{imp} = 7 \times 10^{14} cm^{-3}$ ,  $n_e = 1.5 \times 10^{14} cm^{-3}$ ,  $T_0 = 4.2$  K,  $\Gamma = 10$  K.

Figure 2.7b

Distribution functions calculated including electron-electron scattering.

calculated distribution functions for various electric fields.<sup>(19)</sup> It can be seen that when the effect of electron-electron scattering is included in the theory, the deviation of the distribution function from a Maxwell-Boltzmann distribution is not as great. In this case, the distribution is sharply decreased, but not entirely cut off, at the optical phonon energy.

The quantity  $\Gamma$  in figure 2.7 accounts for the broadening of the Landau levels due to fluctuations in the impurity potential.  $\Gamma$  is proportional to the square root of the ionized impurity concentration.

#### Cyclotron Resonance Linewidths

The linewidth in cyclotron resonance depends on the scattering time  $\tau$ . In general,  $\tau$  is a function of the electron energy, but to derive the expression for the linewidth it is easiest to consider first the case of a constant  $\tau$ . We also use the approximation of spherical energy bands. The equation of motion for a charged particle with a magnetic field in the z-direction and a circularly polarized electric field in the x-y plane is:

$$\frac{d}{dt}(\underline{v}) + \left(\frac{1}{\tau} - i\omega_c\right)(\underline{v}) = \frac{e}{m^*} \underline{E}_0 e^{i\omega t}$$

where  $\underline{v} = v_x + iv_y$ . This has the solution:

$$\underline{v} = \frac{e}{m^*} \frac{E_0 e^{i\omega t}}{1 + i(\omega - \omega_c)\tau}$$

This gives a resonance at  $\omega = \omega_c$  when the carrier velocity is in phase with the field. This is only for the case of right-hand circular polarization; the other sense of polarization gives the term  $\omega + \omega_c$  which does not give a resonance. The complex conductivity is found from the relation:

$$\sigma = ne\mu = \frac{nev}{E}$$

which gives:

$$\sigma = \frac{ne^2}{m^*} \frac{\tau}{1 + i(\omega - \omega_c)\tau}$$

In the general case,  $\sigma$  will be a tensor quantity. The power the carrier absorbs from the electric field is:

$$\begin{aligned} P &= \text{Re}(\sigma E^2) \\ &= \left( \frac{Ne^2 E_0 \tau}{m^*} \right) \frac{1}{1 + (\omega - \omega_c)^2 \tau^2} \\ &= P_0 \frac{1}{1 + (\omega - \omega_c)^2 \tau^2} \end{aligned}$$

The quantity  $P_0$  is the power at resonance when  $\omega = \omega_c$ . At half-power,  $P = \frac{1}{2}P_0$ , and:

$$(\omega - \omega_c)^2 \tau^2 = \Delta\omega_{\frac{1}{2}}^2 \tau^2 = 1.$$

Therefore, the half-width at half-height,  $\Delta\omega_{\frac{1}{2}}$ , is equal to  $1/\tau$ . In terms of magnetic field,

$$\omega_c = \frac{eB}{m^*}$$

and so,

$$\frac{B}{\Delta B_{\frac{1}{2}}} = \frac{\omega}{\Delta\omega_{\frac{1}{2}}} = \omega\tau.$$

$P/P_0$  is plotted in figure 2.8 for different values of  $\omega\tau$  (20).

If  $\tau$  is a function of the electron energy, however, an average  $\langle\tau\rangle$  must be used. The form of this average depends on the experiment involved. In the case of dc conductivity, the average is taken with the weighting function:

$$\mathcal{E}f(\mathcal{E})N(\mathcal{E})d\mathcal{E}$$

where  $N(\mathcal{E})d\mathcal{E}$  is the number of states with energy  $\mathcal{E}$  in the interval  $\mathcal{E}$  to  $\mathcal{E} + d\mathcal{E}$  and  $f(\mathcal{E})$  is the electron distribution function. If the disturbance to the equilibrium distribution function  $f_0$  is small, this weighting

function can be approximated as:

$$\epsilon^{3/2} f_0 d\epsilon$$

where

$$f_0 \propto \exp(-\epsilon/kT).$$

The energy dependence of  $\tau$  varies with the different scattering mechanisms. For many cases we can say  $\tau \propto \epsilon^p$ , where  $p = -\frac{1}{2}$  for acoustic phonon scattering and  $p = 3/2$  for ionized impurity scattering.

The average  $\langle \tau \rangle$  has the form:

$$\langle \tau \rangle_{dc} = \frac{\int_0^{\infty} \epsilon^{3/2 + p} \exp(-\epsilon/kT) d\epsilon}{\int_0^{\infty} \epsilon^{3/2} \exp(-\epsilon/kT) d\epsilon}. \quad (21)$$

In the case of cyclotron resonance, the average  $\langle \tau \rangle_{cr}$  has a different form. Hindley (22) has done calculations of the conductivity tensor using  $\tau = \tau_0 (\epsilon/kT)^p$ . The conductivity is of the form:

$$\text{Re}\left(\frac{\sigma}{\sigma_0}\right) \propto \int_0^{\infty} \frac{\epsilon^{3/2 + p} \exp(-\epsilon/kT)}{1 + (\omega - \omega_c)^2 \tau_0^2 \epsilon^{2p}} d\epsilon.$$

Whereas a constant  $\tau$  leads to a Lorentzian lineshape, the effect of the energy-dependent  $\tau$  is to distort the lineshape. In this case, the simple relation between the linewidth and  $\omega\tau$  no longer holds. It has been found that the linewidth can be described by:

$$\omega \langle \tau \rangle_{cr} = h \frac{B}{\Delta B_{\frac{1}{2}}}$$

where  $h = 1$  if  $p = 0$  and  $h = .65$  if  $p = 1.5$ .

There is still a great deal of uncertainty in the subject of cyclotron resonance lineshapes for the case of ionized impurity scattering, though for the case of acoustic phonon scattering there is good agreement between theory and experiment. <sup>(23,24)</sup> In the experimental results given later, we describe the linewidth in terms of  $\omega\tau$  for

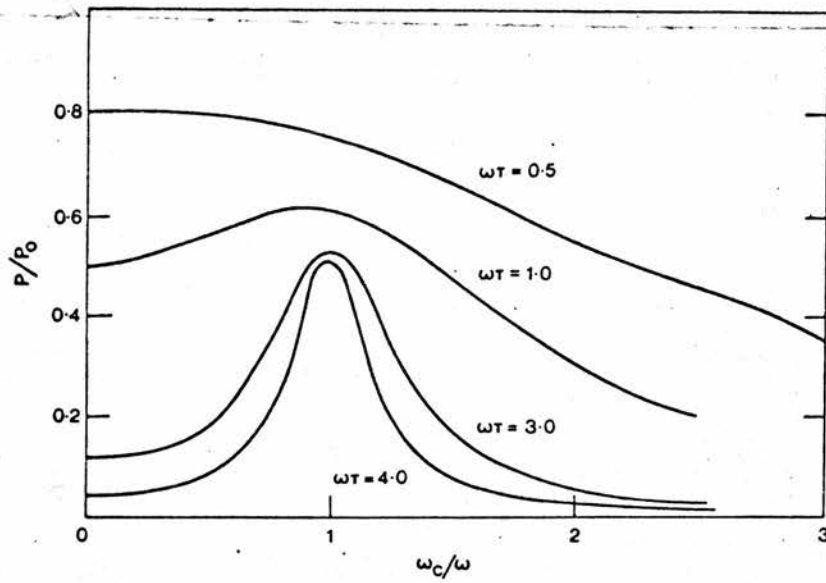


Fig. 1. The microwave power absorption  $P$  as a function of magnetic field, or of  $\omega_c/\omega$ , where  $\omega_c$  is the cyclotron frequency.  $P_0$  is the absorption when  $H = 0$  and  $\omega = 0$  (after Lax et al. 1954).

Figure 2.8

Power absorption in cyclotron resonance vs. magnetic field for several values of  $\omega\tau$ .

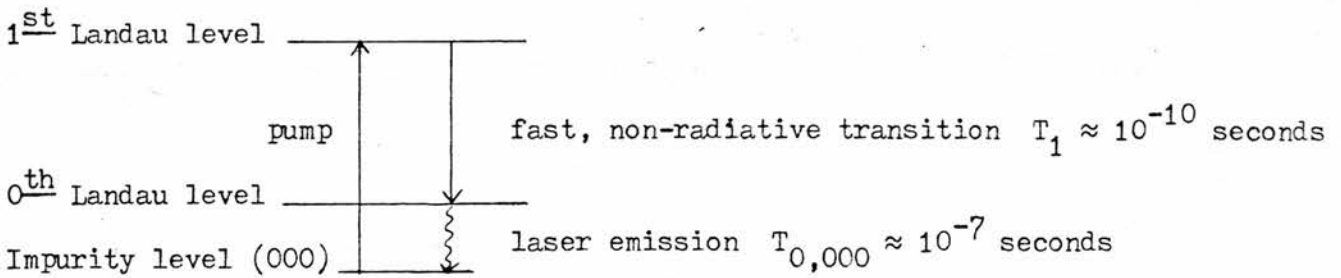


Figure 2.9

Level structure for a cyclotron emission laser.

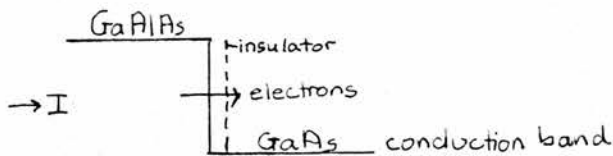


Figure 2.10

Heterojunction used to obtain a population inversion in GaAs.

convenience, but this cannot be taken as a quantitative measure of the relaxation time.

### Lifetimes

The lifetime of the first Landau level is a subject of interest because of the possibility of developing a cyclotron emission laser. Being able to establish a population inversion between the ground and first excited Landau level depends on the lifetime of the first level,  $T_1$ . This in turn depends on the dominant energy relaxation mechanism. If the electron concentration in the first Landau level,  $n_1$ , is very low, the electrons relax by electron-acoustic phonon interactions. In InSb, for example, this is for  $n_1$  on the order of  $10^{10} \text{ cm}^{-3}$ . Acoustic phonon relaxation is a comparatively slow process with  $T_1 \approx 10^{-7}$  seconds and is only observed in pure samples at low electric fields. For higher  $n_1$ , electron-electron scattering is the dominant process, enhancing the optical phonon relaxation by exciting electrons above the optical phonon energy. This is a faster process, with  $T_1 \approx 10^{-10}$  seconds for  $n_1 \approx 10^{13} \text{ cm}^{-3}$  in InSb. In general, it is found that  $T_1$  is inversely proportional to  $n_1$ .

While this very short  $T_1$  makes a population inversion between the ground and first excited Landau levels untenable, a scheme for a pulsed, low frequency laser has been suggested by Muller and Gornik (25). Electrons are pumped from the impurity ground state (000) to the first Landau level, where they collect due to the longer lifetime of this level,  $T_{0,000}$ . Longer wavelength emission is then observed from transitions to the impurity level (figure 2.9).  $T_{0,000}$  has been found to be magnetic field-dependent, ranging from 50 - 200

nanoseconds. Pulses on the order of  $T_1$ , less than about 10 nanoseconds, would be necessary.

Another scheme for a cyclotron emission laser uses a GaAlAs-GaAs heterojunction (figure 2.10). Electrons can be injected from the conduction band of GaAlAs into the conduction band of GaAs at whatever energy is required, in this way setting the energy to the desired  $n\hbar\omega_c$ . The ground state of the GaAs conduction band can be emptied, and so a population inversion will occur.

### Structure of Materials

#### Germanium

Germanium is a group IV semiconductor with the structure of diamond. The crystal has tetrahedral symmetry, and the lattice is face-centered cubic. The four valence electrons of each atom form covalent bonds with the atom's four nearest neighbors. The reciprocal lattice of Ge is body-centered cubic, and the first Brillouin zone is a truncated octahedron, as shown in figure 2.11.<sup>(26)</sup> The band structure of Ge is shown in figure 2.12.<sup>(27)</sup> The material has an indirect gap, with the conduction band minima at the Brillouin zone edges in the  $\langle 111 \rangle$  directions. These are the L points in figure 2.11; there are eight faces but only four minima because the points at opposite Brillouin zone edges are equivalent. The valence band is degenerate at  $k = 0$  and is described by two effective masses corresponding to the light and heavy holes:

$$m_{HL} = .043 m_0$$

$$m_{HH} = .34 m_0$$

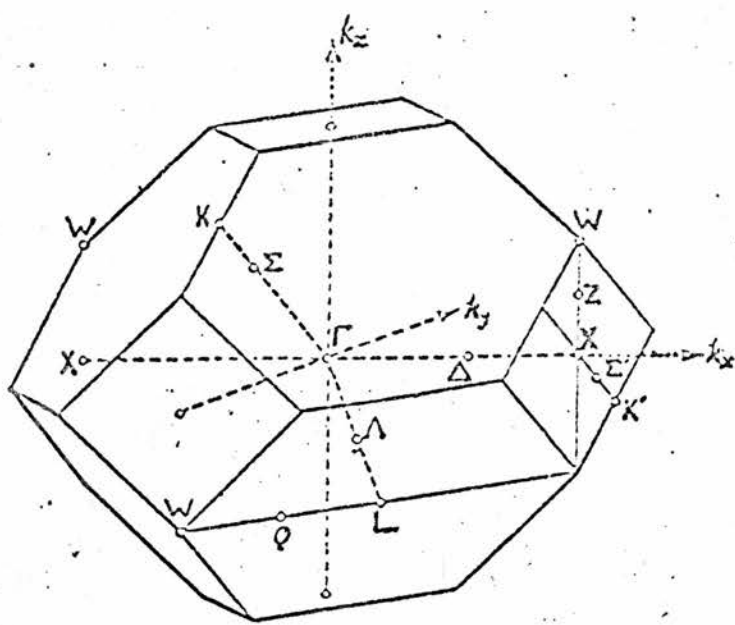


Figure 2.11  
Brillouin zone for face-centered  
cubic structure.

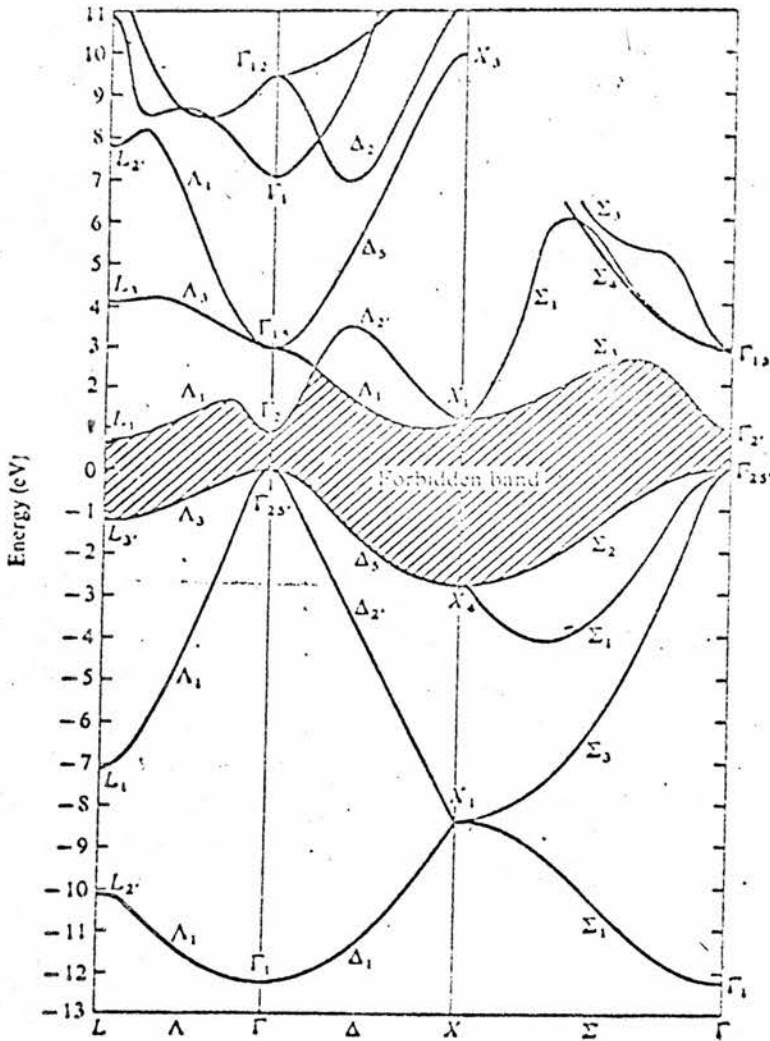


Figure 2.12  
Energy bands of germanium.

Fig. 2.10 The energy bands of germanium, with spin-orbit coupling neglected, as calculated by F. Herman, R. L. Kortum, C. D. Kuglin, and J. L. Shay [in D. G. Thomas (ed.), "II-VI Semiconducting Compounds, 1967 International Conference," Benjamin, New York, 1967].

A third band is split off by the spin-orbit interaction and is characterized by:

$$m_{HS} = .077 m_0.$$

The constant energy surfaces of the conduction band are ellipsoids of rotation around the  $\langle 111 \rangle$  axes. The longitudinal and transverse effective masses are:

$$m_L = 1.59 m_0$$

$$m_T = .082 m_0.$$

In a magnetic field, the cyclotron effective mass varies with the orientation of the field. For a magnetic field at an angle  $\theta$  with the axis of an ellipsoid, the cyclotron effective mass is given by:

$$\frac{1}{m_c} = \frac{\cos^2 \theta}{m_T} + \frac{\sin^2 \theta}{m_T m_L}$$

For other purposes, the conductivity effective mass:

$$m_{\text{cond}} = \frac{3m_L m_T}{2m_L + m_T} = .12 m_0$$

or the density of states mass:

$$m_D = (m_L m_T^2)^{\frac{1}{2}} = .22 m_0$$

are used. (21, 26)

### III - V Compounds

Semiconductors such as GaAs, InP and InSb are compounds of group III and group V elements. They form a zincblende structure, which is of the same form as diamond but with the two types of atoms alternating. The bonding is predominately covalent, but with an ionic component. These materials have a direct gap at  $k = 0$  and the constant energy surfaces in the conduction band are approximately spherical for small

k values. The valence band is degenerate at  $k = 0$  and similar in form to germanium. The size of the energy gap and the effective masses of several III-V compounds are in figure 2.13. (26, 28)

<u>Material</u>	<u><math>E_G(0^\circ\text{K})</math></u>	<u><math>E_G(300^\circ\text{K})</math></u>	<u><math>m_E(4^\circ\text{K})</math></u>	<u><math>m_{HH}</math></u>	<u><math>m_{HL}</math></u>	<u><math>\mu_E(300^\circ\text{K})</math></u>	<u><math>\mu_H</math> (cm<sup>2</sup>/V-s)</u>
InSb	.24 eV	.18 eV	.014 $m_0$	.39	.016	77,000	750
InP	1.42	1.35	.080	.59	.12	4600	150
GaAs	1.52	1.43	.067	.54	.09	8800	400
Ge	.744	.67	—	.34	.043	4500	3500

Figure 2.13.

Energy gaps, effective masses and mobilities of several III-V compounds and germanium.

### Section III: Experimental Methods

Two methods have been used to observe cyclotron emission, both using the photoconductive response of another sample as detector. When light incident on a sample induces a transition to the conduction band, an increase in conductivity takes place. If a constant current is put through the sample, the change in conductivity can be observed as a change in voltage. The relation is:

$$\Delta V = - V \left| \frac{\Delta \sigma}{\sigma_0} \right|$$

where  $V$  is the applied voltage and  $\sigma_0$  the conductivity in the absence of applied radiation. One method of observing cyclotron emission is to use a broadband photoconductive detector, as shown in figure 3.1. (11)

The spectra show the sharp start of the Ge:Ga detector response, the absorption of a AgI filter and the loss of the emission signal at the optical phonon energy. The second method is to use a narrowband photoconductive detector, which is the method we have used here with a GaAs sample as the detector. The emission is seen when it causes a transition between the 1s and 2p impurity states in the detector. It is believed that a sharp photoconductive response is seen when photoexcitation to the excited impurity states is followed by thermal excitation to the conduction band. Stillman, et. al., have shown that the probability of this process is high at 4.2°K. (29)

Examples of spectra taken with a narrowband detector are in figure 3.2. The main peak is the 1s - 2p transition line and the broad shoulder is due to impurity photoionization. The detector is in zero magnetic field in these spectra. In the experimental set-up we have been using, the emitter is placed in the center of a superconducting magnet and the detector can be raised or lowered to be in any fraction

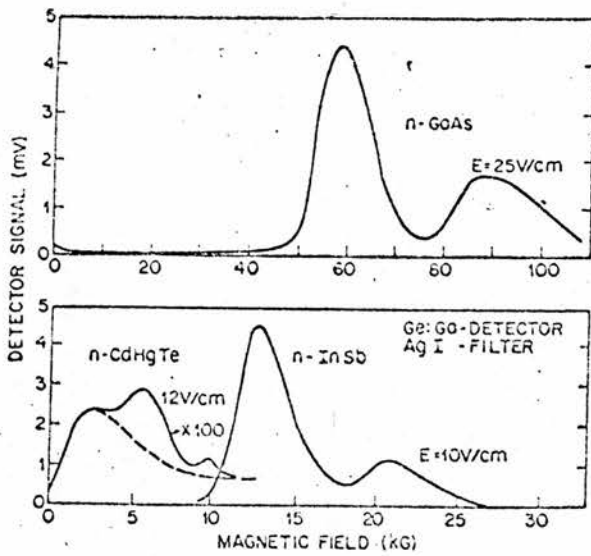


Fig. 3. Photoconductive signals of a Ge:Ga detector with a AgI filter inserted between detector and emitter. The emission frequency is tuned with the magnetic field:

Figure 3.1

Cyclotron emission observed with a Ge:Ga broadband photoconductive detector.

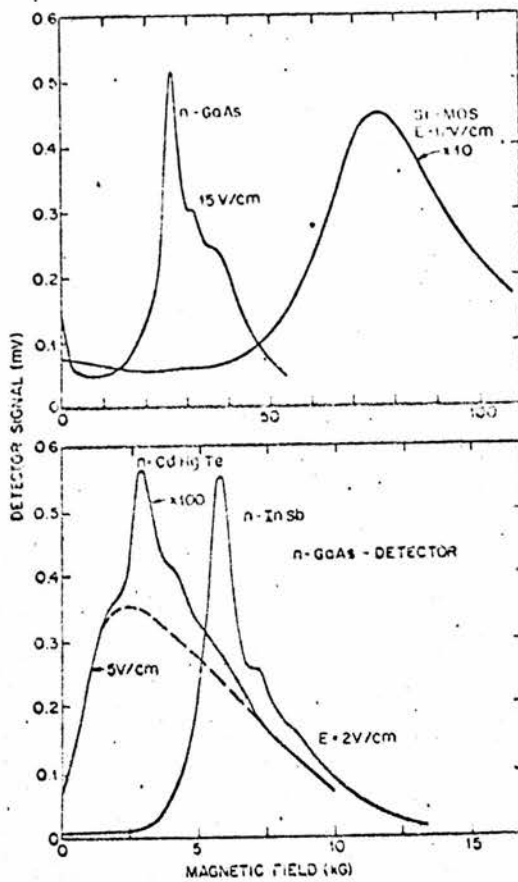


Fig. 2. Photoconductive signals of an n-GaAs detector as a function of the magnetic field of cyclotron emission samples for a given electric field.

Figure 3.2

Cyclotron emission observed with an n-GaAs narrowband photoconductive detector.

of the emitter field. Ideally the emitter and detector would be in separate magnet coils so that they could be tuned independently. A signal is observed when the cyclotron frequency of the emitter corresponds to the frequency of the  $1s - 2p^-$  impurity transition in the detector,  $\bar{\nu}(2p^-)$ , which in GaAs varies only slightly with magnetic field. The relation:

$$\frac{\omega_c}{2\pi c} = \frac{eB}{m^* 2\pi c} = \bar{\nu}(2p^-)$$

can be used to find the effective mass of the emitting sample in terms of the magnetic field. For  $\bar{\nu}(2p^-) = 32.5 \text{ cm}^{-1}$ , the corresponding emitter fields are .5 T for InSb, 2.3 T for GaAs and 2.8 T for Ge oriented so that  $m^* = .08 m_0$ .

The problem with analyzing this kind of spectra is that the signal is the convolution of the emission linewidth and the detector response. This means that absolute measures of the linewidth cannot be obtained without deconvoluting the results. It has been suggested by Tysson, et. al., (30) that Fourier spectroscopy may be used for more accurate study of the emitted radiation. For example, he saw previously unresolved emission lines splitting into doublets, one line corresponding to a free carrier transition between Landau levels and one weak line to an impurity transition. However, problems have been encountered involving the modulation of optical constants with electric field; background radiation is modulated by the varying reflection and transmission coefficients and this can look just like the emission signal. These problems and ways to overcome them are discussed by Muller, et. al. (31).

The experimental set-up we have used for observing cyclotron emission is shown in figure 3.3. The emitting sample is in a superconducting magnet, either a 6 T or a 12.7 T magnet being used, and the

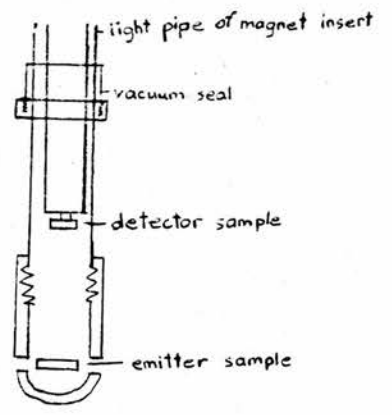
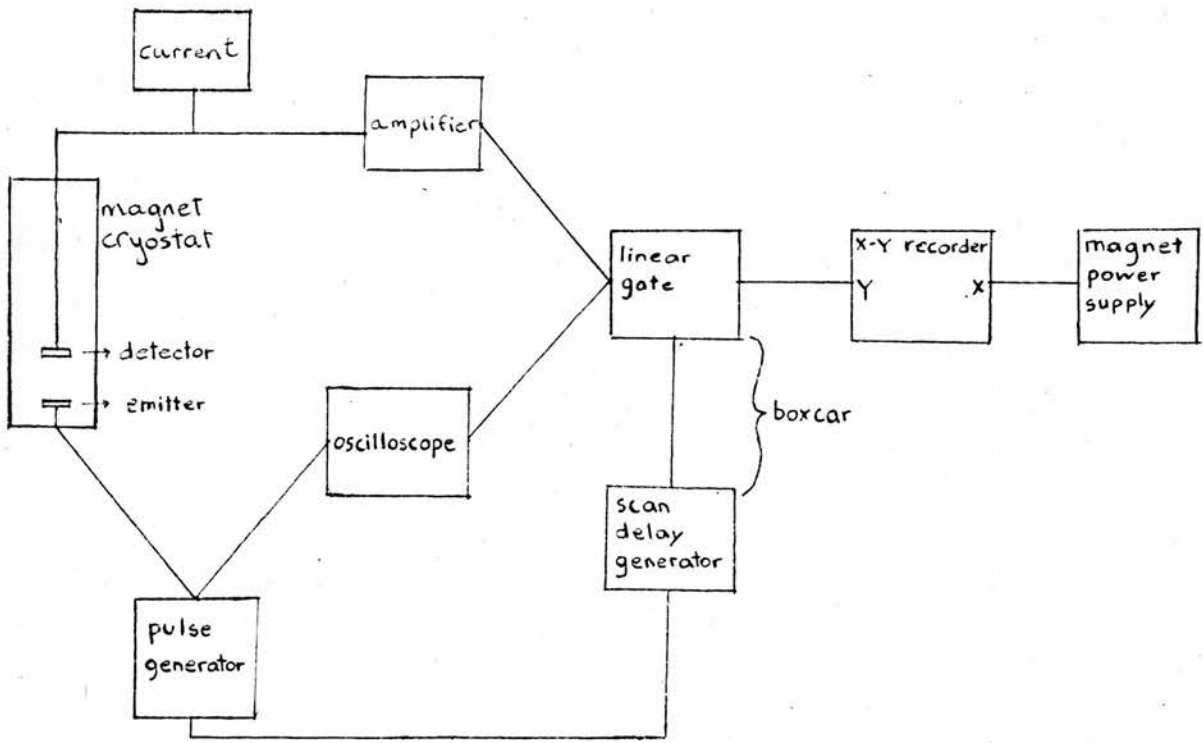


Figure 3.3  
Cyclotron emission experimental set-up.

detecting sample is held above it in the light pipe of the magnet insert. Voltage pulses are applied to the emitter from a pulse generator. A box-car detector is used to obtain the mean amplitude of the noisy signal. The scan delay generator produces a window pulse, triggered by the pulse generator, and the linear gate averages the signal within the pulse while reducing the noise through a low-pass filter. The amplified detector-response and the pulse across the emitter are viewed on an oscilloscope screen. The voltage from the linear gate is recorded on an x-y recorder, with the magnet power supply driving the x-axis.

## Section IV: Results on Cyclotron Emission in Germanium

### Characteristics of Sample

All of the results obtained on cyclotron emission in germanium have been taken from one sample of n-type material which comes from the Hoboken Company in Belgium. The concentration of this sample was given as  $2 \times 10^{12} \text{ cm}^{-3}$ . This was checked in a rough way by measuring the sample resistance as the sample was cooled by 20 or 30° below room temperature. The relation between sample resistance R and carrier concentration n, considering only the electrons as carriers, is:

$$n = \frac{d}{eA\mu} \frac{1}{R}$$

where A and d are the sample cross-sectional area and the contact spacing, respectively, and  $\mu$  is the mobility. In this temperature region,  $\mu$  does not change appreciably, so  $n \propto 1/R$ . At room temperature, the intrinsic concentration  $n_i$  in germanium is about  $3 \times 10^{13} \text{ cm}^{-3}$ . With a small drop in T this intrinsic conduction is lost and only extrinsic conduction remains. R was measured to be  $330\Omega$  at room temperature. As the sample cooled 20 or 30°, the resistance rose by a factor of seven to  $2.3k\Omega$ . We can calculate  $n = 1/7 n_i = 4 \times 10^{12} \text{ cm}^{-3}$ . This is in agreement with the given value within a factor of two. If we had included the temperature dependence of the mobility, n would have been slightly lower.

Current-voltage characteristics were taken at 4.2°K in zero magnetic field and at 3.6 Tesla. This was done with the sample in both longitudinal and transverse orientations and dc electric fields were used. At 3.6T, the non-Ohmic resistance at high electric fields (in the region of 150 V/cm) was found to be  $130k\Omega$  in the transverse orientation and  $20k\Omega$  in the longitudinal orientation. The difference is explained by the greater magnetoresistance in the transverse

orientation. At zero magnetic field, the high electric field resistance in both orientations is about  $5k\Omega$ . Using  $n = 2 \times 10^{12} \text{ cm}^{-3}$ , the mobility is calculated to be  $45,000 \text{ cm}^2/\text{V-s}$ . This is about seventy times lower than the value calculated from the temperature dependence,  $\mu \propto T^{-1.66}$ . However, this relation is only approximate and does not take into account ionized impurity scattering. Also, at these large electric fields the electron temperature is considerably higher than the lattice temperature. At  $3.6T$ , the threshold electric field for observation of current was  $125 \text{ V/cm}$  in the transverse orientation and  $56 \text{ V/cm}$  in the longitudinal orientation. Both these values are consistent with the observed threshold for emission. Hysteresis is observed above the threshold in both orientations, which indicates lattice heating. Since the emission experiments were done with pulsed electric fields, however, less heating will be expected at a given field than observed in these curves.

#### Impurity Spectrum

Figure 4.1 shows the photoconductivity spectrum of the germanium sample taken in zero magnetic field. This shows the presence of different impurities and gives an indication of the quality of the sample. Beginning at about  $65 \text{ cm}^{-1}$ , a series of peaks are seen corresponding to the photothermal ionization of donors from bound impurity states to the conduction band in the two-step photoconductivity process described earlier. These peaks can be identified using the energies found by Seccombe and Korn (32) and Skolnick (33), which have been found to be in fair agreement with those calculated by Faulkner (34). Phosphorus is seen to be the dominant impurity, with the  $1s - 2p$  and  $1s - 3p$  lines strongly resolved. The  $1s - 4p$  line is not seen, but weak peaks can possibly be associated with the  $1s - 4f$  and  $1s - 6p$

transition energies. At lower energies, the 1s - 2p and 1s - 3p transitions for lithium can also be clearly seen, though the 1s - 4p transition observed by Seccombe and Korn is not seen. Between the two Li peaks, another peak at  $69 \text{ cm}^{-1}$  is observed which is not identified. The broad shoulder between 70 and  $80 \text{ cm}^{-1}$  corresponds to antimony, but the separate transition lines are only very weakly resolved. The unknown impurity which is labelled C is only weakly present; only the 1s - 2p transition line is seen. This impurity is believed to be associated with defects in the crystal such as vacancy clusters.

The peaks in this spectrum are not as distinct as they might be, because only a low-resolution spectrum has been taken here. Another consideration is the way the spectrum is affected by temperature. The probability for thermal ionization from an excited impurity level with energy  $E_{\text{ex}}$  to the conduction band  $E_{\text{c}}$  is described by:

$$P_{\text{ion}} \propto \exp\left(\frac{E_{\text{c}} - E_{\text{ex}}}{kT}\right)$$

As can be seen in figure 4.2, the transition lines become much stronger at temperatures greater than  $4^{\circ}\text{K}$ . It would be desirable to take this spectrum again at a higher temperature and with greater resolution.

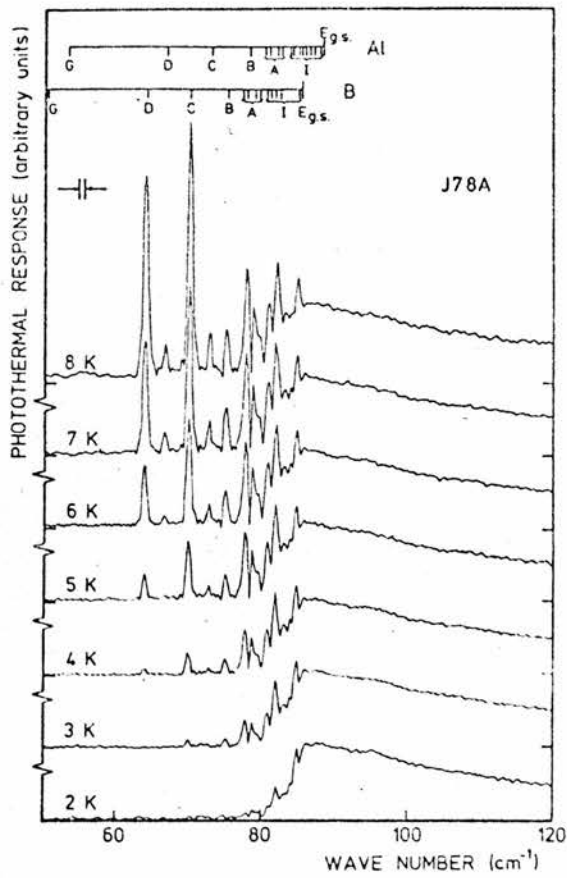


Figure 4.2

Photoconductivity spectra of germanium at temperatures from 2 - 8°K.

FIG. 4. Photoconductivity spectra at several temperatures of the monocrystalline germanium sample J78A. Impurity concentration B:  $2.1 \times 10^{11}$  atoms/cm<sup>3</sup>, Al:  $4.3 \times 10^{10}$  atoms/cm<sup>3</sup>.

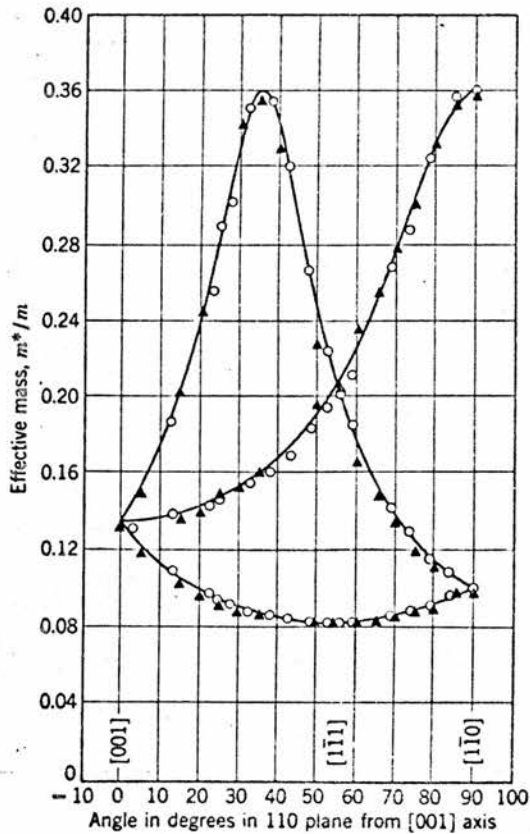


Figure 4.3

Effective cyclotron mass of electrons in germanium for magnetic field directions in a (110) plane.

## Cyclotron Emission Experiments

### Position of Peaks

As described in section III, the magnetic field position of the photoconductivity peak of the detector can be used to find the effective mass of the emitting sample, using the relation:

$$\frac{m^*}{m_0} = \frac{eB}{2\pi c \bar{D} m_0} .$$

In germanium, the effective mass in a magnetic field is a function of the orientation of the sample in the field (figure 4.3). The longitudinal direction of the sample was found to be the  $\langle 110 \rangle$  direction. The transverse orientations of the sample are therefore in the (110) plane. The transverse orientation used was found to be in the  $\langle 111 \rangle$  direction. As can be seen from figure 4.3, more than one effective mass is present for most orientations, corresponding to the four ellipsoids in the conduction band. Peaks were seen corresponding to the different masses in the  $\langle 110 \rangle$  and  $\langle 111 \rangle$  directions. The values of these are shown in figure 4.4. We have also done cyclotron resonance experiments on this sample in a longitudinal orientation and these results are included. The different sets of values given in figure 4.4 correspond to different sets of experiments. It was found that the sample orientation changed by 5 or 10° between different days, which has a large effect since the effective masses are sensitive to orientation. In future experiments it would be worthwhile having more control of the sample orientation. It would be interesting to be able to turn the sample by 55° and look at the emission in the  $\langle 100 \rangle$  direction where only one effective mass is seen.

Figure 4.4. Effective masses in germanium found in cyclotron emission and cyclotron resonance.

<u>Cyclotron emission</u>	<u>Magnetic field position</u>	<u>Detector frequency</u>	<u>Effective mass</u>
<u>Transverse orientation</u>			
first run	2.99 T	32.5 cm <sup>-1</sup>	.086 m <sub>0</sub>
second run	3.51	33.5	.097
third run (high field)	6.45	32.5	.185
	6.75		.194
<u>Longitudinal orientation</u>			
	3.54	34	.098
	3.94		.108
<u>Cyclotron resonance</u>			
<u>Longitudinal orientation</u>			
first run	.378 T		.096
	.397		.101
	1.345		.342
	1.399		.355
second run	.347		.088
	.465		.118
	.960		.244
	1.396		.355

Note: The frequency  $\bar{\nu}$  of the  $1s - 2p$  impurity transition is slightly field-dependent. The method for estimating the detector field and hence calculating the detector frequency is in appendix A.

## Linewidths

### Transverse orientation

The first series of experiments attempted used very long pulses of electric field, about 3 - 4 msec long (duty cycle about 1:2). This gave a very large peak but caused considerable heat broadening of the linewidth. The relation between the linewidth in terms of  $\omega\tau$  and the electric field is shown in figure 4.5. The relation is linear and  $\omega\tau$  is small. The threshold electric field for emission was 125 V/cm. The maximum  $\omega\tau$  measured was  $\omega\tau = 27$ , at an electric field of 146 V/cm.

In later experiments, shorter pulses on the order of .5 msec (duty cycle about 1:18) were used. This did give sharper lines, but it also gave much smaller signals with worse signal-to-noise. An example of a cyclotron emission signal is in figure 4.6. The worse signal makes a greater error in measuring the linewidth. The estimate of the error in these measurements is at least 10%. The relation between the linewidth and the electric field is shown in figure 4.7. It can be seen that there are two approximately linear regions. For fields above about 250 V/cm, the line has about the same slope as in the previous graph. This means that while there is less heat broadening of the lines with shorter pulses, the relation between field and linewidth is the same for fields above a certain value. For fields below 250 V/cm, there is a second region with a much steeper slope. Here there seems to be less significant heating and  $\omega\tau$  gets much larger with decreasing electric field. The smaller signal caused the threshold to observe emission to be higher, about 167 V/cm. Higher electric fields were obtained by using closer contacts on the sample. The maximum  $\omega\tau$  measured was  $\omega\tau = 89$  at a field of 192 V/cm. At  $34 \text{ cm}^{-1}$ , this is equivalent to a linewidth of  $.4 \text{ cm}^{-1}$ .

Figure 4.5

Transverse cyclotron emission.

Linewidth vs. electric field with high  
electron heating.

Duty cycle 1:2.3

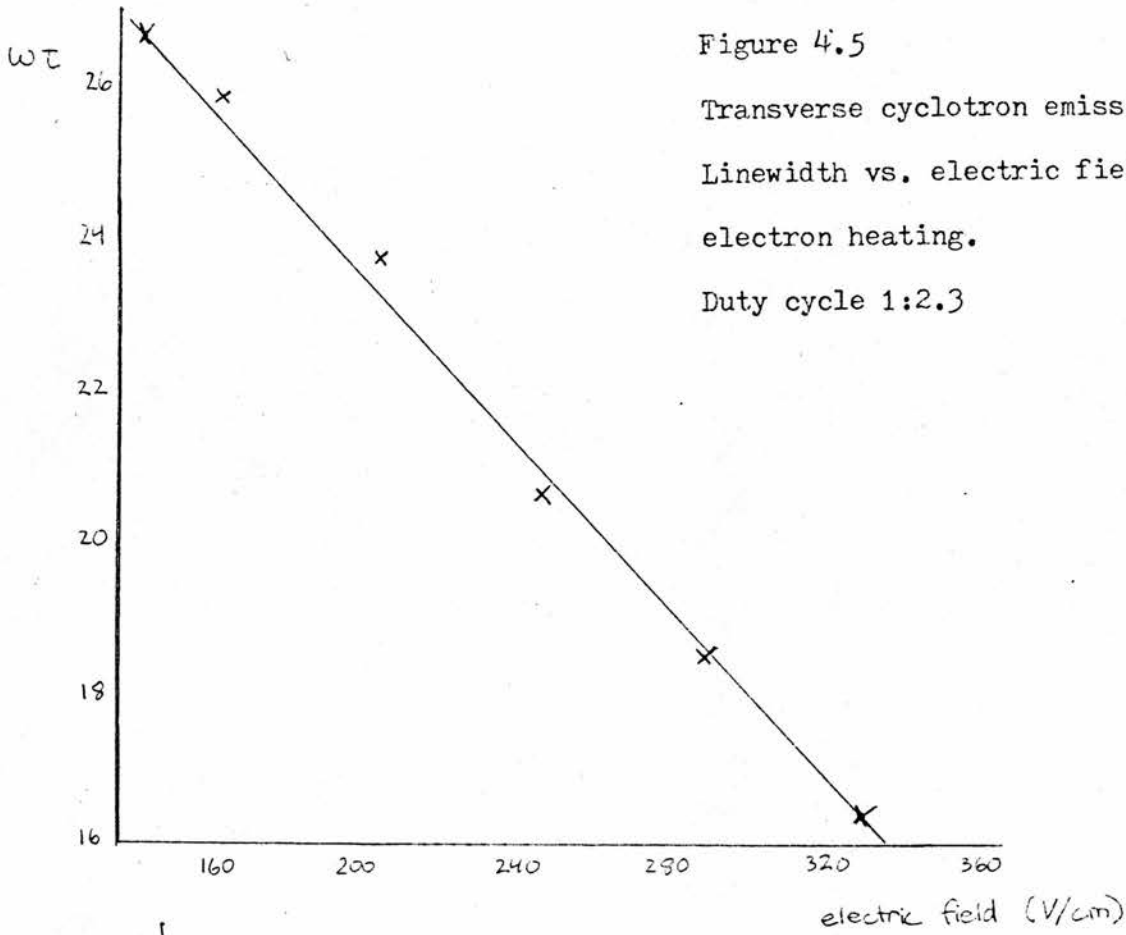
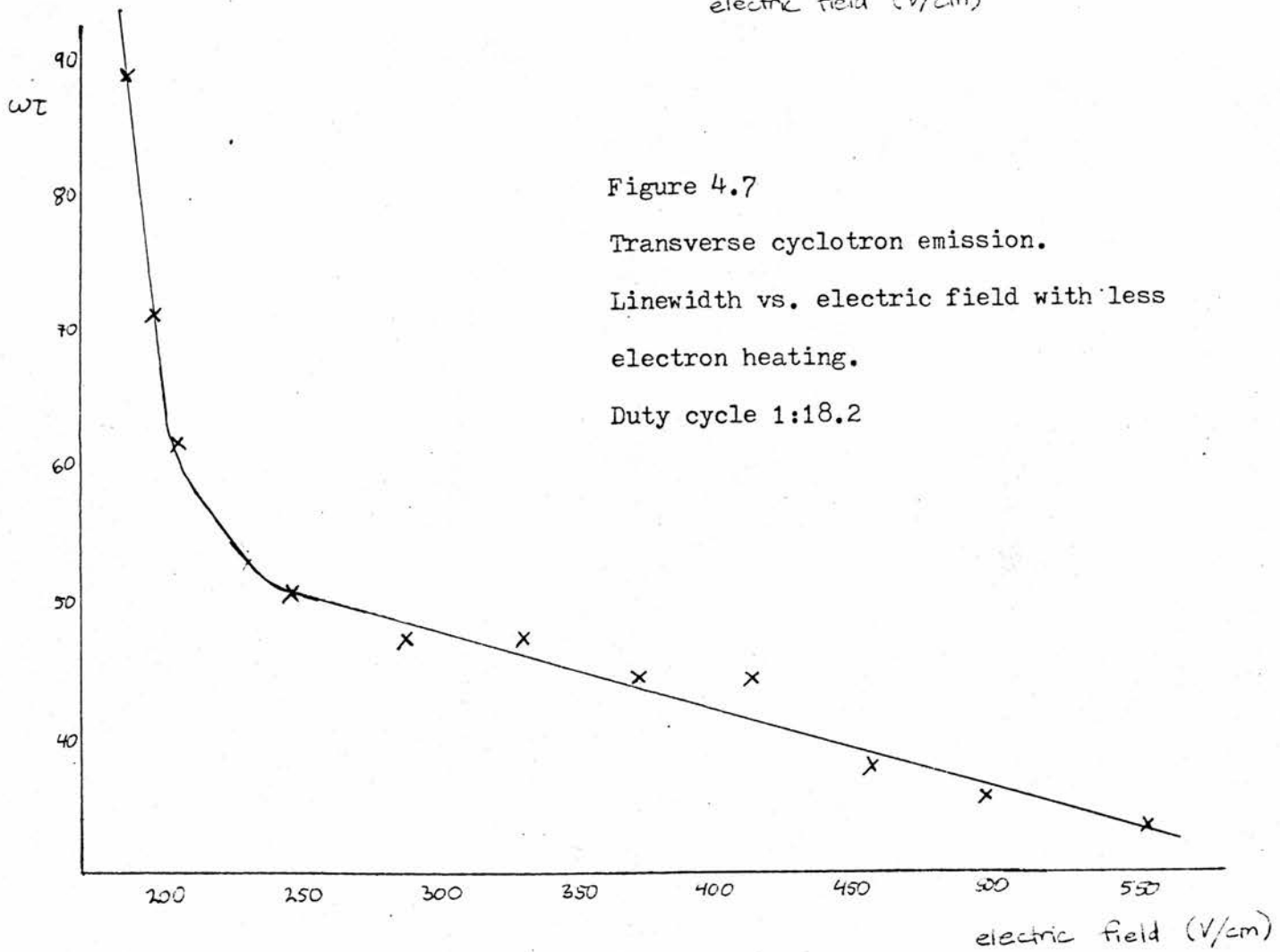


Figure 4.7

Transverse cyclotron emission.

Linewidth vs. electric field with less  
electron heating.

Duty cycle 1:18.2



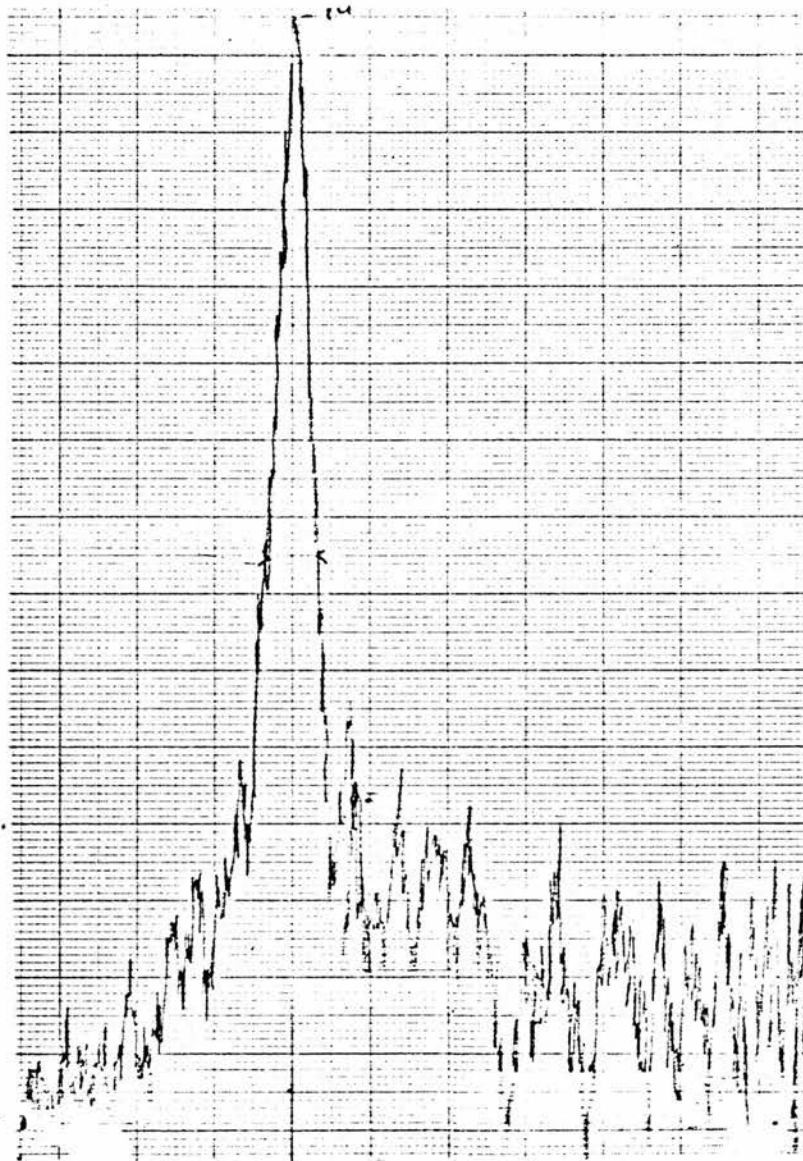


Figure 4.6

Example of cyclotron emission in germanium

Transverse orientation

$E = 400 \text{ V/cm}$

### Longitudinal orientation

For these runs, short pulses of about .5 msec were used, and a relation between  $\omega\tau$  and electric field similar to that in a transverse orientation with regions of different slope was found. Signal could be observed at lower electric fields in this orientation, with a threshold of 83 V/cm. A lower  $\omega\tau$  was seen, which may be expected since the higher power obtained in the longitudinal orientation indicates that there is more electron heating. The maximum  $\omega\tau$  was  $\omega\tau = 71$  at 97 V/cm. The higher effective mass peak ( $m^* = .11 m_0$ ) gave a lower  $\omega\tau$ , with a maximum value of  $\omega\tau = 50$ . This is probably because of the anisotropy in  $\tau$ . Since the relaxation time depends on the number of states available for scattering, it varies between the different valleys in a given direction. Also, if the effect of inter-valley scattering is not large, the electrons in different valleys can be at different temperatures.<sup>(35)</sup> The error in these higher field measurements is larger because the detector signal becomes increasingly noisy at higher magnetic fields. The results for  $\omega\tau$  versus electric field in the longitudinal orientation are in figure 4.8.

### Detector linewidth

As mentioned before, the observed linewidth is the convolution of the emission and detector linewidths. This means that while we can comment on the variation of linewidths with electric field, we cannot really say what the emission linewidth alone is. We can find the detector linewidth by taking a photoconductivity spectrum of the detector with the Fourier transform spectrometer. This gave the detector linewidth as  $.5 \text{ cm}^{-1}$  in zero field and  $.3 \text{ cm}^{-1}$  at 4.5 T. At 3 T, the linewidth is probably about  $.35 \text{ cm}^{-1}$ , giving an  $\omega\tau$  of 97. The linewidth for the impurity transition comes from the

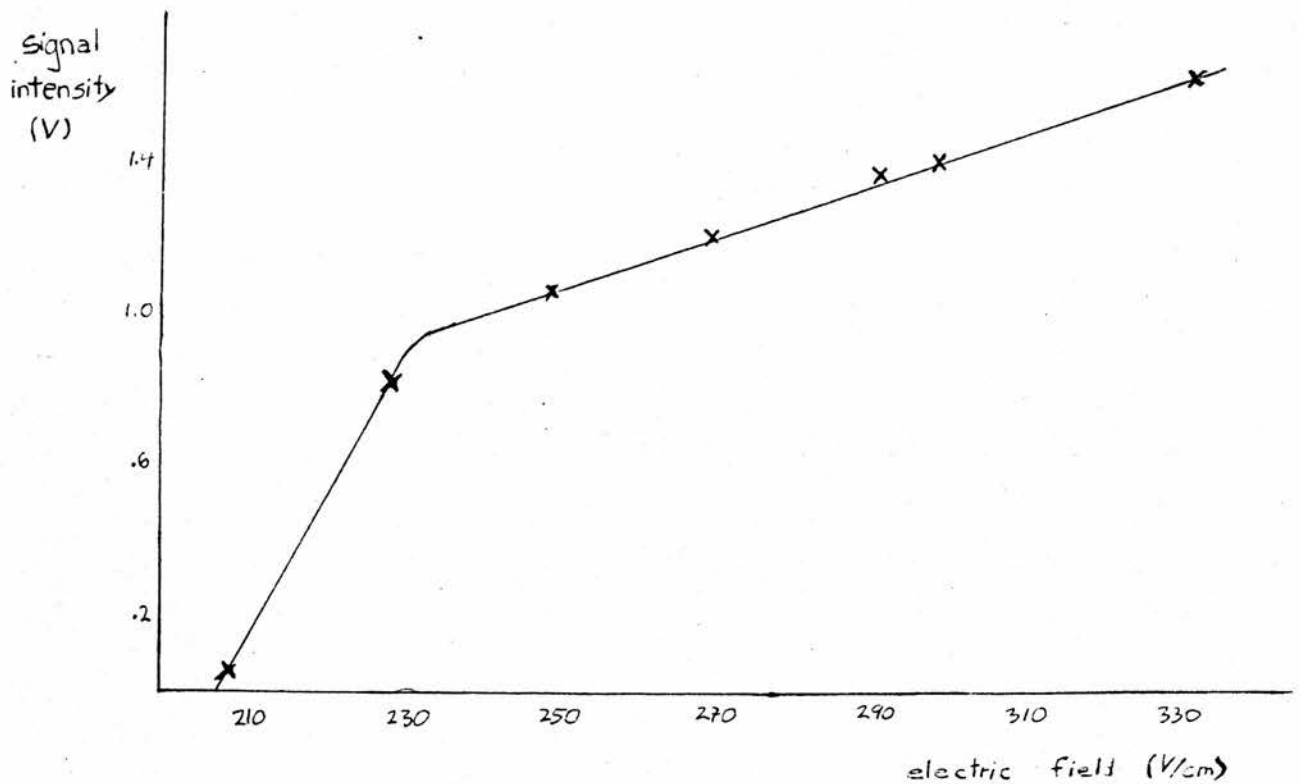
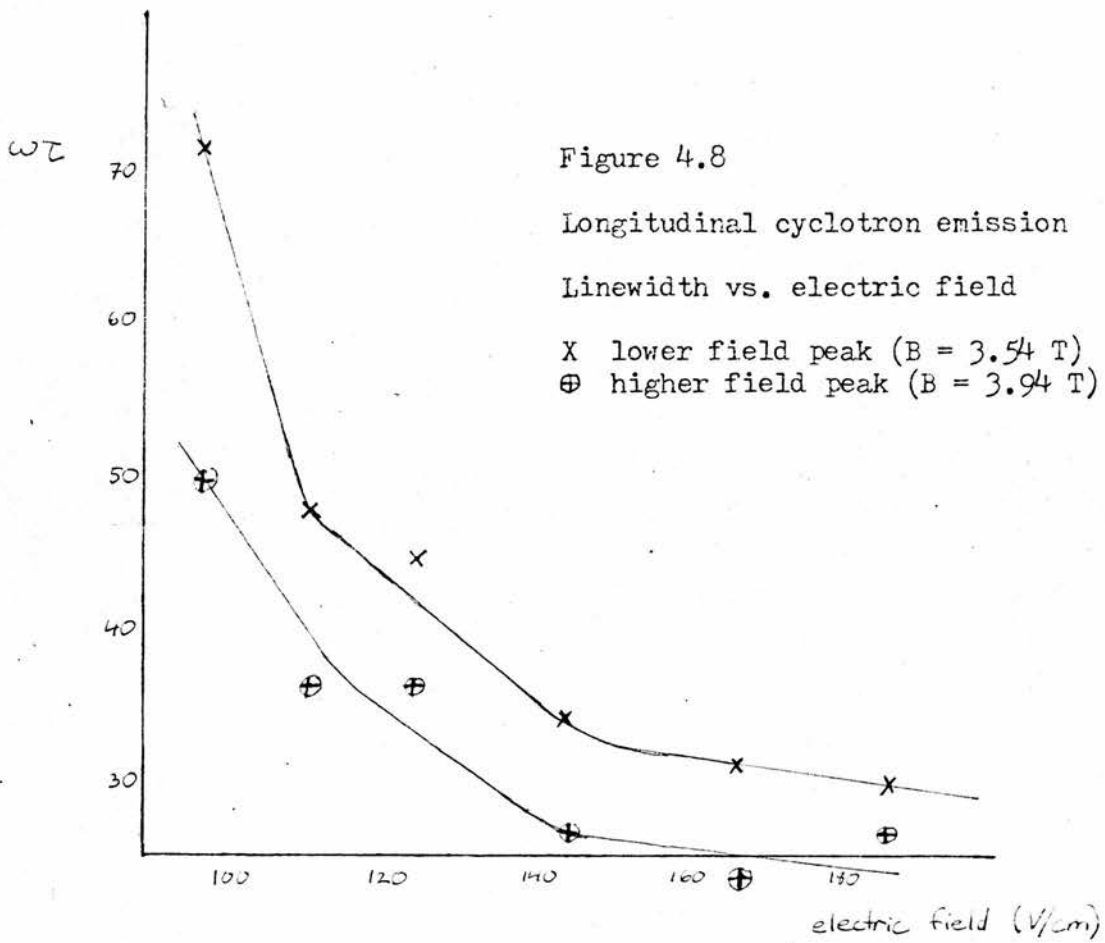


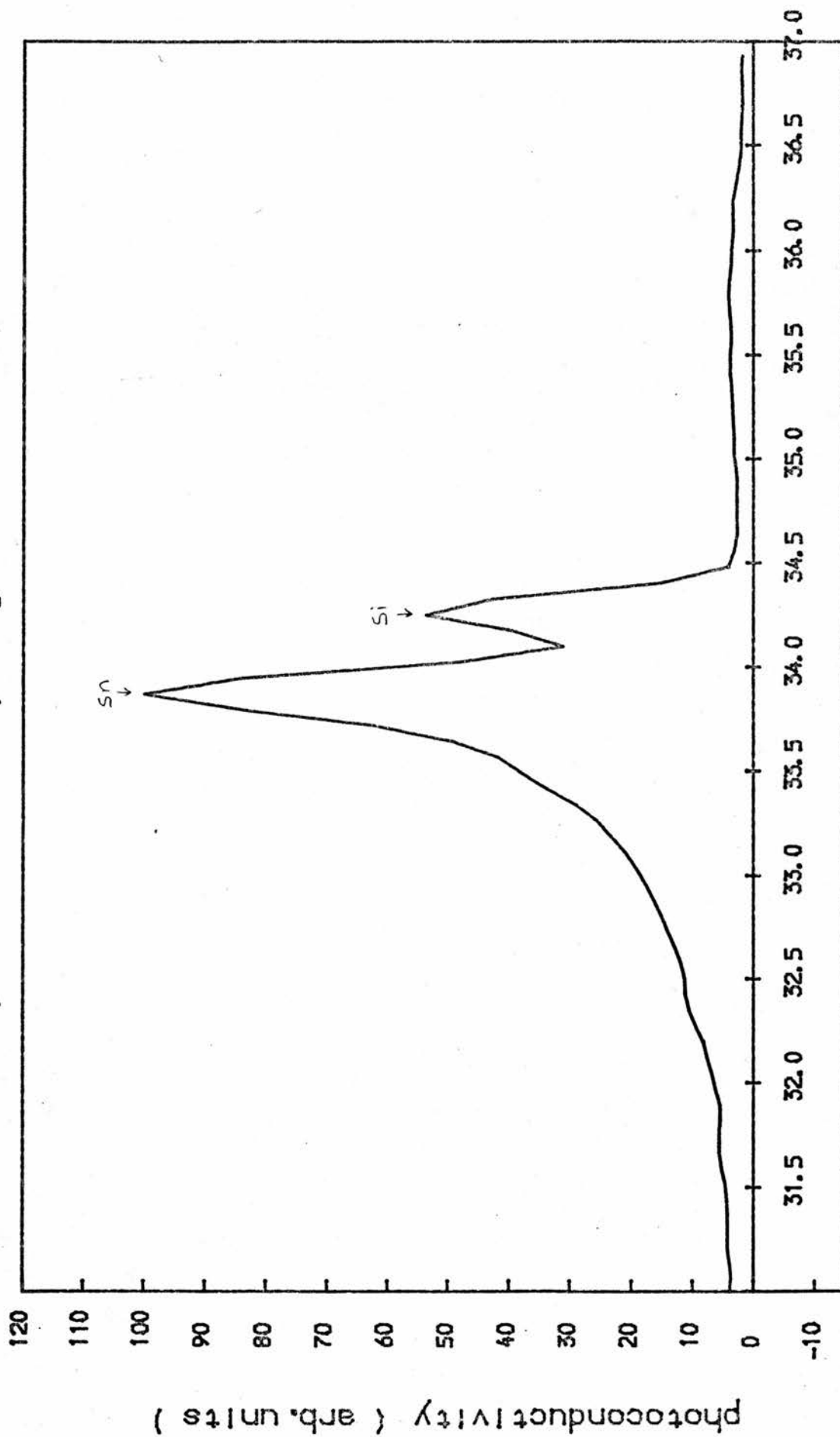
Figure 4.10 Transverse cyclotron emission. Intensity vs. electric field.

spread in electric field due to the spatial distribution of impurities. In a magnetic field, the donor wave functions contract and so the effect of the Stark broadening is reduced (36). The spectrum of the detector at 4.5 T is shown in figure 4.9. The  $1s - 2p^-$  peak is shown and it can be seen to be split due to the central cell effect.

#### Intensity

The height of the emission signal in the transverse orientation was measured for different electric fields. Since the detector linewidth has been measured to be less than the emission linewidth, it is the peak intensity and not the integrated intensity which is observed. From the threshold at about 200 V/cm to about 250 V/cm the intensity increased sharply with field. Above this value, the increase in intensity with field is less sharp. This is shown in figure 4.10. It can be seen that the intensity of the signal begins to decrease steeply at the same electric field at which the linewidth begins to decrease steeply, illustrating that this is where the heating is less significant. When using cyclotron emission as a source of radiation, these two effects will have to be optimized. This means that a certain amount of line broadening would have to be accepted in order to produce a sizable signal, or else a sharp but weak signal would have to be used.

photoconductivity of gas detector



frequency ( cm-1 )

Figure 4.9

### Cyclotron emission in III-V compounds

We have also done cyclotron emission experiments with GaAs, InP and InSb. Similar to the work on Ge, the variation of intensity and linewidth with pulsed electric fields were studied. The lines were not found to be as narrow as in Ge, since the samples were not as pure, but the examples in figure 4.11 show that very strong signals with good signal-to-noise levels were achieved. The variation of intensity with electric field is shown in figure 4.12 for InP. The threshold for emission is 10 V/cm. After an initial steep increase, the variation in intensity with field is approximately linear. A graph of linewidth versus field is shown in figure 4.13 for GaAs and InP. For both materials,  $\omega\tau$  is seen to decrease with increasing field from a maximum of about 21. For GaAs, the points do not lie on a smooth curve, which can be explained by the inaccuracy in the measurements. Error bars are included to account for a 10% error.

The two examples of InSb emission shown in figure 4.14 were taken with similar conditions but with different orientation. The longitudinal run shows the expected sharp lineshape, while the transverse run is broadened by a low field shoulder. This effect is also seen in GaAs, though less pronounced, and the explanation is not known. Gornik has attributed a low field shoulder to thermal emission from hot electrons (11), but it is not known why this effect should be orientation-dependent.

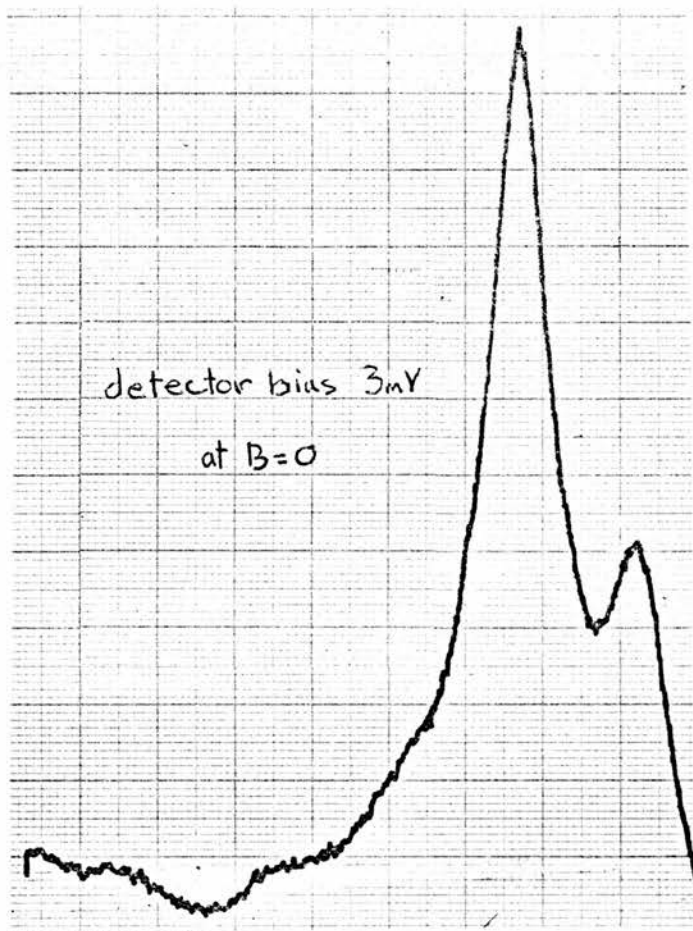


Figure 4.11 Examples of cyclotron emission signals

This page: n-GaAs 5LE200 emitter  $N_D - N_A = 3.4 \times 10^{14} \text{ cm}^{-3}$

n-GaAs E351 detector

Next page: n-InP KV419 emitter

n-GaAs 3LE165 detector

InP KV419 emitter  
GraAs 3LE165 detector



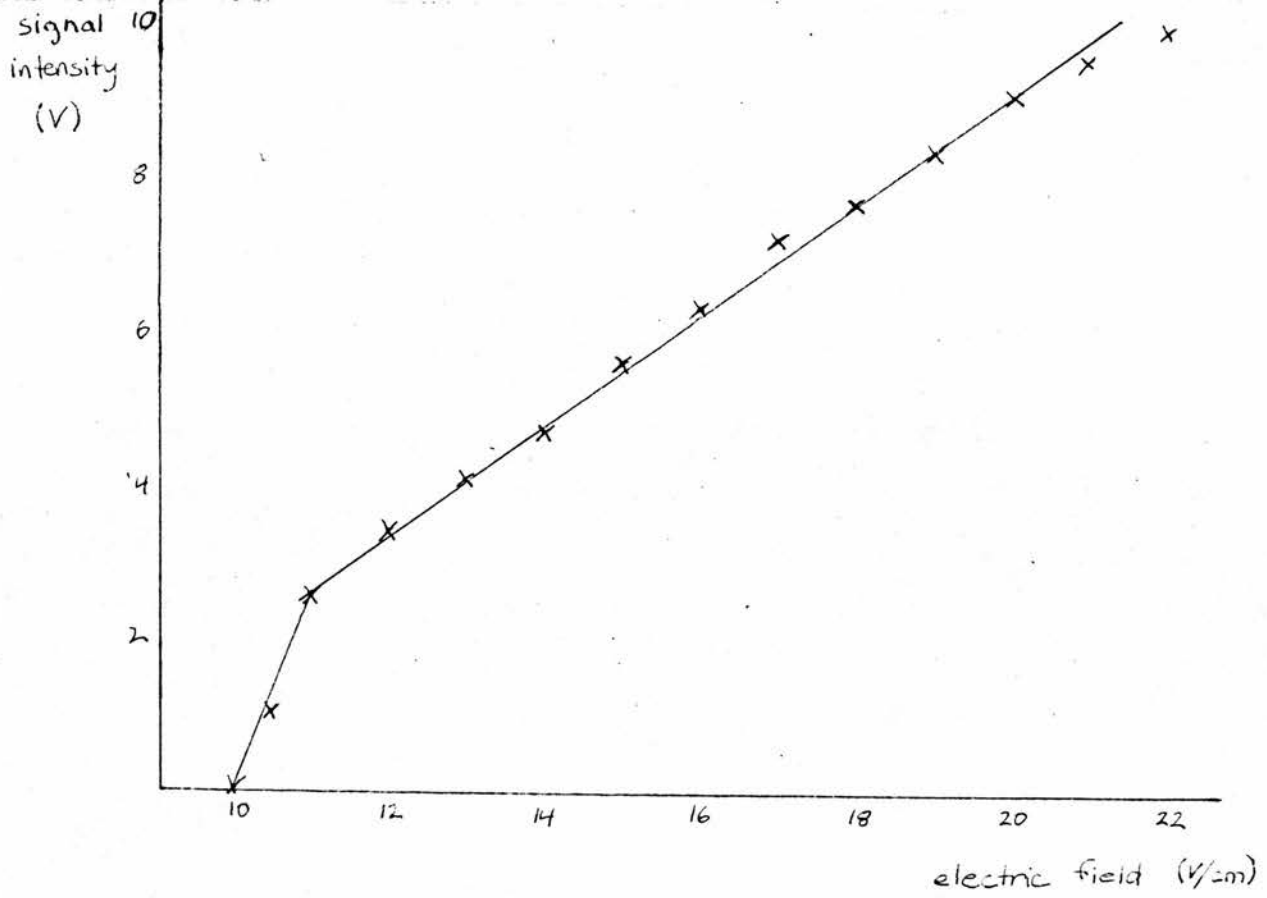


Figure 4.12 Intensity vs. electric field for InP.

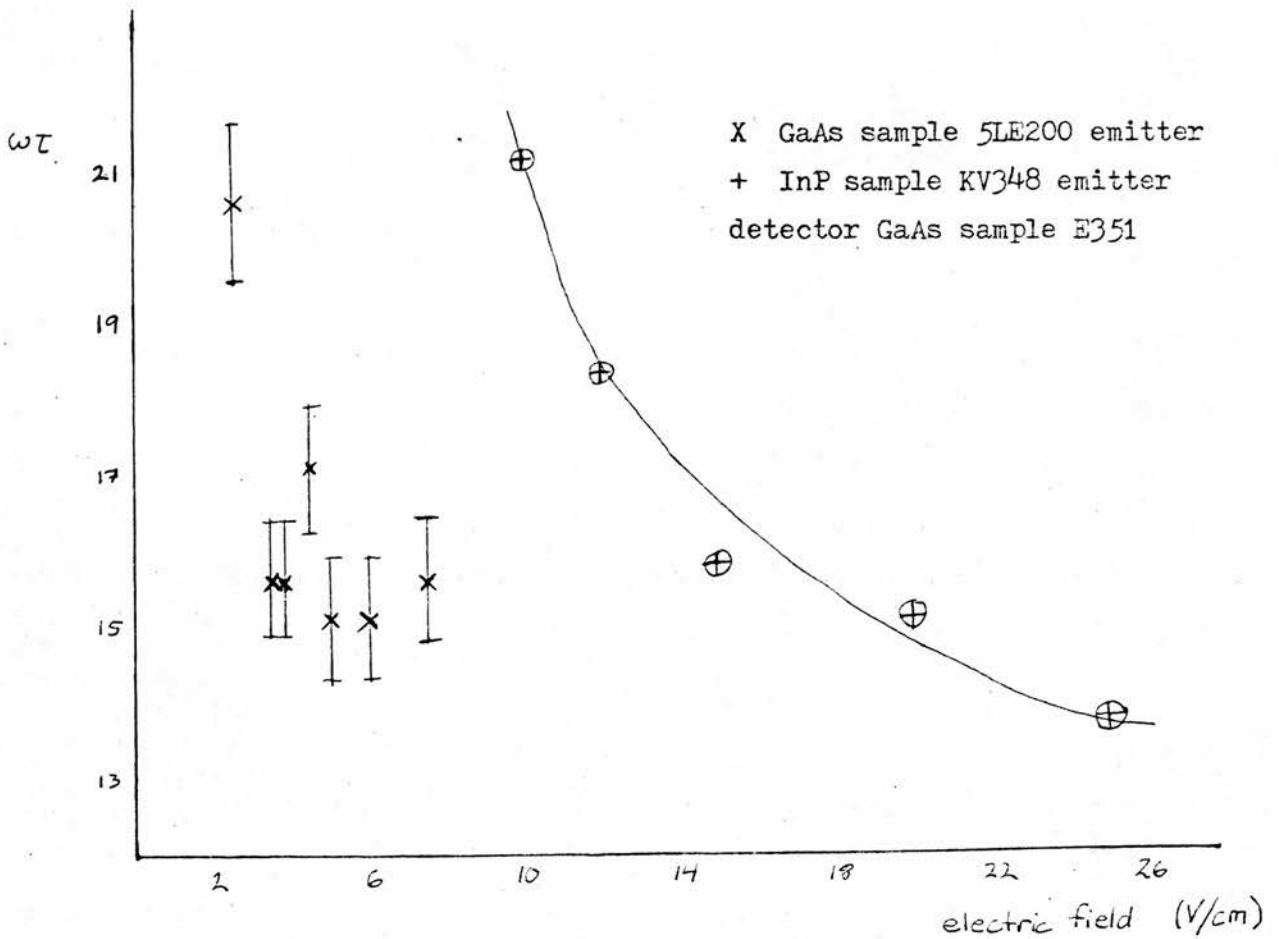


Figure 4.13 Linewidth vs. electric field.

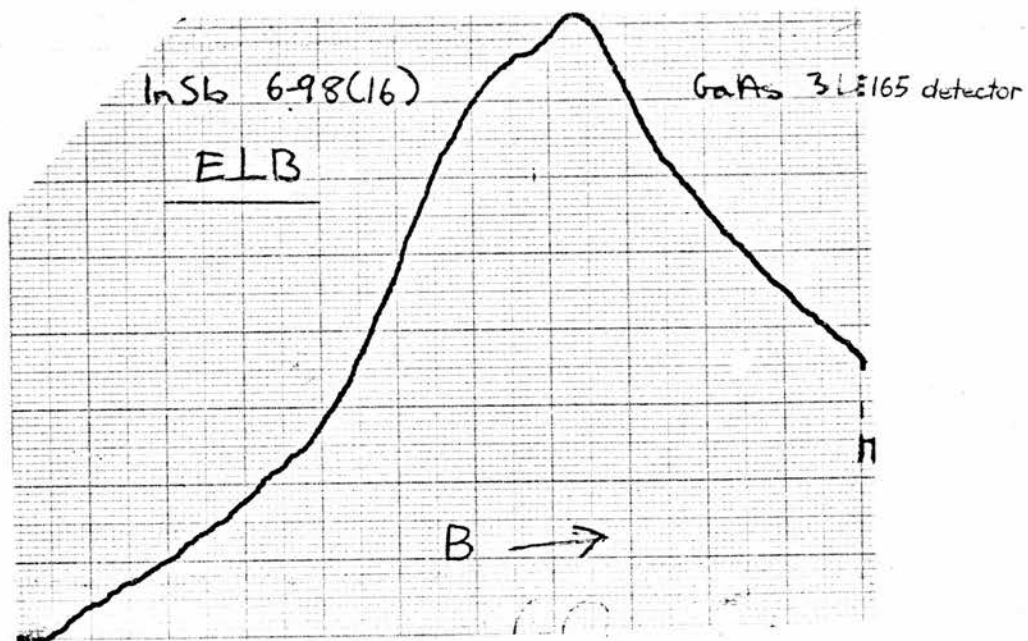
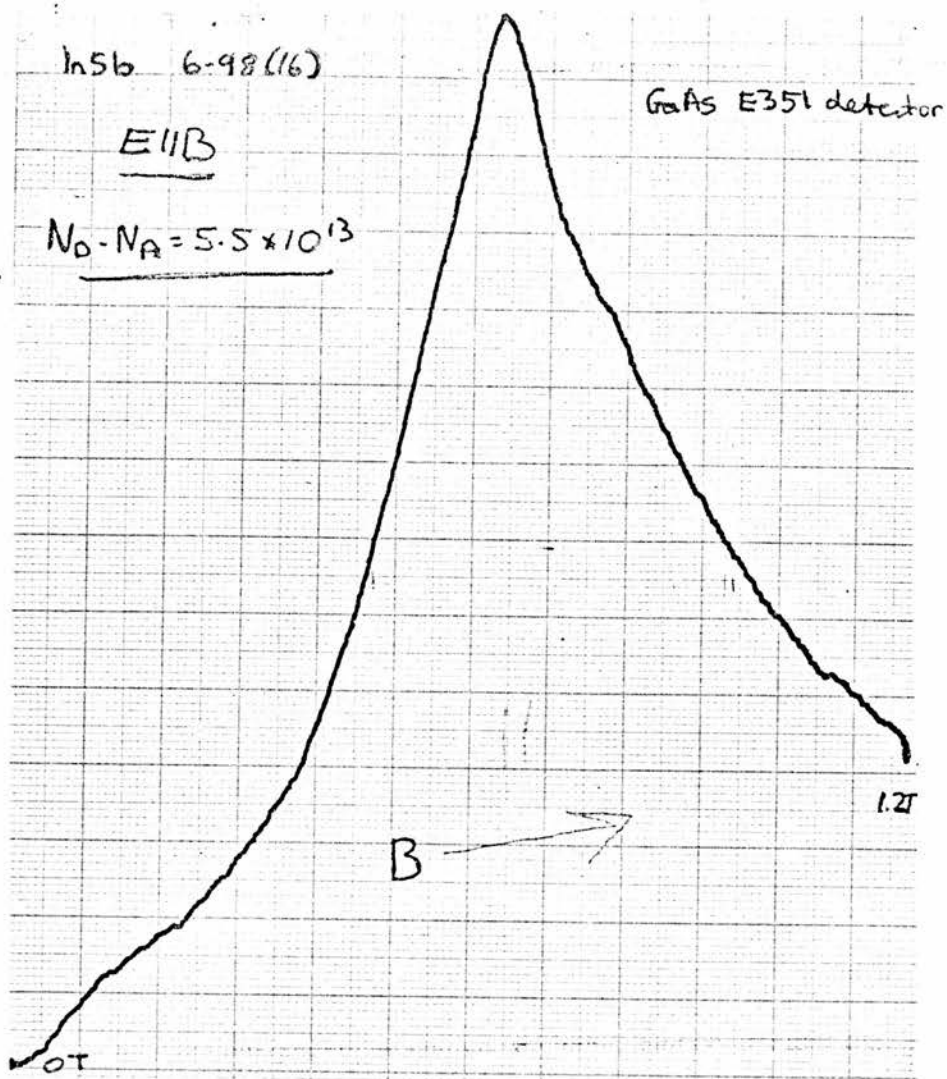
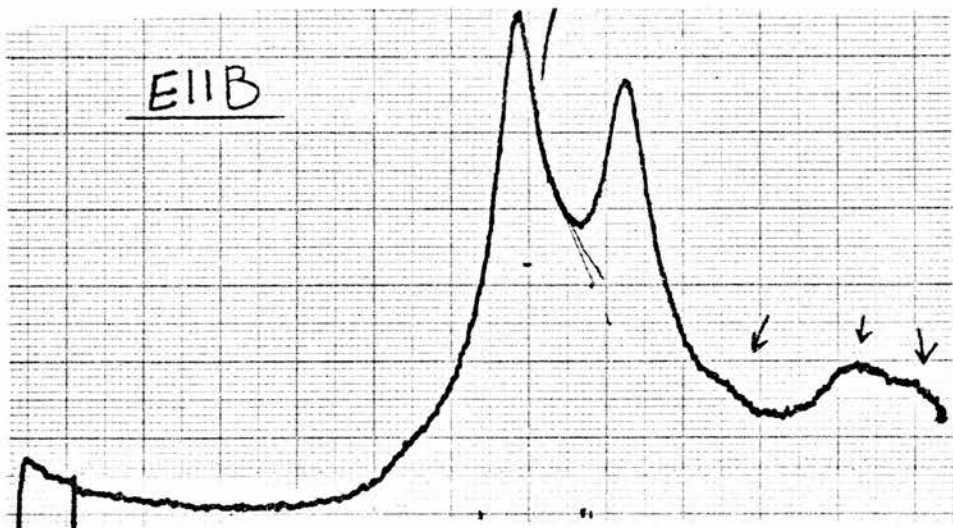
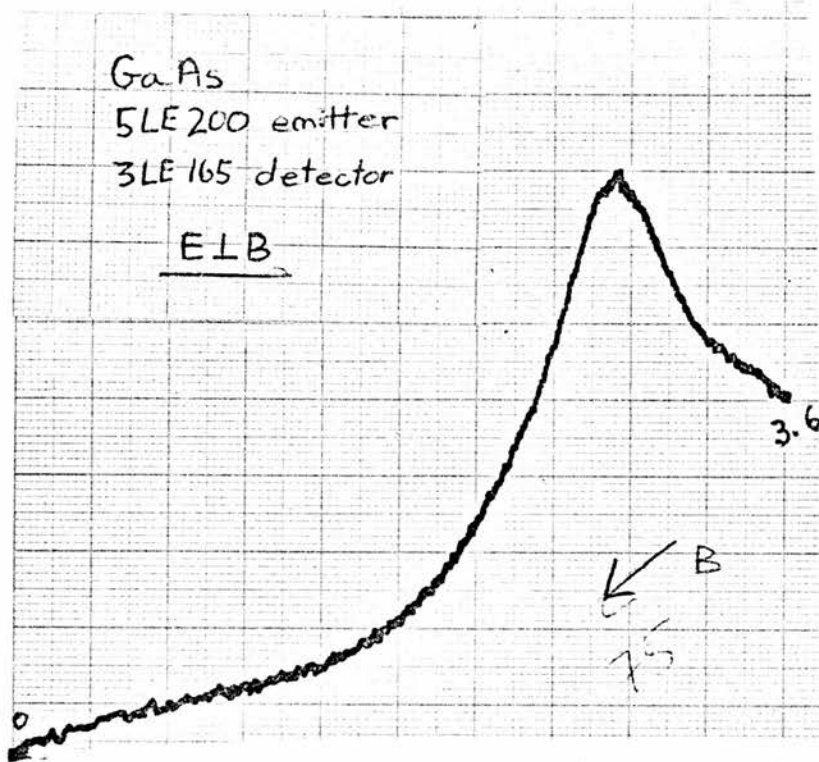


Figure 4.14 Difference in lineshapes in longitudinal and transverse orientations.

This page: InSb emitter

Next page: GaAs emitter

The lower trace on the next page also illustrates that a number of higher transitions may be resolved.



## Section V: Cyclotron resonance experiments

We have also performed cyclotron resonance experiments on the germanium sample in order to compare the linewidths with those in emission. These experiments used an IMPATT diode solid-state microwave source operating at 110 GHz. IMPATT stands for Impact Avalanche Transit Time. In an IMPATT diode, carriers are created in an avalanche process by impact ionization in a narrow p-n junction depletion region. The delay from the transit time of the carriers across a drift region causes the system to oscillate at a frequency given by the drift distance divided by the drift velocity. Sources are commercially available from 20 GHz, to 255 GHz. The power varies from 2.3 W at 40 GHz, to 12 mW at 255 GHz. (37)

The set-up of the cyclotron resonance experiments is in figure 5.1. The radiation from the IMPATT source was chopped by a rotating blade of variable frequency. The resonance was observed using photoconductivity, first using a dc bias for low electric fields, later using higher, pulsed fields of the order of those used in emission. DC fields went from 40 mV/cm to 9 V/cm and pulsed fields from 14 V/cm to 172 V/cm. In the pulsed experiment, greater sensitivity was obtained by detecting the change in voltage with a resistance bridge method as shown. The voltage across the sample was compared to the voltage across a fixed resistor of comparable resistance to the sample.

Cyclotron resonance peaks were easily seen in a longitudinal orientation, an example of which is in figure 5.2. It proved impossible to see any signal in a transverse orientation. This is possibly due to the effect of the large Hall field induced in

this orientation. Two peaks were seen corresponding to two different effective masses. At first these two peaks were seen as just slightly split, then in later runs they split into four separate peaks as the position of the sample shifted.

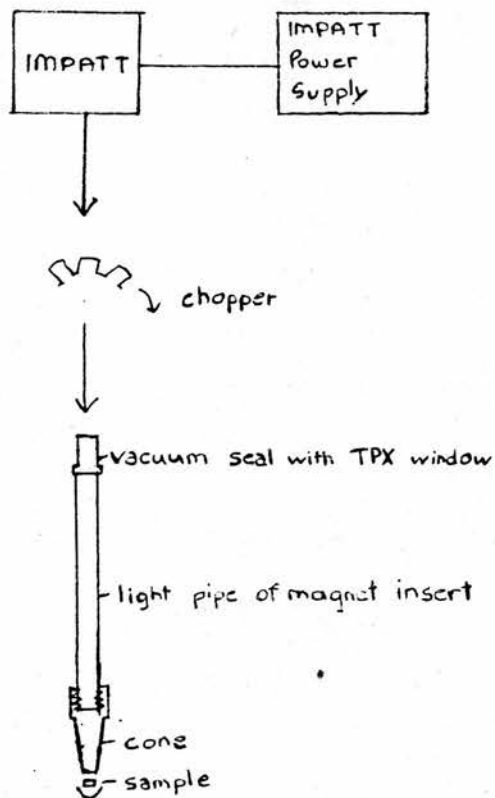
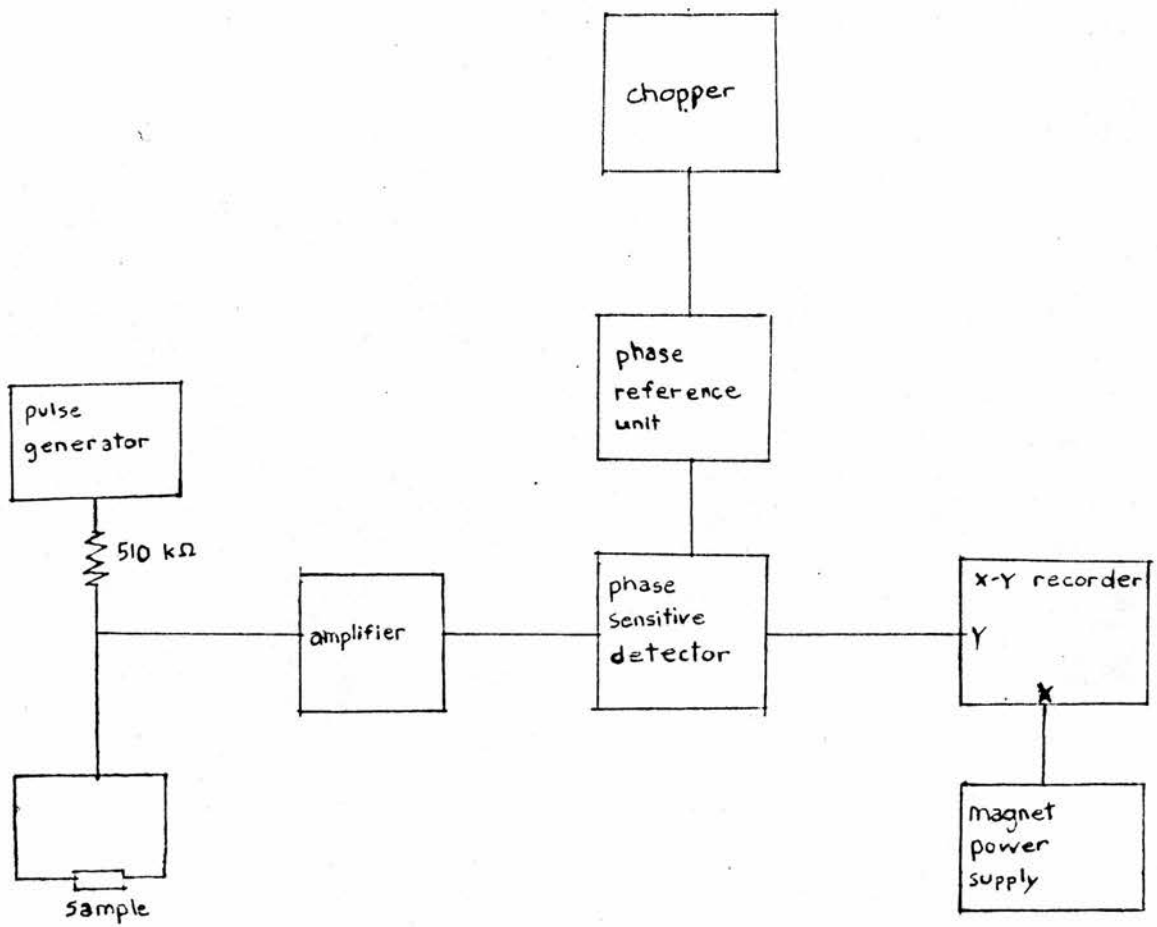


Figure 5.1. Set-up of cyclotron resonance experiment.

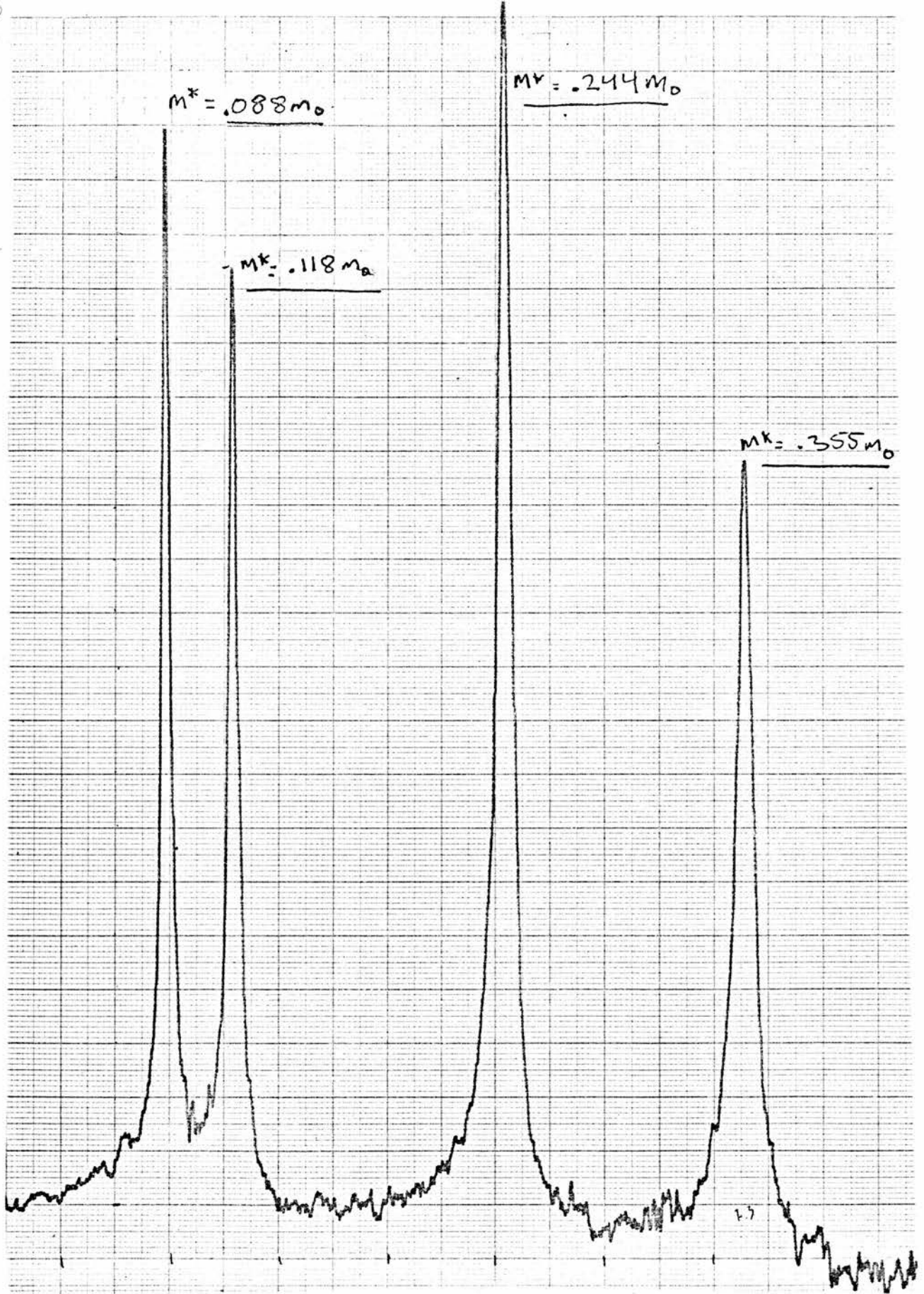


Figure 5.2. Example of cyclotron resonance in germanium. The sample is in a longitudinal orientation and four effective masses are seen. The electric field is 136 mV/cm.

## Results in cyclotron resonance

### IMPATT source power

Before making a study of the linewidths in cyclotron resonance, the effect of the power of the IMPATT source was studied. This is shown in figure 5.3 where it can be seen that the IMPATT power has a large effect on the intensity of the signal. At electric fields above about 100 mV/cm changing the IMPATT power has no effect on the linewidth, but some line broadening can be seen at very low electric fields. The conclusion from this was to do all the experiments using the maximum IMPATT power to get the best signal, except when working at very low electric fields.

### Linewidths at low electric fields

In the first series of runs, as explained above, two sets of lines just beginning to split were seen. A study of linewidth versus electric field was made for these lines, but the linewidths measured are broad because they correspond to two overlapping lines. Still, the variation of linewidth with field can be observed and this is shown in figure 5.4 for low electric fields (below 10 V/cm). The increase in linewidth with increasing field is steeper for fields less than 200 mV/cm. For fields above this, up to 9 V/cm, the increase in linewidth with field is only slight. Linewidth measurements were made again at low electric fields when the sample position had shifted and the lines were well separated. Not many measurements were made in this case, but the few points plotted in figure 5.4 show the same tendency as those for the overlapping lines. Using the optimum conditions of minimum bias and low IMPATT power, a maximum  $\omega\tau$  of 88 for the lowest magnetic field line and  $\omega\tau = 144$  for the highest field line was found. The highest field

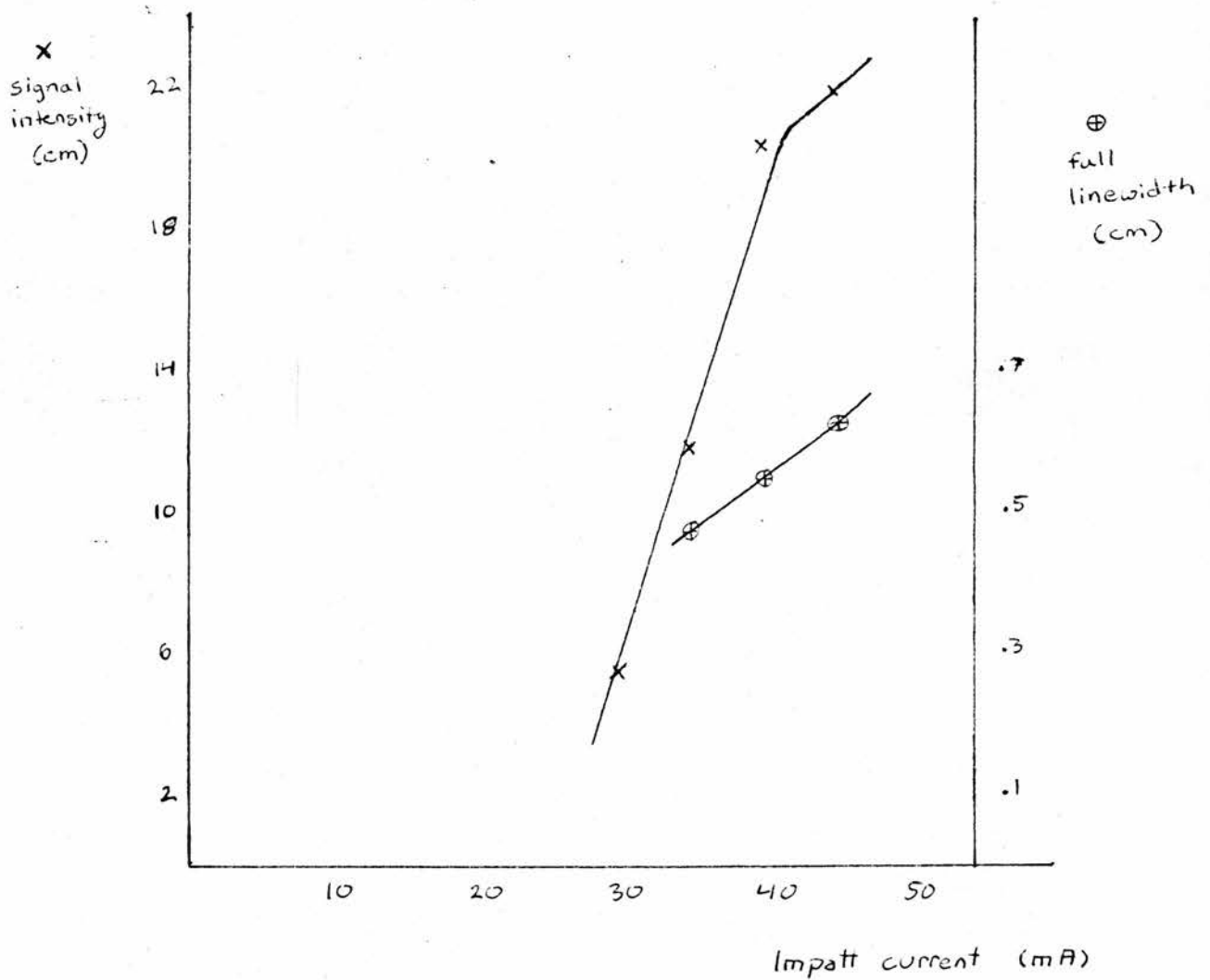
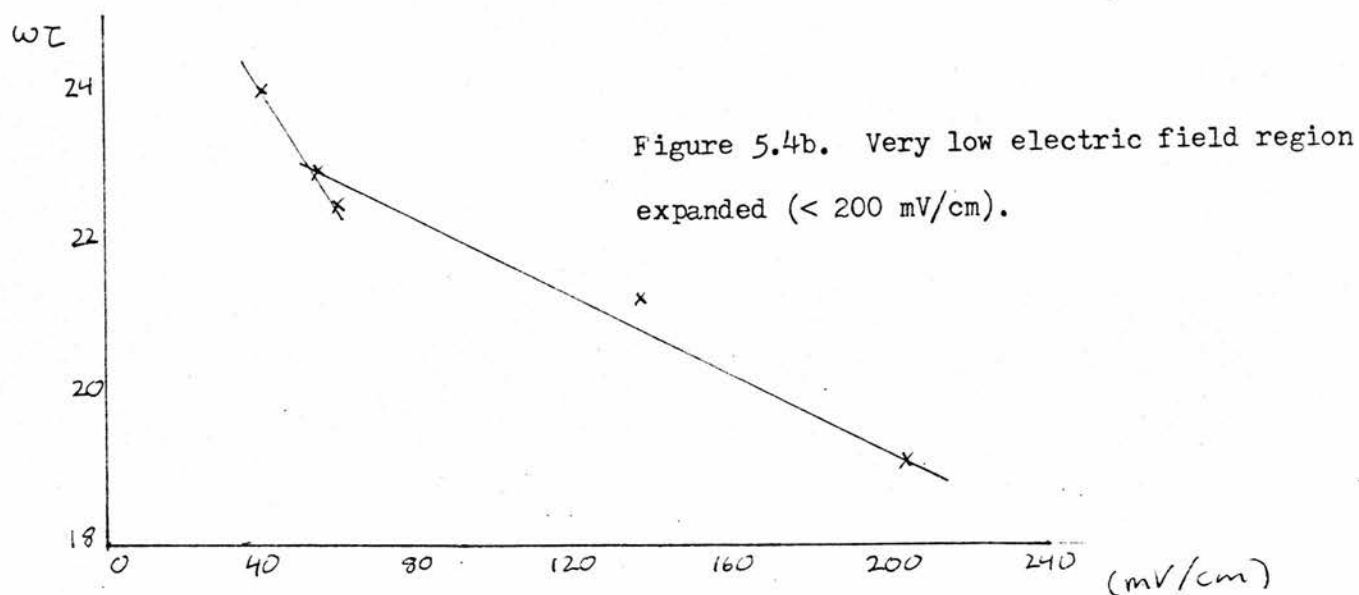
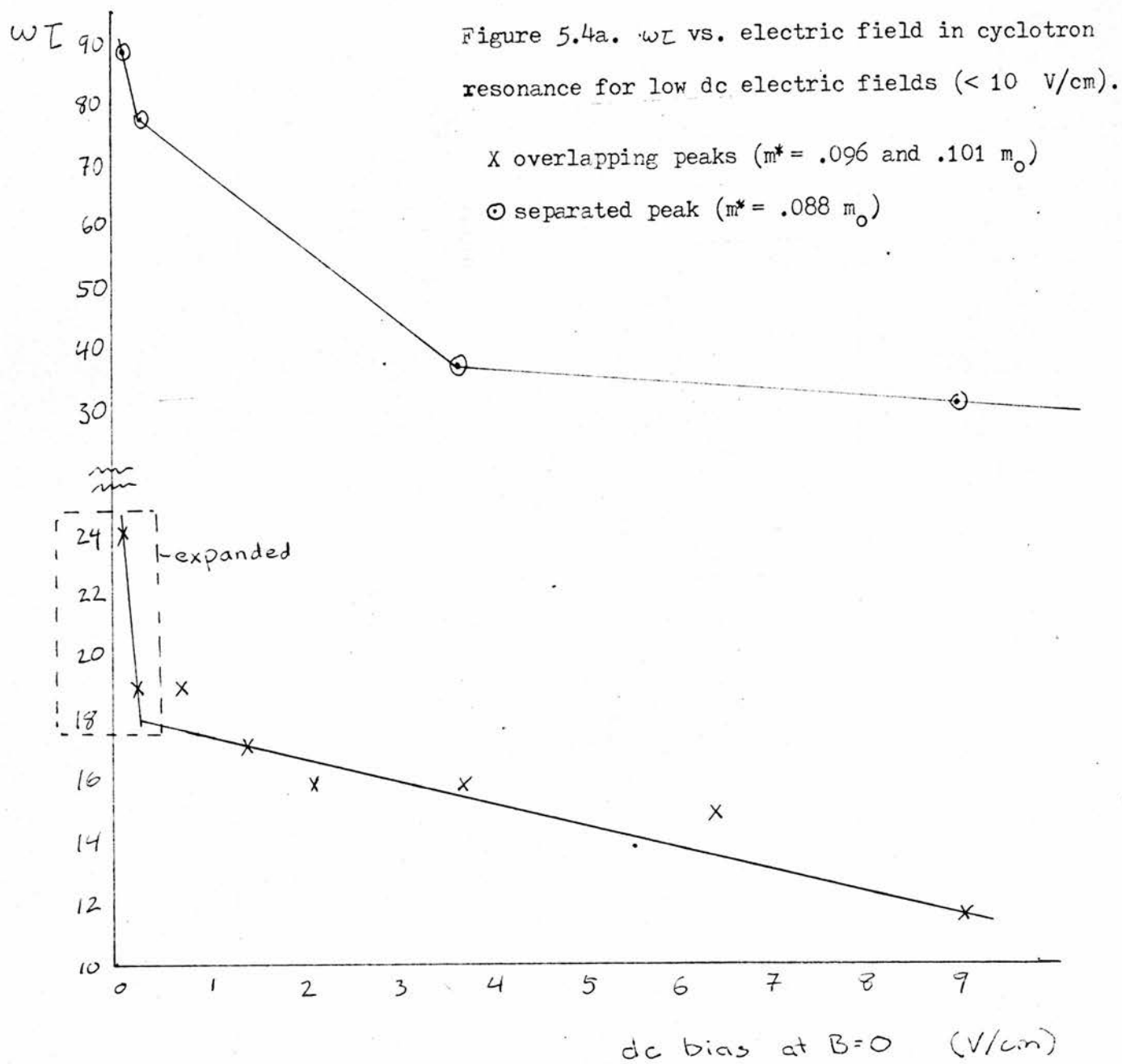


Figure 5.3 Effect of IMPATT current on signal intensity and linewidth. Linewidths were measured with a dc electric field of 48 mV/cm on the sample, and the intensity with 136 mV/cm. The following values of IMPATT power were obtained from a calibration graph which is suspected of being inaccurate.

<u>current</u>	<u>voltage</u>	<u>power</u>
35 mA	18.8 V	0.4 mW
40	19.2	6.6
45	19.6	13.4



line, corresponding to  $m^* = .355 m_0$ , is narrower than the lowest field line which corresponds to  $m^* = .088 m_0$ . This is in agreement with Bagguley, et. al. (35)

#### Linewidths at high electric fields

Cyclotron resonance experiments were done using pulsed electric fields from 9 V/cm to 172 V/cm. The linewidths are less than those with a dc bias for comparable fields, because the pulses cause less heating. Figure 5.5 shows the variation of  $\omega\tau$  with electric field, with the highest dc field point included for comparison. The maximum  $\omega\tau$  was  $\omega\tau = 55$  at a field of 50 V/cm.  $\omega\tau$  falls with increasing electric field as expected, but at the lower field end  $\omega\tau$  seems to fall off with decreasing field. This could be accounted for within the margin of error.

As in emission, the intensity increased with electric field. This is shown in figure 5.6 for electric fields above 80 V/cm.

Figure 5.5  $\omega\tau$  vs. electric field  
in pulsed cyclotron resonance.  
(Longitudinal orientation)

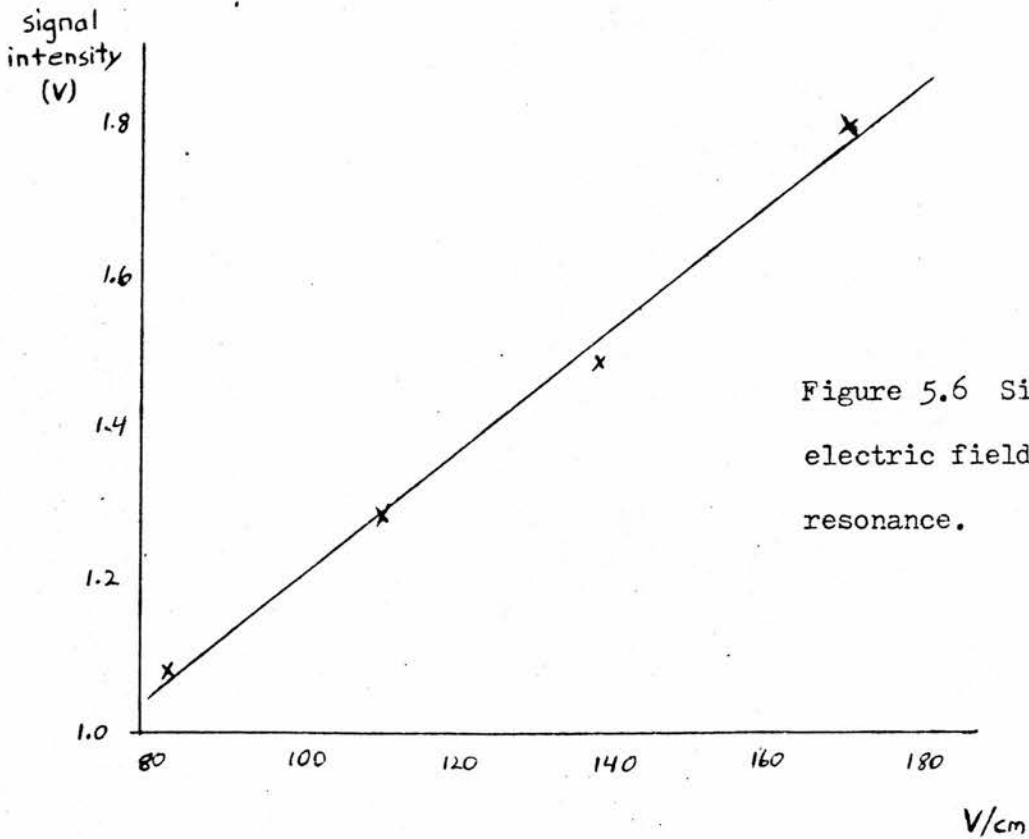
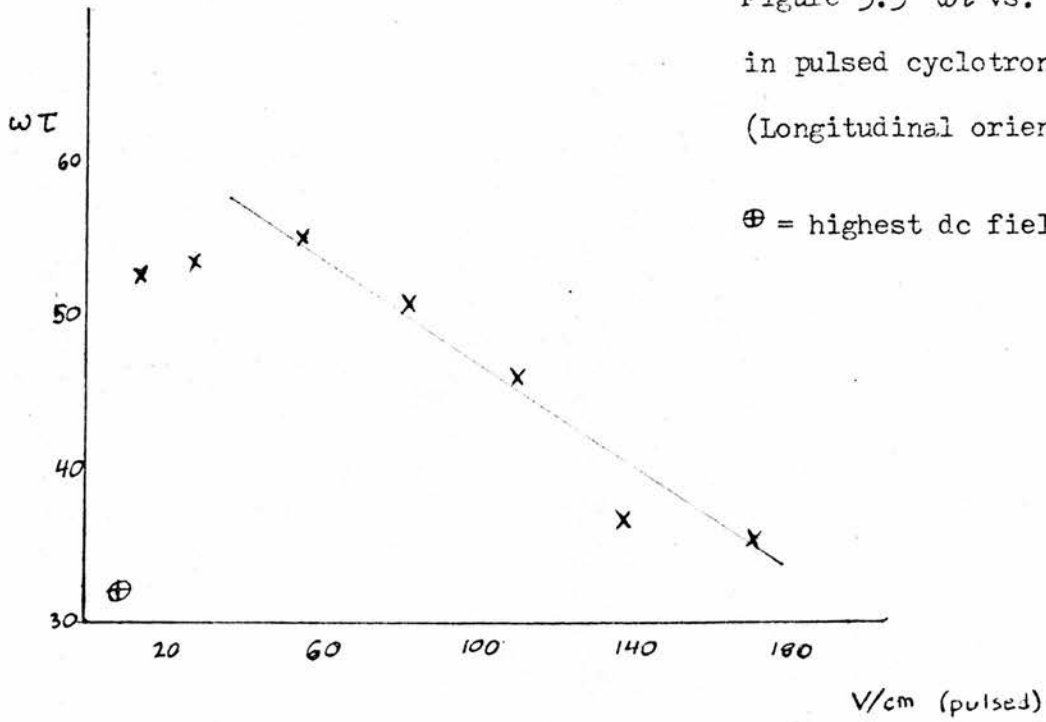


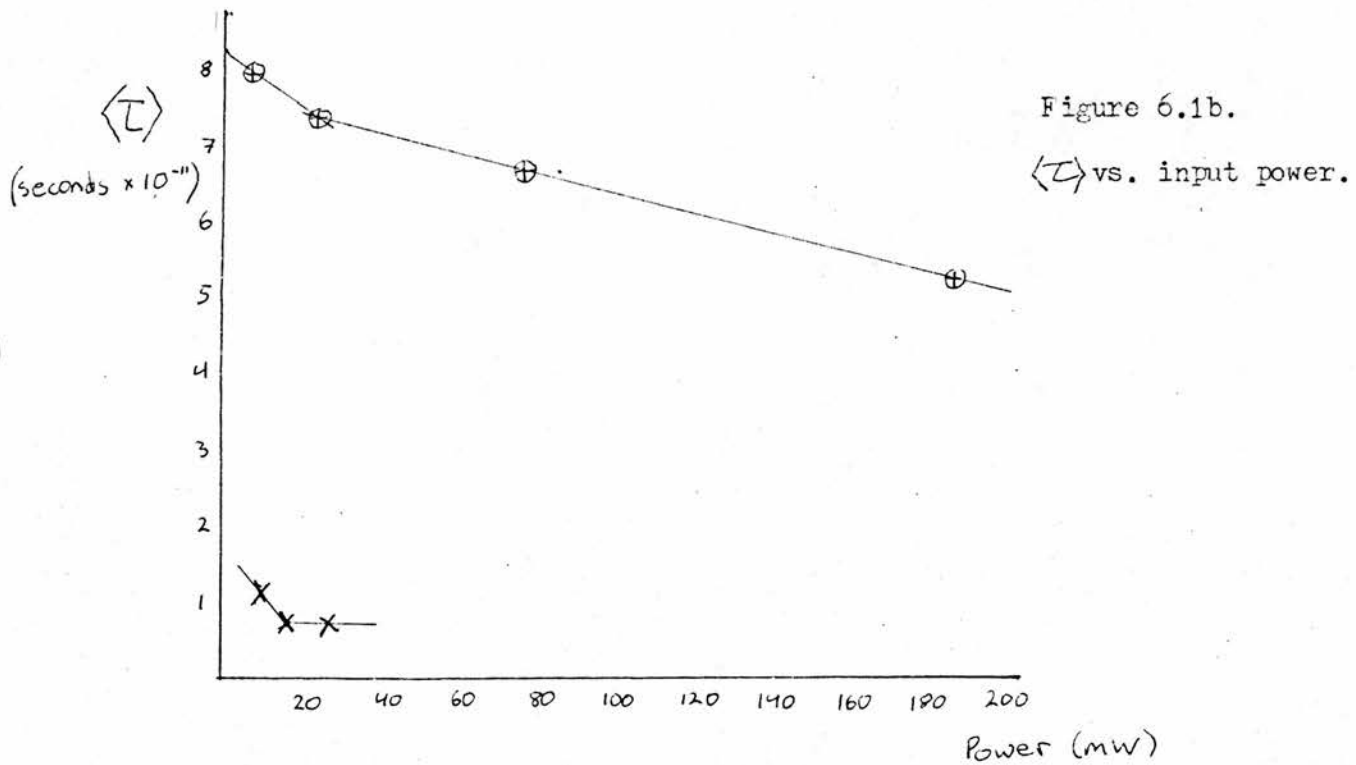
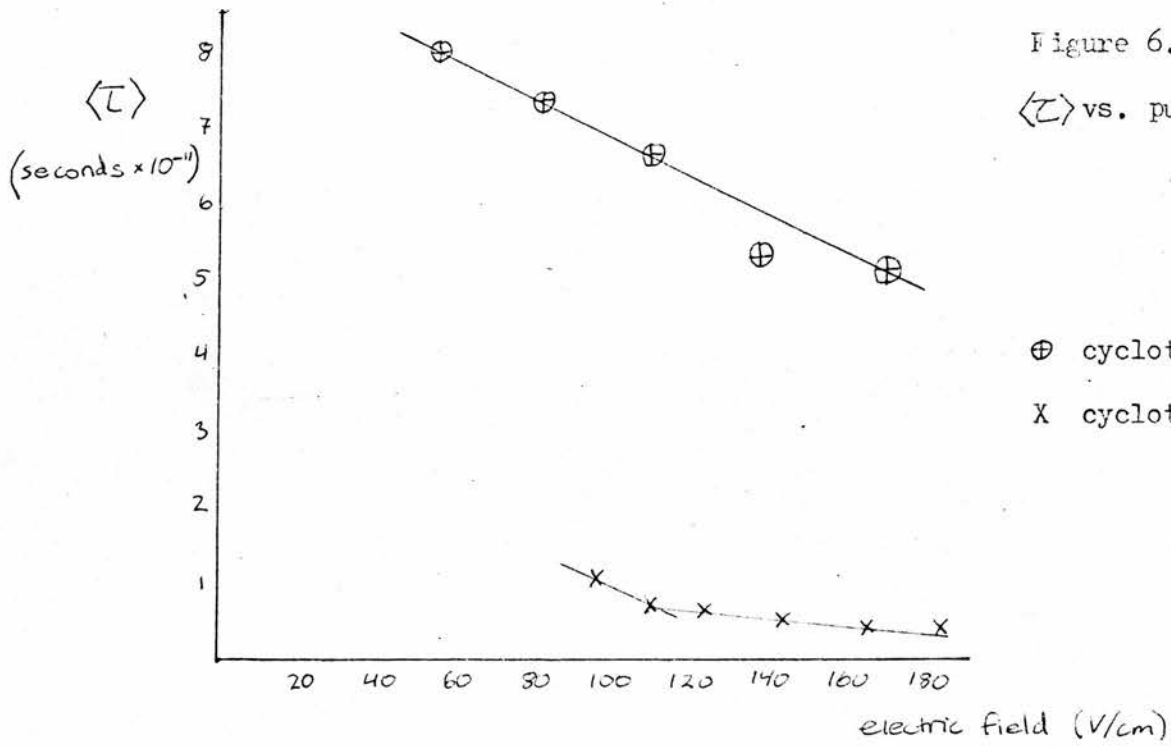
Figure 5.6 Signal intensity vs.  
electric field in pulsed cyclotron  
resonance.

## Section VI

### Comparison of linewidths in cyclotron emission and absorption

The values of  $\omega\langle\tau\rangle$  found in cyclotron resonance and in cyclotron emission are of the same order of magnitude, but this is just coincidental. To take account of the factor of nine difference in frequency (the resonance experiment was done at 110 GHz. and the emission experiment at  $34 \text{ cm}^{-1} = 1020 \text{ GHz.}$ ), just  $\langle\tau\rangle$  needs to be considered. In pulsed cyclotron resonance, the longest  $\langle\tau\rangle$  was found to be  $8 \times 10^{-11}$  seconds, increasing to about  $10^{-10}$  seconds at low dc fields. This is comparable to Bagguley, et. al. (24), who measured  $\langle\tau\rangle$  to be  $7 - 8 \times 10^{-11}$  seconds in microwave electric fields of up to 100 mV/cm.  $\langle\tau\rangle$  against electric field is plotted in figure 6.1a for both experiments. It can be seen that the emission linewidths are about a factor of eight broader than the absorption linewidths.

The effect of the high electric field on the linewidths may be estimated by calculating the electron temperature. As described earlier, the electrons will have a distribution of energy characterized by an electron temperature  $T_e$ . Part of the difference in linewidths between cyclotron resonance and cyclotron emission may arise from the experiments being sensitive to electrons in different parts of the distribution. Because the scattering time is a function of electron energy, it will be different in the two cases. In cyclotron emission, the contribution comes from high energy electrons, because the electrons must have a minimum energy of  $\hbar\omega_c$  to be in the first Landau level. This is equivalent to a temperature of  $49^\circ\text{K}$  at  $34 \text{ cm}^{-1}$ . In cyclotron resonance, however, the absorption could come from lower energy electrons, which would give a larger  $\langle\tau\rangle$ .



Scattering times for cyclotron resonance and cyclotron emission experiments.

An estimate of  $T_e$  can be made from considering the rate at which the electrons gain energy from the electric field. This is given by the force multiplied by the average velocity:

$$\frac{d\mathcal{E}}{dt} = eE \times \mu E$$

where  $\mathcal{E}$  is the electron energy,  $E$  is the electric field and  $\mu$  is the electron mobility. This can be approximated by the average energy divided by the energy relaxation time  $\tau_{\mathcal{E}}$ . If the electrons can be described by a Maxwellian distribution, then:

$$\mathcal{E}_{av} = 3/2 k(T_e - T).$$

So we can calculate  $T_e$  from:

$$e\mu E^2 = 3/2 k \frac{(T_e - T)}{\tau_{\mathcal{E}}}$$

$\tau_{\mathcal{E}}$  has been found to obey the relation:

$$\tau_{\mathcal{E}} = 3 \times 10^{-10} (100^\circ\text{K}/T)^{\frac{1}{2}} \text{ seconds} \quad (28)$$

which gives  $\tau_{\mathcal{E}} = 1.5 \times 10^{-9}$  seconds at  $4^\circ\text{K}$ . The mobility has been found by Koenig, et. al. (38), to be  $2 \times 10^6 \text{ cm}^2/\text{V-s}$  for a sample with a carrier concentration of  $10^{13} \text{ cm}^{-3}$ . We can extrapolate this to give a mobility of about  $3 \times 10^6 \text{ cm}^2/\text{V-s}$  for a sample with a concentration of  $2 \times 10^{12} \text{ cm}^{-3}$ . This is in agreement with the formula found by Bagguley, et. al., (24) for the electron mobility in the presence of phonon scattering:

$$\mu = 2.4 \times 10^7 T^{-1.5} \text{ cm}^2/\text{V-s}.$$

Using these values, we get  $T_e = 12^\circ\text{K}$  for an electric field of .5 V/cm. This increases rapidly with field, giving  $T_e = 36^\circ\text{K}$  at  $E = 1\text{V/cm}$  and  $T_e = 290^\circ\text{K}$  at  $E = 3 \text{ V/cm}$ .  $T_e$  will not increase this rapidly in practice because  $\mu$  will decrease. Koenig calculates  $T_e$  using  $\mu/\mu_0 \propto E^{-\frac{1}{2}}$  (and an effective mass tensor to account for the mass anisotropy). He calculates  $T_e = 20^\circ\text{K}$  for  $E = 3 \text{ V/cm}$  at  $T = 7^\circ\text{K}$  and  $T_e = 230^\circ\text{K}$  for  $E = 40 \text{ V/cm}$  and

$T = 8^{\circ}\text{K}$ . Experimentally, he found that  $T_e$  was higher ( $70^{\circ}\text{K}$  and  $380^{\circ}\text{K}$ , respectively).

In our experiments, the fields for electron heating were substantially higher because the experiments were done in a magnetic field. The magnetic field has a cooling effect on the electron temperature, which is proportional to  $B^2$  at low  $B$  (figure 6.2), (38). The effect of the magnetic cooling can be estimated from the difference in breakdown voltage for non-Ohmic behavior observed in the current-voltage characteristics described in section IV. In zero magnetic field, we found the breakdown voltage to be about 10 V/cm and at 3.6T, about 56 V/cm. From the above, we can estimate, very roughly, that the electron temperatures we are working with at the fields where we are comparing the linewidths (about 90 V/cm) are on the order of 10 -  $100^{\circ}\text{K}$ .

The two experiments were done at different magnetic fields (.3 T for cyclotron resonance and 3 T for cyclotron emission), and some account needs to be taken of this. In figure 6.1b,  $\langle v \rangle$  is plotted against the power put into the sample. The power here is calculated simply as the pulse voltage multiplied by the current found from the current-voltage characteristics described previously. This exaggerates the effect of the magnetic field, because the two current-voltage curves were taken at zero field and at 3.6 T, while the two experiments were done at .3T and 3T. Still, it gives some indication of the effect of magnetoresistance on the power being put into the sample. However, we cannot say with any certainty what effect the difference in magnetic fields is having on the electron temperature. As can be seen in figure 6.3 (18), the relationship between  $\xi_{av}$  and  $B$  is not a simple one. The cyclotron resonance experiment should be repeated at the same magnetic field as the emission experiment to be sure that the difference in magnetic field is not affecting the linewidths.

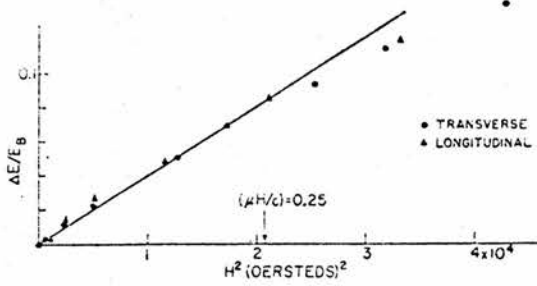


FIG. 21. Variation of the fractional change in breakdown field ( $\Delta E/E_B$ ) with both longitudinal and transverse magnetic field.

Figure 6.2.

Variation of breakdown voltage with magnetic field.

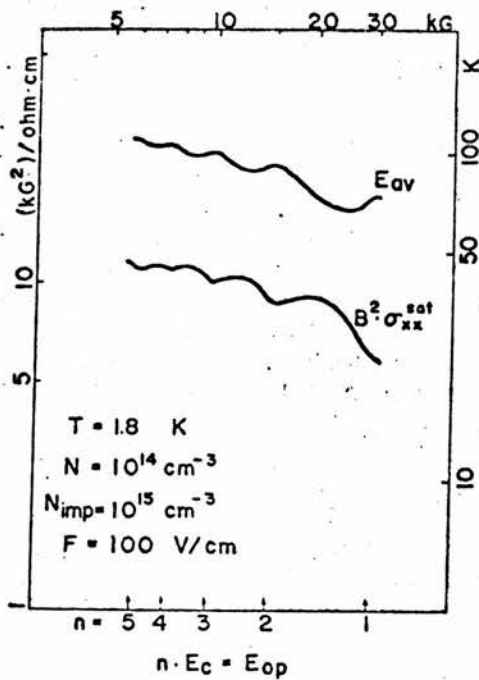


Fig. 4. Average energy  $E_{av}$  and transverse conductivity  $\sigma_{xx}$  multiplied by squared magnetic induction in the electric field of 100 V/cm as a function of magnetic field. Arrows show the points of magnetophonon resonance.

Figure 6.3.

(Top trace) Variation of average electron energy with magnetic field.

We can estimate the electron temperatures needed to give the observed linewidths using the theoretical value of  $\langle\tau\rangle$  given by Baguley, et. al., (24). They found the linewidth to be:

$$\frac{1}{\langle\tau\rangle_{cr}} = .1 \times 10^{11} + 4 \times 10^8 T^{3/2} \text{ sec}^{-1}.$$

The constant term is due to impurity scattering and the temperature dependent term to phonon scattering. At  $4.2^\circ\text{K}$ , the limiting linewidth in the absence of impurities gives an  $\omega\langle\tau\rangle$  at 110 GHz. of 200 and an  $\omega\langle\tau\rangle$  at 1020 GHz. of 1860. In the first case the measured  $\omega\langle\tau\rangle$  was 55, and in the second case about 70. To reduce  $\omega\langle\tau\rangle$  from 200 to 55 requires an electron temperature of  $54^\circ\text{K}$ , while to reduce  $\omega\langle\tau\rangle$  from 1860 to 70 requires a temperature of about  $3000^\circ\text{K}$ . From the previous paragraphs, it can be seen that temperatures on the order of  $54^\circ\text{K}$  are to be expected; therefore the broadening of the cyclotron resonance lines can be explained as the effect of the increased electron temperature. However, temperatures of  $3000^\circ\text{K}$  would not be expected. While the cyclotron emission broadening may be partly caused by the electron temperature, it must also be broadened by other effects.

Another factor which can explain the difference between the linewidths in the two experiments is the fact that the broadening due to non-parabolicity is proportional to frequency. Cusset, et. al., (39) have found that the broadening is .16% per meV at 890 GHz. This will give a broadening of .02% per meV at 110 GHz. and .18% per meV at 1021 GHz. To get an  $\omega\langle\tau\rangle$  of 70 at 1020 GHz., therefore, requires an energy of 8 meV, which is equivalent to  $92^\circ\text{K}$ . An  $\omega\langle\tau\rangle$  of 55 at 110 GHz., however, requires 91 meV, or over  $1000^\circ\text{K}$ . Temperatures of the order of  $90^\circ\text{K}$  are to be expected in cyclotron emission, so the emission linewidth can thus be explained as a broadening due to non-parabolicity. The non-parabolicity, however, is only expected to make a small contribution to the absorption linewidth.

### Summary

We have seen that the linewidths in cyclotron emission and cyclotron resonance differ by a factor of about eight, but by considering the different mechanisms contributing to the linewidths in each experiment, the difference in linewidths can be accounted for. The linewidth in cyclotron resonance may be satisfactorily explained by the theory of acoustic phonon scattering given an electron temperature of  $54^{\circ}\text{K}$ , and we have seen that this is a reasonable temperature to expect at the electric fields used in these experiments. The cyclotron emission linewidth can be explained by the broadening due to non-parabolicity at a temperature of  $92^{\circ}\text{K}$ . We have seen that this is also a reasonable temperature, and that we could expect the temperature in an emission experiment to be higher than in an absorption experiment. There will also be some contribution to the emission linewidth from the temperature broadening and, especially at the lower electric fields, from the detector linewidth.

## Section VII: Laser Annealing

### Introduction

Heavy doping of surface layers of semiconductors by bombarding the surface with a beam of impurity ions is now a widely used technique. While the method has proved successful for forming shallow junctions with a high degree of control over the impurity profile, ion implantation has the drawback that a large amount of damage is introduced into the surface region. The disorder caused by the energetic ions coming to rest in the crystal can make the surface layer amorphous, and the impurities are not electrically active as they are not in substitutional sites. The standard treatment for removing the implantation damage has been thermal annealing. By heating the whole sample (a typical treatment for silicon would be heating to 900°C for 30 minutes) only some of the damage is removed, often with the unwanted side effect of impairing the electrical properties of the substrate material, and with only incomplete activation of the dopants. In 1976 Soviet scientists reported a new annealing technique using laser radiation (1). Laser annealing has been widely investigated recently, and researchers claim that it gives complete removal of lattice damage, no degradation of substrate properties, and increased activation of impurities.

The method is simply to apply laser radiation to the implanted semiconductor surface, using either a pulsed or continuous wave (cw) laser of appropriate energy density and wavelength. If the wavelength is such that the radiation energy is greater than the band gap, then there is a large absorption of radiation into the first few thousand angstroms of the material, and the energy absorbed into the bulk of the crystal is small. The variation of absorption coefficient with wavelength for silicon is shown in figure 7.1 along with the wavelengths of various

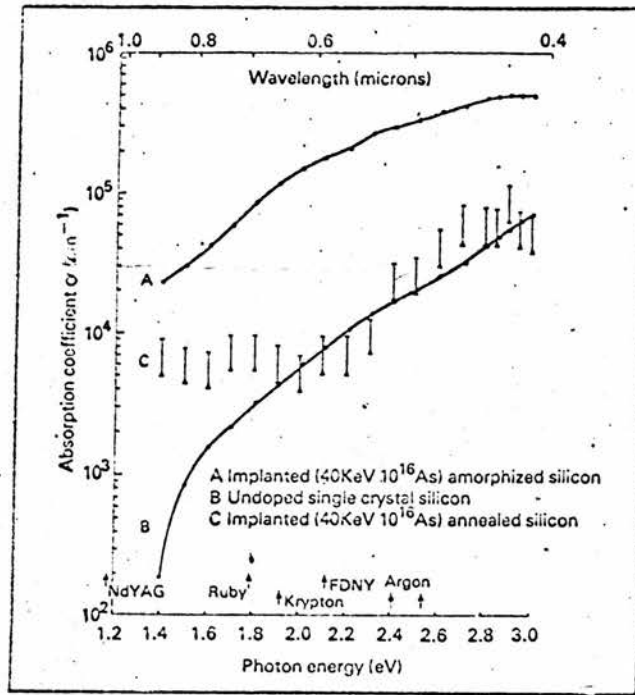


Figure 7.1

Optical absorption coefficients of silicon at room temperature

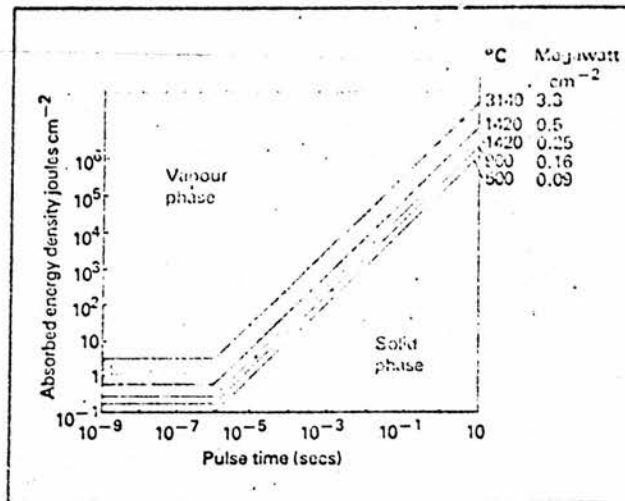


Figure 1 Phase map for laser annealing of silicon.

Figure 7.2

Relation of laser energy density with pulse length.

lasers used for annealing (2). If the absorption coefficient is greater than  $3 \times 10^4 \text{ cm}^{-1}$ , then 90% of the radiation is stopped in the first micron of material. The energy required for annealing depends strongly on how long the material is exposed to the beam. As the mechanism for annealing is quite different for pulsed and cw lasers, we can consider the two separately.

### Pulsed Laser Annealing

The relation between the laser energy density and the pulse length required for the heating of a silicon surface to a specific temperature is shown in figure 7.2 (3). It can be seen that there are two distinct regions. For pulses of less than one microsecond, the pulse time is less than the time needed for heat to diffuse out of the surface region. As all of the energy is then used to raise the surface temperature, only a small amount of energy is required. If the pulse length is longer, heat will diffuse out of the surface layer into the substrate, and so more energy is needed, and the substrate may be affected. For this reason, pulsed lasers are usually used in the Q-switched mode, giving a pulse length of 10-100 nanoseconds. In practice, it has been found that about  $1 \text{ Joule/cm}^{-2}$  is the minimum energy density required for annealing with this pulse length, though this will depend on the implantation conditions (4).

Transmission electron microscopy has shown that there is essentially no residual lattice damage after laser annealing, compared with numerous dislocation loops left after thermal annealing. The laser pulse does leave some surface structure in the form of ripples and craters, though these effects can be reduced by removing the coherence of the laser beam with a beam homogenizer. (5)

It is not generally agreed by what mechanism the annealing works, but the most widely held theory is that the laser radiation melts the crystal surface, and that this melted region then recrystallizes from the undamaged substrate by liquid phase epitaxial re-growth. The dopants diffuse much more rapidly in the liquid phase than in the solid; in silicon the liquid phase diffusion coefficient is seven orders of magnitude higher than the solid. The result is an undamaged crystal with significant redistribution of impurities.

After pulsed laser annealing, the impurity profile is considerably broadened. Figure 7.3 shows the change in the dopant profile of P-implanted silicon measured by secondary ion mass spectroscopy. (6) The distribution is almost uniform to a depth of about .2 microns, a result which is important for certain device applications. Calculations based on the theory that the laser radiation melts the crystal surface produce good agreement with the observed redistribution of impurities (figure 7.4). Further evidence to support this theory is the time-resolved reflectivity experiment performed by Auston, et. al., in 1978 (7). They found that the reflectivity of silicon during laser annealing changed abruptly to the value for liquid silicon, and held that value for a few hundred nanoseconds before changing back. This is shown in figure 7.5. However, other theories point to the highly non-equilibrium conditions present in the laser annealing process, which suggest that something more complicated than simple melting of the surface is taking place. Possibly the impurities could diffuse in the solid state, aided by interactions with vacancies and mobile defects, especially as under conditions of strong ionization of the implanted layer the energy needed for defect migration is reduced. (8-10)

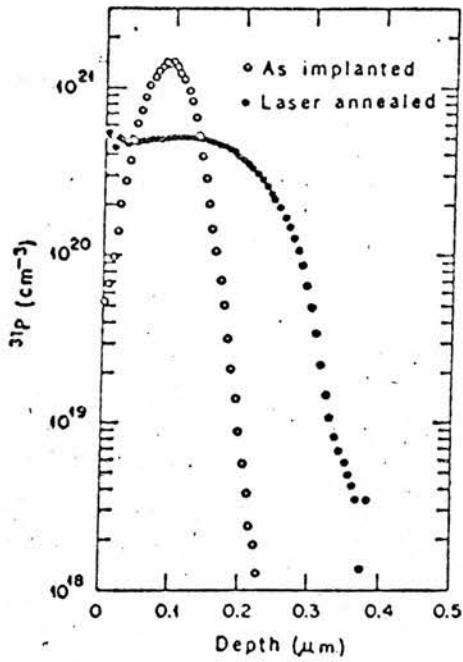


Figure 7.3

Dopant profile of P-implanted silicon.

$^{31}\text{P}(80 \text{ keV}, 1.16 \times 10^{16}/\text{cm}^2)$  in Si

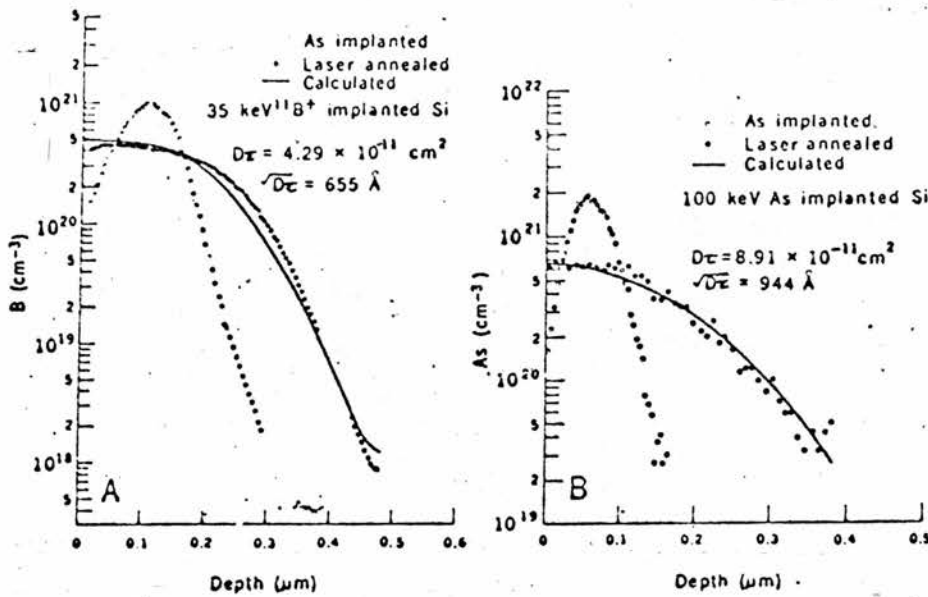


Figure 7.4 Comparison of experimental and theoretical dopant profiles.

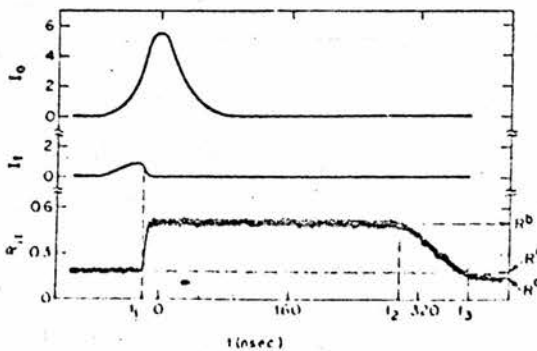


Figure 7.5

Reflectivity of silicon during laser annealing.

FIG. 1. Shown as a function of time are  $I_0$ , the incident laser intensity at  $1.06 \mu\text{m}$ ,  $I_t$ , the transmitted laser intensity (in arbitrary units), and  $R_0$ , which is the absolute value of the reflectivity at  $0.63 \mu\text{m}$  for light polarized parallel to the plane of incidence. The incident energy was  $5.2 \text{ J}/\text{cm}^2$  and the implant dose was  $10^{15}/\text{cm}^2$ .

The positions of the impurities in the lattice can be determined by ion-backscattering and ion-channeling techniques. In silicon, they have been found to be 98 to 99% incorporated into electrically active substitutional lattice sites, compared to 90% at best for thermal annealing. This means that the concentration of dopants far exceeds the equilibrium solid solubility limit. The explanation for this is that a high concentration of impurities are incorporated into substitutional sites during the liquid phase regrowth, and then the regrown region cools in only a few microseconds. This is too short a time for precipitation to occur at the solid phase diffusion rate, so the impurities are "frozen in" at a concentration exceeding the solid solubility limit. This supersaturated condition is stable up to 600°C in silicon, and leads to the possibility of manufacturing materials with properties unobtainable using thermal annealing.

#### CW Laser Annealing

If the laser annealing is done with a scanning CW laser, no redistribution of the dopants is observed (figure 7.6) (11). This indicates that annealing occurs in the solid phase, without any melting of the surface layer. The process may be solid phase epitaxial regrowth, or it has been suggested that annealing occurs throughout the damaged region simultaneously, with dopants and dislocated host atoms searching for vacant lattice sites to occupy. Either process takes place at the slow rate of about a millisecond, compared to hundreds of nanoseconds for liquid phase regrowth. As with pulsed laser annealing, essentially perfect recrystallization is observed, and with CW lasers the resulting surface is completely flat. The

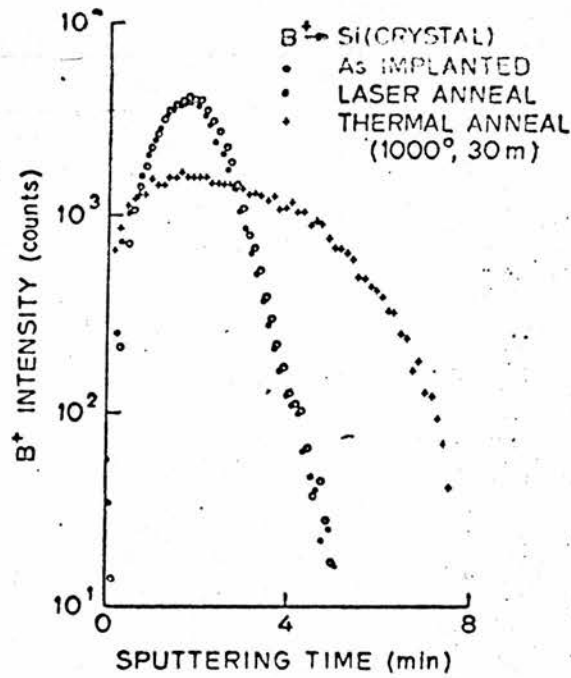


Fig. 9—Impurity profiles by the SIMS technique in as-implanted laser annealed and thermally annealed Si implanted with  $2 \times 10^{15}$  B<sup>+</sup>/cm<sup>2</sup> at 35 keV.

Figure 7.6 Dopant profile of B-implanted silicon after CW laser annealing.

concentration of impurity atoms which are electrically active can exceed the equilibrium (room temperature) solid solubility limit, because the sample has had time to come to equilibrium at a much higher temperature where the solubility limit is higher. This method of laser annealing is important for fine geometry devices, where one wants the carefully controlled impurity profile undisturbed. It also has interesting possibilities for using a laser scan to "write" regions of electrically active regrown crystal on an amorphous layer. (12)

#### Summary

Laser annealing promises to be a very important technique as it is quicker and more effective than thermal annealing. For example, laser annealing can be done in air because the cooling process is too quick for significant contaminants to be introduced, and compound semiconductors can be annealed without decomposition. To the highest experimental resolution, damage caused by ion implantation appears to be completely removed by laser annealing, and up to 99% of the implanted impurities are electrically active. Damage to the substrate is minimized, and the impurity profile can be smoothed out or left as implanted, depending on the type of laser used. For all these reasons, there are many promising applications of laser annealing in material development and processing.

## Section VIII: Experiments in Laser Annealing

### Sample Preparation

Laser annealing was first investigated here in St. Andrews on two 3"-diameter slices of ion-implanted silicon donated by Hughes Microelectronics of Glenrothes. The details of these slices are given in figure 8.1. The slices are assumed uniform enough that "before and after" comparisons can be done on different samples. The samples were cut by spark erosion, a wire saw, or by cleaving. The material is so brittle that the wire saw, while very slow, was the only method that did not tend to crack the large slices. Different methods were also tried to contact the samples. Neither silver conducting paint nor alloyed indium dots would stay on, so a device for applying four probes with adjustable pressure was constructed. The design of this is in figure 8.2. Silicon can be tested with probes but, as can be seen from descriptions of commercial devices, it is a very precise operation and such factors as the hardness of the probes and the pressure applied are critical. This rather rough device would not give an accurate reading on silicon, but it does work successfully on other materials such as germanium. Finally, aluminium was evaporated onto a masked sample and alloyed in at 500°C, and contacts were made to the aluminium with silver epoxy. While these contacts stayed on, the uncertain results of the electrical measurements undertaken indicate that the contacts are not reliable.

At first annealing was attempted here with a ruby laser belonging to Dr. Arthur Maitland, but the laser output proved to be too weak to anneal. Using a rat's nest calorimeter (figure 8.3),

Figure 8.1 Silicon samples used in laser annealing experiments.

Si - P implanted at 80 keV  $N \approx 10^{15} \text{ cm}^{-2}$

sample SiP6 unannealed

sample SiP2 annealed with  $1.92 \text{ J cm}^{-2}$

Si - B implanted at 35 keV  $N \approx 10^{15} \text{ cm}^{-2}$

sample SiB3 unannealed

sample SiB2 annealed with  $1.49 \text{ J cm}^{-2}$

sample SiU3 unimplanted silicon

Figure 8.2 Probe device for making 4-contact electrical measurements.

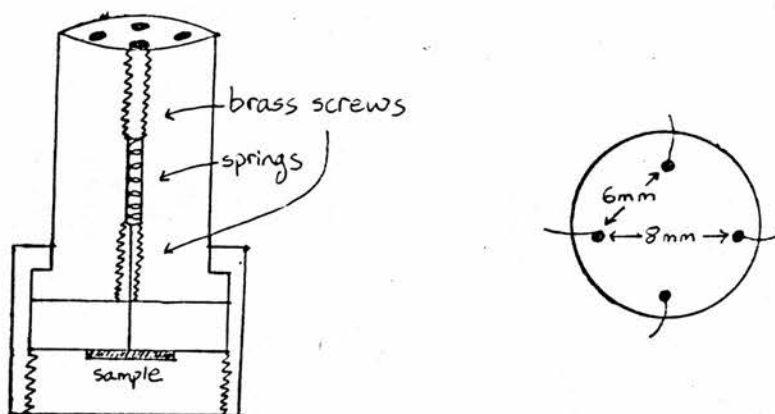
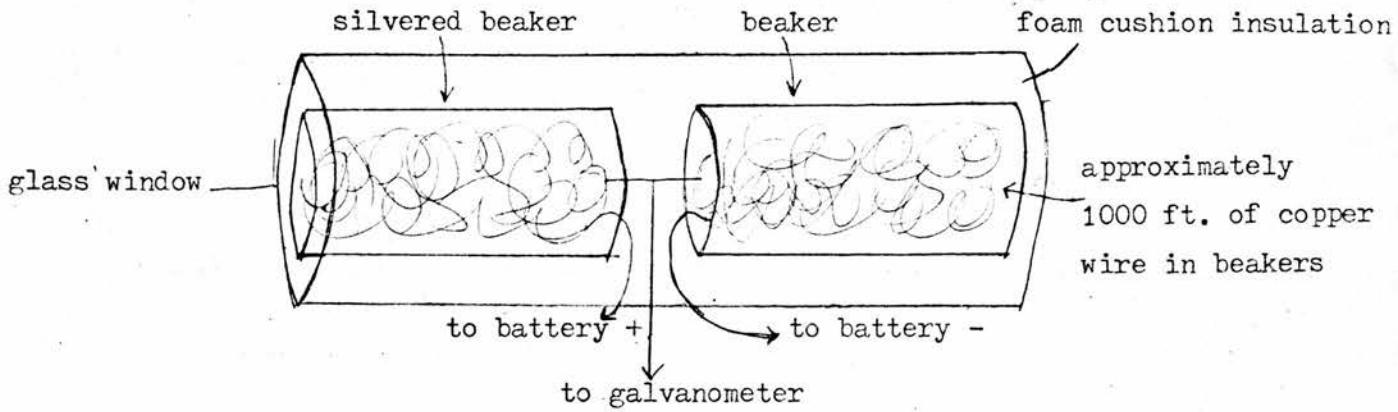
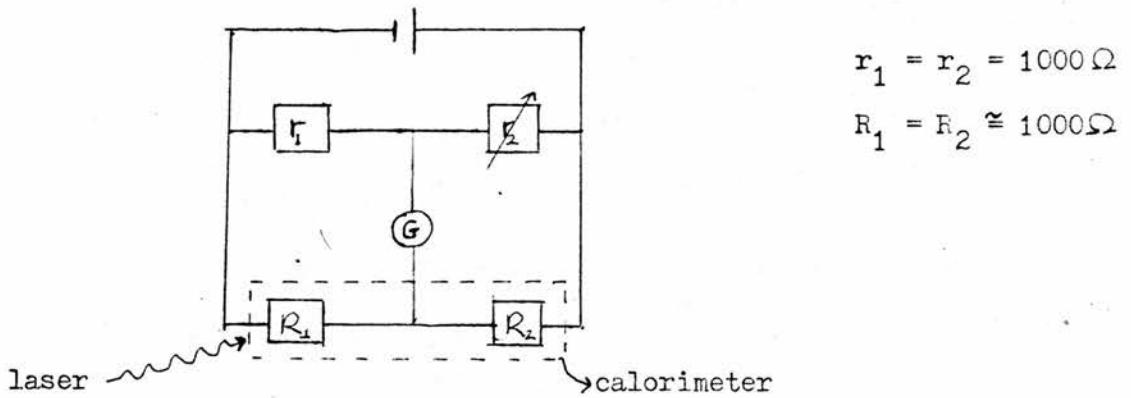


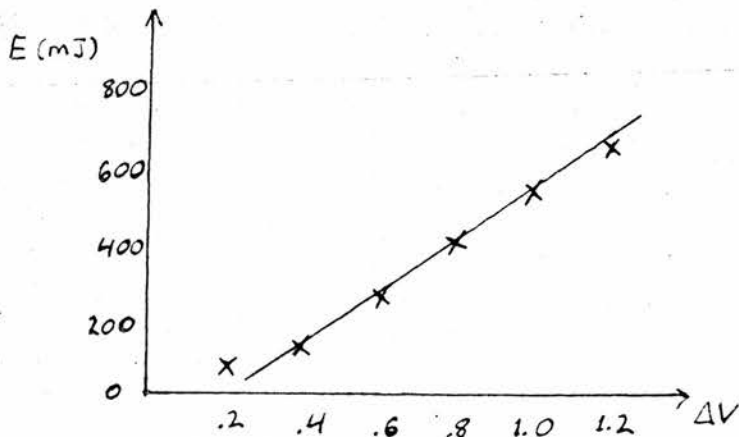
Figure 8.3 "Rat's nest" calorimeter.



The calorimeter is used as two arms of a Wheatstone bridge:



The calorimeter was calibrated using a He - Ne laser by measuring the voltage against time and comparing with the power given for the laser.



Calibration of rat's nest calorimeter.

Laser energy vs. change in voltage.

The average pulse for the ruby laser was found to be 550 mJ.

the energy output was measured to be .5 Joules, which is well below the critical threshold of 1 Joule. Several samples were annealed at RSRE Malvern with a q-switched Ruby laser with pulses of between  $1\frac{1}{2}$  - 2 J (the annealing details are included in figure 8.1). A definite change in reflectivity can be seen in these samples. Another problem with the laser here is that the output is multi-mode, causing a non-uniform intensity distribution in the beam and uneven annealing. At Malvern, this problem has been alleviated by the use of a quartz light guide diffuser. (5)

### Optical Experiments

The first experiment was to look at the transmission spectra of annealed and unannealed samples. Interferograms were taken on a Beckman Fourier Transform Spectrometer at room temperature, using a Golay detector to observe the transmission. The spectrometer, used with a 25 gauge beam splitter, covers the far infrared range from 25 microns to 1 mm. The experimental set-up is in figure 8.4. The spectra were calculated from the interferograms and plotted using the existing Fourier Transform computer program. Strong interference fringes were seen corresponding to the sample thickness, but no other structure. We could measure a change in the interference fringe spacing between annealed and unannealed samples, indicating a change in optical thickness  $nd$ . This can be seen from the relation:

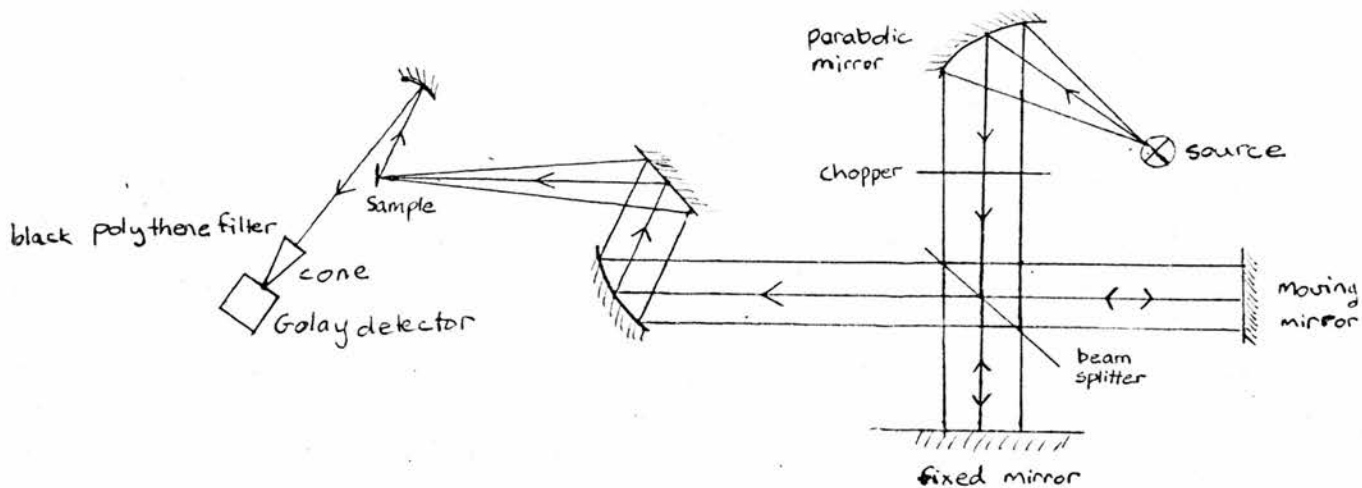
$$m\lambda = 2nd$$

$$\frac{1}{\Delta\nu} \propto nd$$

$$-\frac{\delta(\Delta\nu)}{\Delta\nu} \propto \frac{\delta(nd)}{nd}$$

where  $\Delta\nu$  is the fringe spacing in wavenumbers,  $d$  is the sample thickness, and  $n$  the refractive index. Careful

Figure 8.4 Fourier Transform Spectrometer. The spectrometer is shown set up for reflectivity measurements.



The source is a mercury vapor lamp in a quartz envelope, which behaves as a black body source. A Moire fringe system senses the mirror position. The signal and the Moire fringe count are fed into an analog-to-digital converter. The digital form of the results are punched onto paper tape, which is then read into the computer to be analyzed.

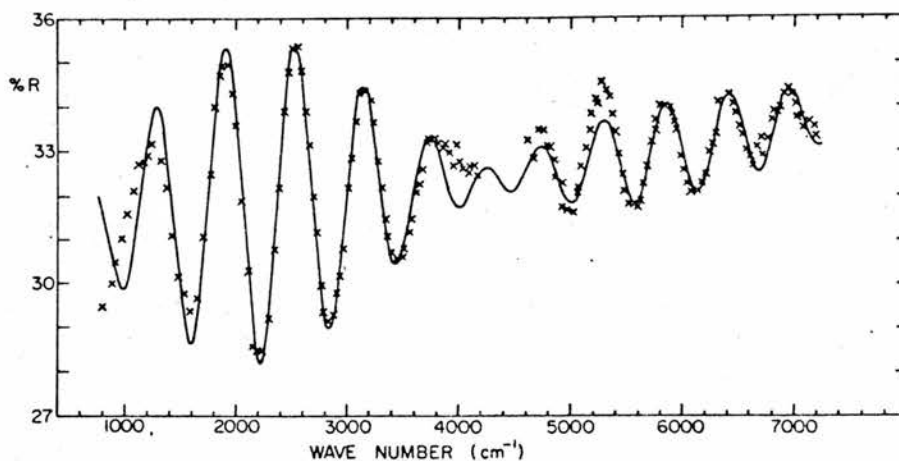


Figure 8.13. Calculated (solid curve) and measured reflectivity of ion-implanted GaAs.

measurement with a micrometer showed no change in the sample thickness, implying a change in the refractive index. This occurs due to the disorder which is introduced by implantation and then removed by annealing. The change in  $n$  for P-implanted Si was 1%.

As well as taking experimental transmission spectra, computer calculations were made using parameters expected of the samples studied. The effect of the substrate is ignored, and the calculation is done for a single conducting layer in a vacuum. The program was later expanded to calculate reflection and absorption, to plot the results on graphs, and to do the calculations for multi-layer systems. Thanks are given to A. M. Davidson for help with these alterations. The basic calculation is as follows: (20)

The complex dielectric function  $\epsilon$  is defined:

$$\epsilon = \epsilon_L \left( 1 - \frac{\omega_p^2}{\omega^2 - i\omega/\tau} \right) = \epsilon_R + i\epsilon_I$$

where  $\omega_p$  is the plasma frequency:

$$\omega_p^2 = \frac{Ne^2}{m^* \epsilon_0 \epsilon_L}$$

$\epsilon_L$  is the lattice dielectric constant,  $N$  is the carrier concentration,  $m^*$  is the (optical) effective mass, and  $\tau$  is the scattering time, related to the mobility  $\mu$  by:

$$\mu = e\tau/m^*$$

The complex refractive index  $\tilde{n}$  is related to  $\epsilon$  by:

$$\tilde{n}^2 = (n + ik)^2 = \epsilon.$$

The transmission intensity is given by:

$$\frac{I_T}{I_0} = \left| \frac{A_T}{A_0} \right|^2.$$

$\frac{A_T}{A_0}$  is the sum of a geometric series. For a one layer system:

$$\frac{A_T}{A_0} = \frac{T_{12} T_{23} e^{i\phi_2}}{1 + R_{12} R_{23} e^{2i\phi_2}}$$

$T_{12}$  = transmission coefficient for medium 1 (vacuum) to medium 2 (sample)

$T_{23}$  = transmission coefficient for medium 2 (sample) to medium 3 (vacuum)

Similarly,

$R_{12}$  = reflection coefficient for medium 1 to medium 2

$R_{23}$  = reflection coefficient for medium 2 to medium 3

The coefficients are defined:

$$T_{ab} = \frac{2\tilde{n}_a}{\tilde{n}_a + \tilde{n}_b} \quad R_{ab} = \frac{\tilde{n}_a - \tilde{n}_b}{\tilde{n}_a + \tilde{n}_b}.$$

For  $\tilde{n}_1 = \tilde{n}_3 = 1$  (for a vacuum) and  $\tilde{n}_2 = \tilde{n}$ :

$$T_{12} = \frac{2}{1 + \tilde{n}} \quad T_{23} = \frac{2\tilde{n}}{1 + \tilde{n}} \quad R_{12} = -R_{23} = \frac{\tilde{n}-1}{\tilde{n}+1}.$$

The phase factor in the exponential term is:

$$\phi = \frac{\omega d}{c} \tilde{n}.$$

The reflection can be similarly calculated from:

$$\frac{I_R}{I_0} = \left| \frac{A_R}{A_0} \right|^2$$
$$\frac{A_R}{A_0} = \frac{R_{12} + R_{23} e^{2i\phi/2}}{1 + R_{12} R_{23} e^{2i\phi/2}}$$

The absorption is given by:

$$1 - \frac{I_R}{I_0} - \frac{I_T}{I_0}.$$

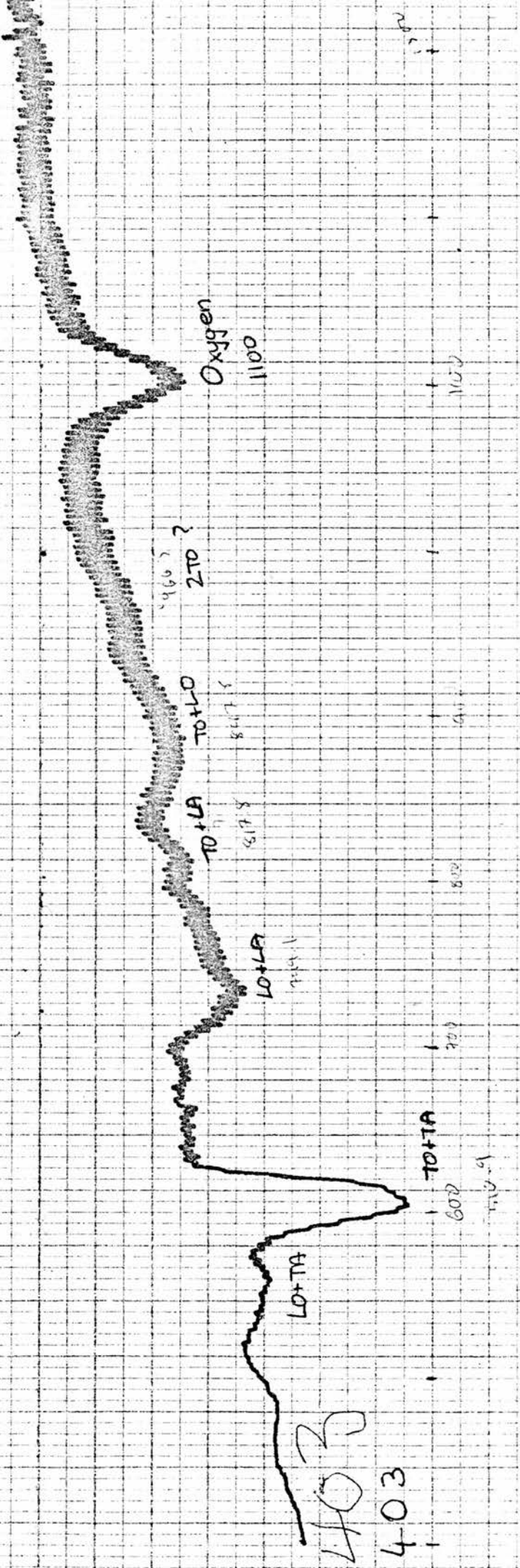
It is apparent from the spectra produced by these calculations that any structure which could be used to characterize the samples would be near the plasma frequency in the near infrared region, out of the range of the spectrometer. The program remains a very useful one, however, for calculating spectra in many different situations. Such factors as the cyclotron frequency in a magnetic field and phonon frequencies may be easily added to the expression for the dielectric

function. Kachare, et. al., has used a similar calculation to describe interference fringes in ion-implanted GaAs (21). He found that a model using two partially absorbing layers on a non-absorbing substrate gave very good agreement with experiment. (figure 8.13)

Spectra were also taken at Oxford using a double beam interferometer which covers the spectral range 400 to 10,000  $\text{cm}^{-1}$ . Various phonon combination lines can be identified, but nothing which can be used to characterize the samples. An example of these spectra is in figure 8.5.

### Transport Experiments

It was then attempted to characterize the samples by means of resistivity and Hall effect measurements. Sheet resistance was measured by the van der Pauw method of four contacts on the perimeter of an arbitrarily shaped sample (figure 8.6) (18). Resistivity was then calculated assuming a layer thickness of either  $1\mu\text{m}$  or  $.1\mu\text{m}$ . Hall effect measurements were done at  $77^{\circ}\text{K}$  in an electromagnet at fields up to 1 Tesla. The results calculated from these experiments are extremely unlikely (figure 8.7). A possible explanation is the effect of the contacts. For one thing, they are not very "good" contacts in the sense that it is not always possible to take steady, reproducible readings with all of them. For another, they are quite large, which introduces large errors into the van der Pauw calculation. Also, the effect of the conducting substrate, and whether it can be ignored, is unknown. It is possible that the resistivity of the heavily doped, disordered layer is too high to make Ohmic contacts to it by this method (13). Some work has been done on using the technique of laser annealing to overcome these difficulties in making contacts to semiconductors (14).



Phonon combination lines

Phonon combination	Energy (meV)	Energy ( $\text{cm}^{-1}$ )
3TO	179.4	1449.7
2TO + LO	170.9	1381.0
2TO + LO	162.4	1312.3
2TO + LA	161.0	1301.0
2TO	119.6	996.5
TO + LO	111.1	897.8
TO + LA	101.2	817.8
LO + LA	92.7	749.1
TO + TA	75.6	610.9
LO + TA	67.1	542.2
TO - TA	44.0	355.6

Figure 8.5

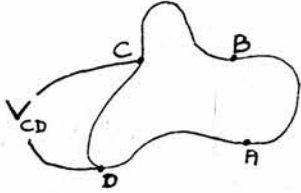
Silicon reflectivity spectrum.

Laser annealed, boron implanted silicon with KBr background.

Figure 8.6 van der Pauw's theorem.

$R_{CD}$  = voltage across C and D per unit current through A and B.

$R_{AD}$  = voltage across A and D per unit current through B and C.

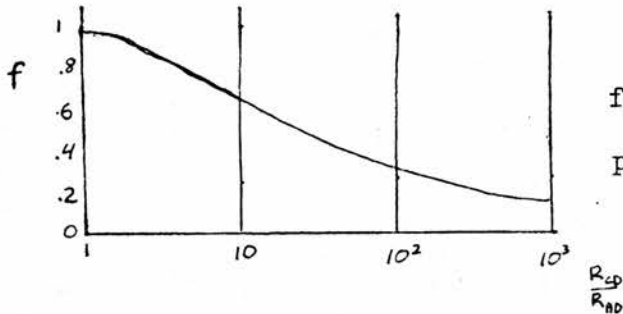


$d$  = sample thickness

$$R_s = \rho/d$$

$$\text{resistivity } \rho = \frac{rd}{\ln 2} \frac{(R_{CD} + R_{AD})}{2} f\left(\frac{R_{CD}}{R_{AD}}\right)$$

$$f \text{ satisfies: } \frac{R_{CD} - R_{AD}}{R_{CD} + R_{AD}} = f \operatorname{arcosh} \left( \exp\left(\frac{\ln 2/f}{2}\right) \right)$$



$f \rightarrow 1$  if contacts are symmetrically placed.

Conditions:

- contacts are at the circumference of the sample
- contacts are small
- sample is homogeneous in thickness
- sample is singly connected, i.e. no holes.

$$\text{Hall mobility } \mu_H = \frac{d}{B} \frac{\Delta R_{AC}}{\rho} \quad \Delta R_{AC} = \text{change in } R_{AC} \text{ with and without } B$$

There is least error in this method if a clover leaf-shaped sample is used.

Figure 8.7 Resistivity and Hall effect measurements on laser annealed silicon.

Sample	$R_s (300^\circ K)$	$R_s (77^\circ K)$	$d^* (\mu)$	$\rho (\Omega\text{-m})$	$R_H (m^3 C^{-1})$	$N (m^{-3})$	$\mu_H (m^2 V^{-1} s^{-1})$
SiP6	65.7	12.9	1	$1.3 \times 10^{-5}$	$1.4 \times 10^{-5}$	$4.4 \times 10^{23}$	1.1
			0.1	$1.3 \times 10^{-6}$	$1.4 \times 10^{-6}$	$4.4 \times 10^{24}$	1.1
SiP2	41.5	10.6	1	$1.1 \times 10^{-5}$	$8.2 \times 10^{-6}$	$7.6 \times 10^{23}$	0.8
			0.1	$1.1 \times 10^{-6}$	$8.2 \times 10^{-7}$	$7.6 \times 10^{24}$	0.8
SiB3	86.6	108.9	1	$1.1 \times 10^{-4}$	$1.4 \times 10^{-6}$	$4.4 \times 10^{24}$	0.013
			0.1	$1.1 \times 10^{-5}$	$1.4 \times 10^{-7}$	$4.4 \times 10^{25}$	0.013
SiB2	67.1	13.9	1	$1.4 \times 10^{-5}$	$1.6 \times 10^{-5}$	$4 \times 10^{23}$	1.1
			0.1	$1.4 \times 10^{-6}$	$1.6 \times 10^{-6}$	$4 \times 10^{24}$	1.1
SiU3	16.2						

82

$I = .96 \text{ mA}$        $T = 77^\circ K$  for Hall measurements       $R_H = \frac{d}{I} \left( \frac{\Delta V}{B} \right)$

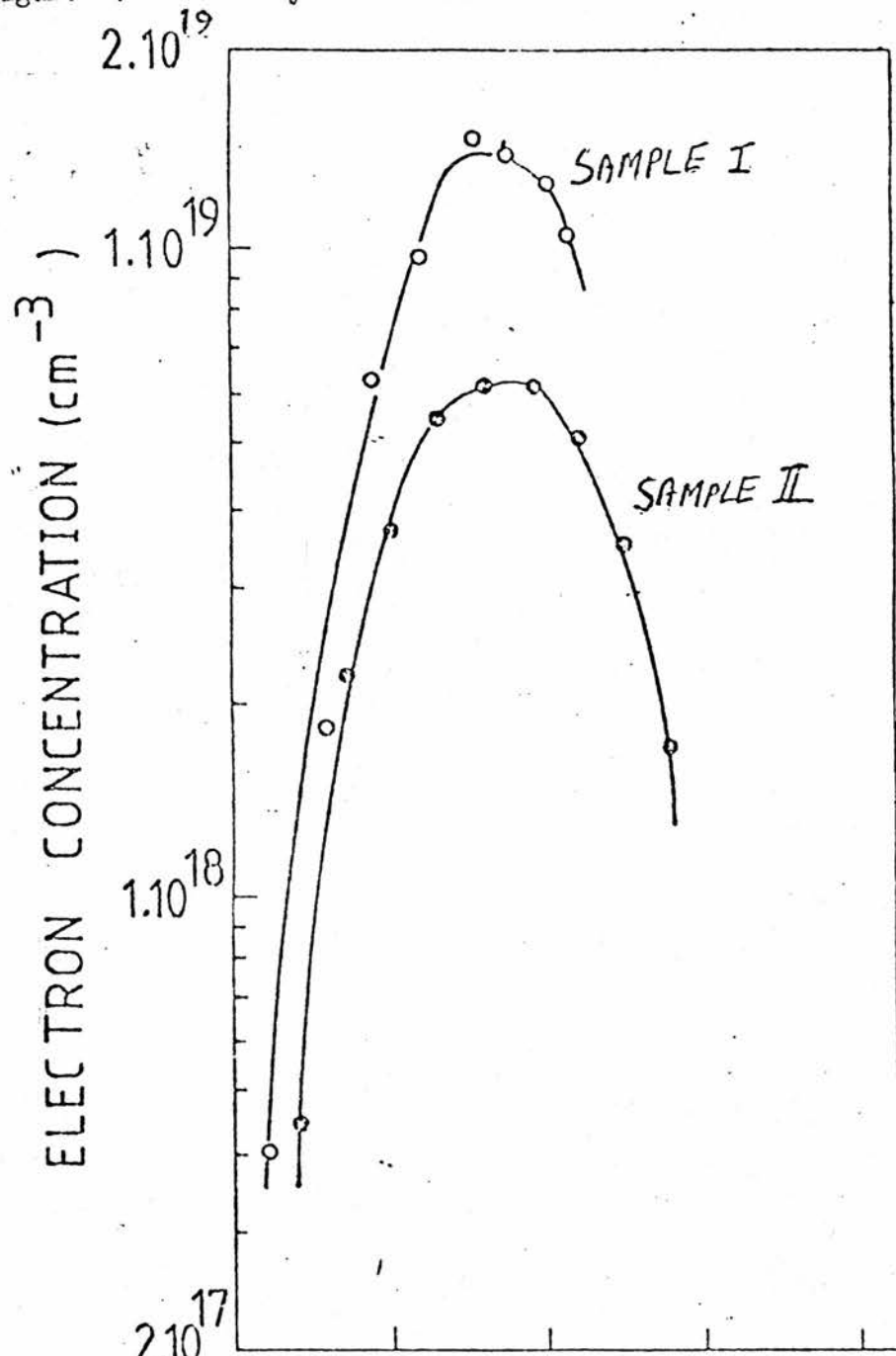
\* results were calculated for two different estimates of the sample thickness.

For an implant of  $10^{15} \text{ cm}^{-2}$ , one would expect  $N$  to be higher and  $\mu$  to be lower by factors of 10 or more.

## Experiments on GaAs

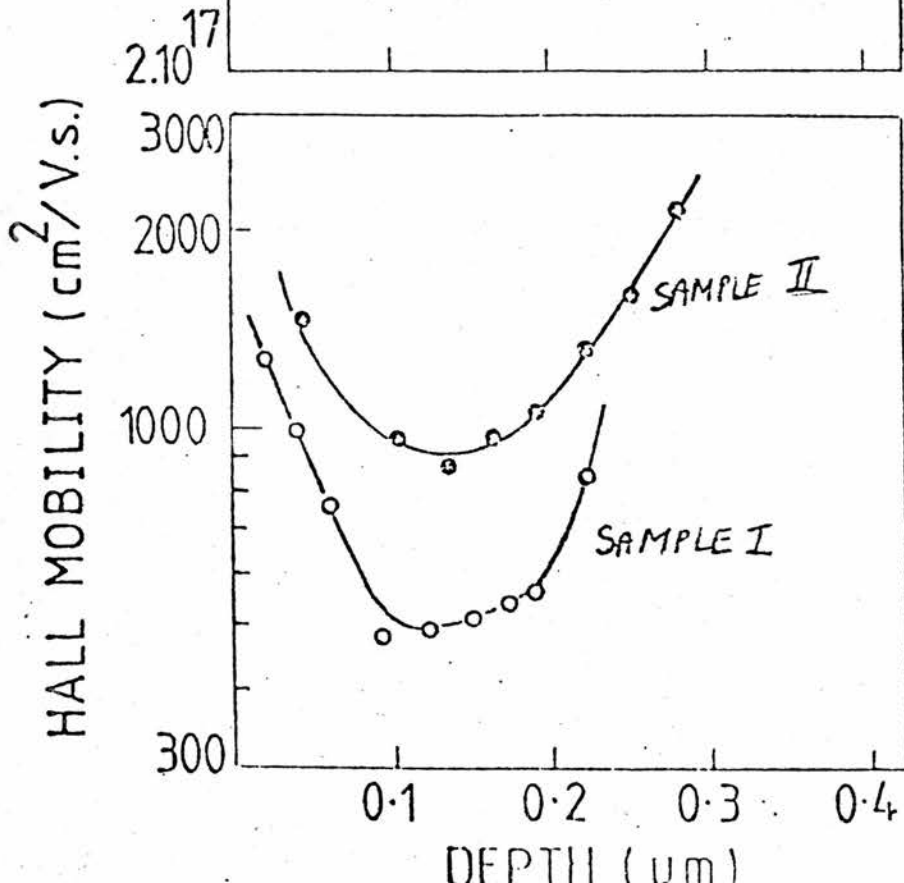
We have also done some experiments on ion-implanted, laser annealed GaAs samples donated by Dr. B. Sealey of Surrey University. The first samples investigated were implanted with  $\text{Se}^+$  ions at an energy of 300 keV and annealed with an energy density of  $.5 \text{ J/cm}^2$ . One sample had a subsequent thermal annealing treatment. Sheet resistance and Hall effect experiments done at Surrey in conjunction with chemical etching gave the electron concentration and mobility curves shown in figure 8.8. These gave a lower mobility than would be expected, though it is noteworthy that the thermal annealing increased the mobility. Further experiments done to test the mobility were inconclusive. We could see no cyclotron resonance in either sample. Dr. R. Nicholas of Oxford has calculated values of the Fermi energy  $\mathcal{E}_F$  for these samples. His values are supported by luminescence spectra taken at Oxford (figure 8.9) where the broad "above band" luminescence cuts off at the calculated value of  $\mathcal{E}_F + \mathcal{E}_G$ . This leads to values of  $B_F$ , the magnetic field for the first Shubnikov-de Haas oscillation, of about 100 T. This would indicate that at a field of 30 T the  $n = 3$  Shubnikov-de Haas oscillation should be seen. However, Professor J. C. Portal of Toulouse University did not see any convincing oscillations using a pulsed magnet with fields up to 30 T. These results indicate that either the implantation or annealing techniques used are not adequate to produce high concentration, high mobility samples.

Dr. Sealey has recently provided more samples which have been implanted at 800 keV and laser annealed at the same energy density as the earlier samples. A room temperature reflectivity spectra of one of these samples is shown in figure 8.10. A peak appears at

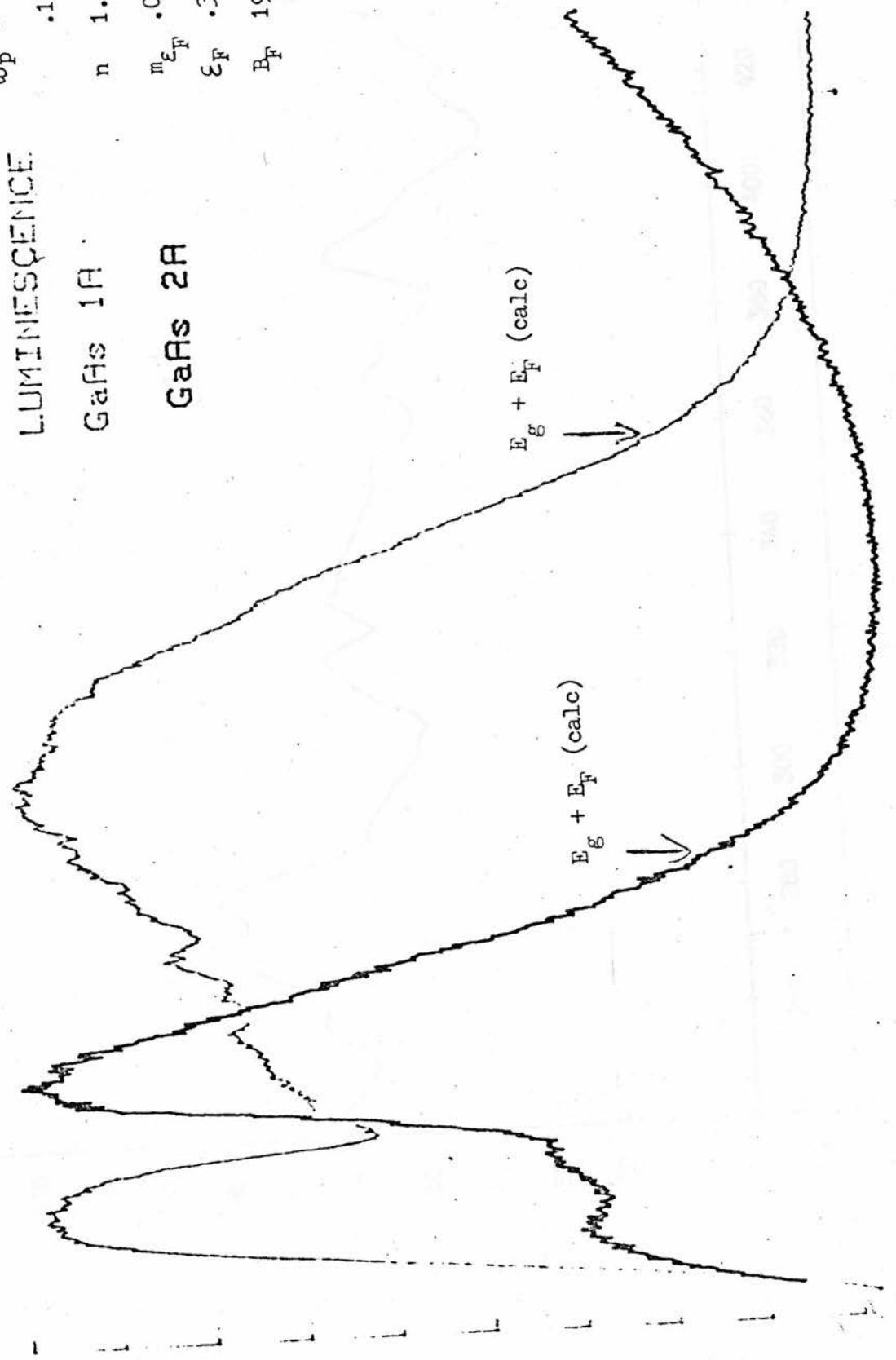


Sample I.  
 GaAs -  $\text{Se}^+$  at 300 K  
 $N = 10^{15} \text{ cm}^{-3}$   
 Annealed with laser  
 pulse of  $.5 \text{ J cm}^{-2}$ .

Sample II.  
 Same as sample I with  
 addition of thermal  
 anneal at  $900^\circ\text{C}$  for  
 30 minutes.



GaAs 1A 80K 5145A



LUMINESCENCE

GaAs 1A

GaAs 2A

$E_g + E_F$  (calc)

$E_g + E_F$  (calc)

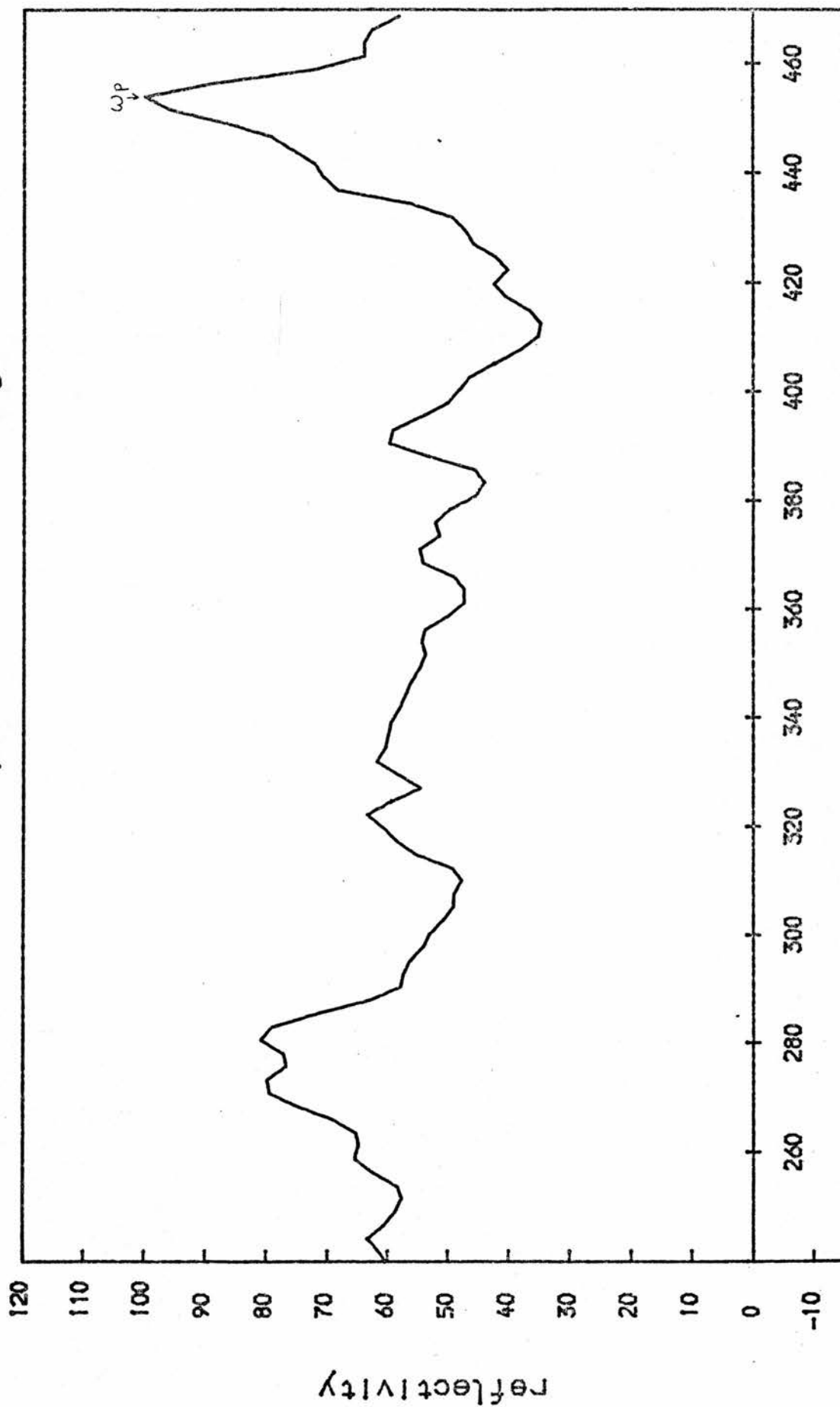
1.9000 eV

Calculated values:

	GaAs1a	GaAs2a
$\omega_p$	1274 $\text{cm}^{-1}$	742 $\text{cm}^{-1}$
$n$	$1.5 \times 10^{19} \text{ cm}^{-3}$	$6 \times 10^{18}$
$m_{e_F}$	.063 $m_0$	.074 $m_0$
$\xi_F$	.35 eV	.16 eV
$B_F$	190.5 T	102.3 T

Assume  $E_g \approx 1.45 \text{ eV}$   
 (tends to be reduced by heavy doping.)

reflectivity of laser annealed GaAs



frequency (cm-1)

Figure 8.10. Ratio of GaAs reflectivity against background with diamond Golay detector.

$450 \text{ cm}^{-1}$  which is believed to correspond to the plasma frequency, giving a carrier concentration of  $1.9 \times 10^{18} \text{ cm}^{-3}$ . The implantation is given as  $10^{15} \text{ cm}^{-2}$ , which therefore gives the carrier depth as  $.5 \mu\text{m}$  if we assume 10% of the implants are electrically active. (Sealey has found the electrical activity to range from 5 to 30%) (19)

Also, the optical phonon lines from the bulk material can be seen, though they are somewhat reduced in amplitude. This may be due to screening effects of the high electron concentration. This spectra is not as good as it might be because the beam splitter minimum is in the region of  $\omega_p$  and because the sample was too small to reflect the entire beam. This experiment should be done again with another beam splitter, and with a larger piece of material if possible.

## Thermal Annealing of GaAs

Another project involving annealing processes aims to settle an unresolved question concerning the central-cell effect in GaAs. As mentioned earlier, the impurity transitions in semiconductors are fairly well explained using a hydrogenic model of impurities. When the donor electron is close to the impurity atom, however, there will be small shifts in the electron transition energies corresponding to different impurities. The result is that instead of a single transition from the ground state to an excited state, several lines will be present corresponding to several different impurities. This only affects transitions involving the ground state, as this is the only state in which the electron has a probability of being near the impurity atom.

Several of these impurities in GaAs have been identified by comparing the photoconductivity spectra with those of back-doped samples (15). One line which has not been identified (labelled "b" in figure 8.11) is seen to appear in spectra of samples grown by vapor phase epitaxy (vpe) but not in those grown by liquid phase epitaxy (lpe). This line is believed to be due to gallium vacancies. We aimed to establish this by introducing vacancies into a lpe sample with a heat treatment and seeing if the required line appeared in the spectrum.

The heat treatment followed the suggestion of Hester, et. al. (16). The sample was heated to 600°C for 24 hours in an evacuated quartz tube. At the end of 24 hours, the sample was cooled to room temperature under vacuum in about ten minutes. The spectra of the sample taken before and after the treatment

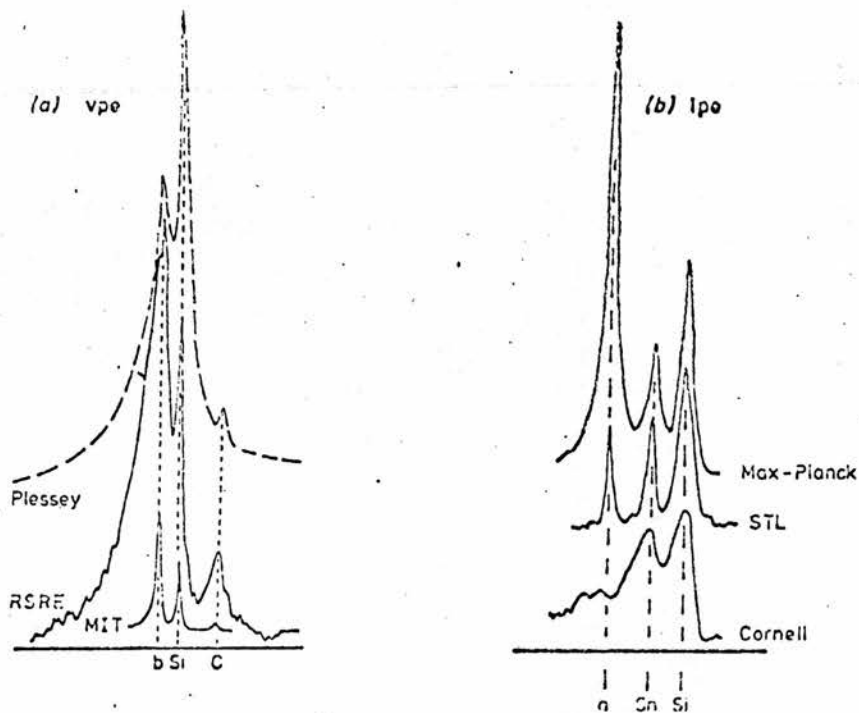


Figure 4 demonstrates that high-purity samples grown without specific doping contain the same set of residual contaminants even when they are prepared in different laboratories provided that the same growth technique is employed. Figure 4(a) compares the central cell structure observed on the 1s-2p- line in a field of 5 T for vapour phase material grown at Plessey, RSRE (Malvern) and MIT Lincoln Laboratory. All three samples contain impurities b, e and h. The lowest recording is taken from the paper by Stillman *et al* (1976). Figure 4(b) compares the central cell structure resolved on the 1s-2p- line for a field of 1.9 T with liquid phase samples prepared at the Max-Planck Institute in Stuttgart, STL (Harlow) and at Cornell University. All these liquid phase samples contain impurities a, d and e.

Figure 8.11

Central cell structure in photoconductivity in GaAs. The line labelled 'b' is believed to be due to gallium vacancies.

are in figure 8.12. It does look like a new line appears in the spectrum in the expected place, but it is not clearly seen due to the large tin line present in this sample which is near the expected position of the "b" line. The experiment needs to be repeated in a purer GaAs sample. Unfortunately when this was attempted on the only other available sample, no spectra could be taken after the heat treatment because of thermal damage to the sample. A stricter cleaning procedure needs to be followed in future attempts. It has also been found that the type of quartz tube used (spectrosil or vitrosil) is very important. (17)

photoconductivity of thermal annealed gaas

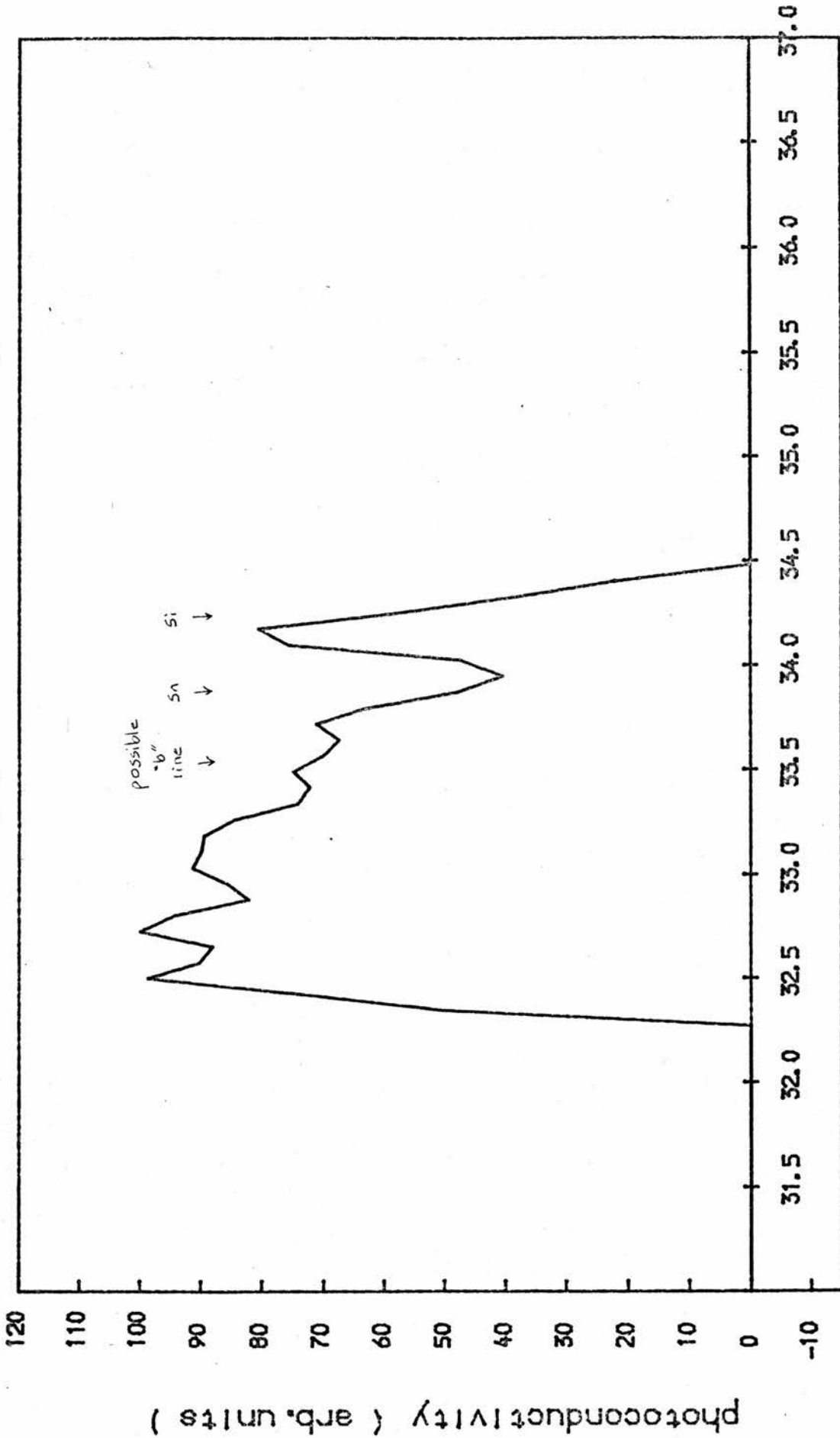


Figure 8.12 Ratio of spectra of thermally annealed sample against unannealed sample (figure 4.9).

## Section IX: Conclusion

The major part of this project has been concerned with studying the effect of the electric field in cyclotron emission, and particularly the effect of the electric field on the linewidth. Results were taken mainly on germanium, but also on some III-V compounds. Over most of the range of electric fields looked at, we have found that the linewidths broaden gradually, and that the intensity increases rapidly with field. In this region, cyclotron emission makes a strong source of radiation, but one with a broad linewidth. The linewidth can be reduced by using the purest sample possible. An interesting possibility is to produce cyclotron emission from a sample under pressure, which would further reduce the linewidth. We have also seen, especially in the pure Ge sample investigated, that at the lowest electric fields where we can still see emission the linewidth begins to narrow quite sharply. Linewidths of  $\omega\langle\tau\rangle \sim 90$  were obtained in Ge at electric fields less than about 200 V/cm. In this region, it would be possible to use cyclotron emission as a source for spectroscopic studies, where a resolution no greater than  $.4 \text{ cm}^{-1}$  is required.

We have also seen cyclotron resonance in the same Ge sample, using pulsed electric fields of the same order as those used in emission. Because the experiments were done at different frequencies, the linewidths were considered in terms of  $\langle\tau\rangle$  rather than  $\omega\langle\tau\rangle$ . We found that the cyclotron resonance lines were narrower than the emission lines by a factor of about eight. We could explain this difference in linewidths by considering the dominant broadening mechanisms at each frequency. In cyclotron resonance, we found the

broadening could be accounted for by the theory of acoustic phonon scattering given an electron temperature of about  $50^{\circ}\text{K}$ , and that we would not expect the broadening due to non-parabolicity to have much effect as this would require a temperature of over  $1000^{\circ}\text{K}$ . In cyclotron emission we found the opposite: the linewidths could be explained as broadening due to non-parabolicity given an electron temperature of about  $90^{\circ}\text{K}$ , but that the temperature would need to be about  $3000^{\circ}\text{K}$  to account for the linewidth by acoustic phonon scattering. We also made a rough estimate of the electron temperature, and found that temperatures of  $10 - 100^{\circ}\text{K}$  would be expected.

Another part of this project dealt with laser annealing in semiconductors. This has been shown to be a useful method of removing surface damage caused by ion-implantation. We have done transmission and reflection experiments to investigate the properties of laser annealed silicon and GaAs samples, and we have developed a computer program to calculate reflection and transmission spectra. This program indicated that the plasma frequency in Si would be out of the range of our apparatus, but we did see a change in the interference fringe spacing in transmission which indicated a change in optical thickness after annealing of about 1%. We have measured the plasma frequency in one GaAs sample to be  $450\text{ cm}^{-1}$ , which, if we assume 10% electrical activity, gives an implantation depth of  $.5\text{ }\mu\text{m}$ . This is of the order we would expect, given the high implantation energy.

Finally, we have attempted to introduce vacancies into a GaAs sample by thermal annealing in order to investigate whether a certain line in the central-cell structure of GaAs is due to vacancies. The resulting spectra indicate that the line could be there, but the matter needs further investigation.

Appendix A: Method of finding detector field.

Since the frequency of the  $1s - 2p^-$  impurity transition is magnetic field-dependent, it is necessary to find the magnetic field at the detector. From the separation and relative intensities of the two detector peaks seen in the cyclotron emission experiments, it can be assumed that they correspond to the  $1s - 2p^-$  and  $1s - 2p^0$  impurity transitions. By comparing the separation of the peaks at different detector positions, it is possible to estimate the field the detector experiences at the different positions. The frequency for the different detector heights is found from figure a. (6). The results are summarized below.

Detector height above field center.	$\frac{B(2p^0)}{B(2p^-)}$	Estimate of $B_{det}$	$\bar{\nu}_{det}(2p^-)$	$x = \frac{B(d)}{B(e)}$
<u>12 T magnet</u>				
28 cm (low field)	1.124	.7 T	$33 \text{ cm}^{-1}$	.24
(high field)	1.250	2.2	32.5	
25	1.18	1.5	32.5	.51
18	~1.2	2.0	32.5	.67
<u>6 T magnet</u>				
18 cm	1.053	.2 T	34	.054
14	1.085	.5	33.5	.143

It is best to do the cyclotron emission experiments with the detector in a magnetic field of one Tesla or more, as at these fields the frequency is approximately constant.

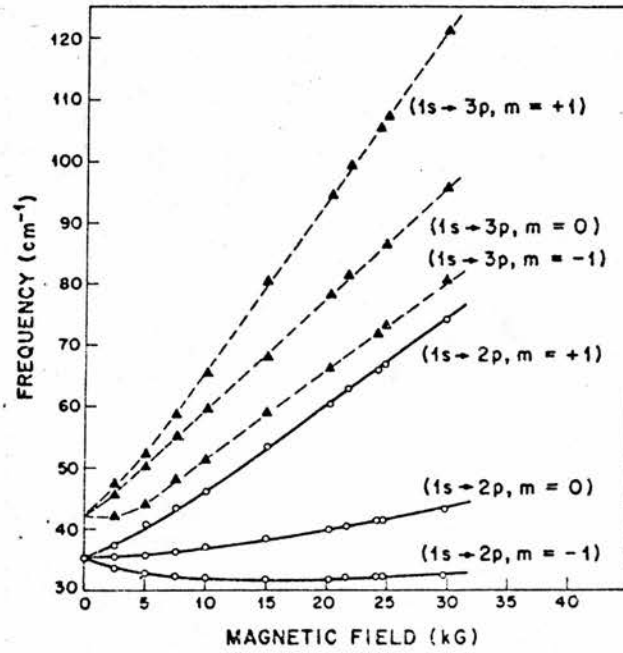


FIG. 2. Energies of the (1s → 2p) and (1s → 3p) transitions as a function of magnetic field.

Figure a. Frequency of 1s - 2p and 1s - 3p impurity transitions in GaAs versus magnetic field.

## References

### Sections 1-6: Cyclotron Emission

1. Bridges, T. J., Nguyen, V. T., Applied Physics Letters 23, 107, (1973).
2. Yang, K. H., et. al., Appl. Phys. Lett. 23, 669, (1973).
3. Aggarwal, R. L., et. al., Appl. Phys. Lett. 23, 329, (1973).
4. Kohn, W., Solid State Physics 5, 257, (1957).
5. Cooke, R. A., et. al., J. Physics D: Appl. Phys. 11, 945, (1978).
6. Stillman, G. E., et. al., Solid State Communications 7, 921, (1969).
7. Lax, B., Quantum Electronics, (Columbia University Press), 428, (1960).
8. Gornik, E., Phys. Rev. Lett. 29, 595, (1972).
9. Kobayashi, K. L., et. al., Phys. Rev. Lett. 30, 702, (1973).
10. Gornik, E., Optics and Laser Technology 7, 121, (1975).
11. Gornik, E., J. Magnetism and Magnetic Materials 11, 39, (1979).
12. Gornik, E., Int. Conf. Application of High Magnetic Fields in Semiconductor Physics, Oxford 1978, ed. J. F. Ryan, 329.
13. Dornhaus, E., et. al., Proc. 12<sup>th</sup> Int. Conf. Physics of Semiconductors, Stuttgart 1974, 1157.
14. Lindemann, G., et. al., Inst. Phys. Conf. Ser. No. 56, chapter 8, 631, (1981).
15. Gornik, et. al., Appl. Phys. Lett. 29, 169, (1976).
16. Gornik, E., Tsui, D. C., Phys. Rev. Lett. 37, 1425, (1976).
17. Gornik, E., et. al., Infrared Physics 16, 109, (1976).
18. Yamada, E., Kurosama, T. J., J. Phys. Soc. Japan 34, 603, (1973).
19. Partl, H., et. al., J. Phys. C: Solid State 11, 1091, (1978).
20. Lax, B., et. al., Physica 20, 818, (1954).
21. Smith, R. A., Semiconductors, (Cambridge University Press), chap. 5, 1959.
22. Hindley, N. K., Phys. Stat. Sol. 7, 67, (1964).
23. Fukai, M., et. al., J. Phys. Soc. Japan 19, 30, (1964).

24. Bagguley, D. M. S., et. al., Proc. Royal Society A (GB) 262, 340, (1961).
25. Muller, W., et. al., Solid State Electronics 21, 1455, (1978).
26. Kittel, C., Intro. to Solid State Physics, 5<sup>th</sup> edition, (John Wiley & Sons), chap. 8, 1976.
27. Herman, F., et. al., II-VI Semiconducting Compounds, 1967 Inter. Conf., New York, ed. D. G. Thomas.
28. Seeger, K., Semiconductor Physics, (Springer-Verlag), 1973.
29. Stillman, G. E., et. al., Proc. 11<sup>th</sup> Conf. on Physics of Semiconductors, Warsaw, 1973, p. 863.
30. Tyssen, E., et. al., Solid State Comm. 17, 1459, (1975).
31. Muller, W., et. al., Phys. Stat. Sol. (b) 86, 205, (1978).
32. Secombe, S. D., Korn, D. M., Solid State Comm 11, 1539, (1972).
33. Skolnick, M. S., et. al., Solid State Comm. 15, 1403, (1974).
34. Faulkner, R. A., Phys. Rev. 184, 713, (1969).
35. Bagguley, D. M. S., et. al., Physics Letters 1, 111, (1962).
36. Larsen, D. M., Phys. Rev. B 8, 535, (1973).
37. Fraser, D., Physics of Semiconductor Devices, (Oxford University Press) 1977, chap. 3.
38. Koenig, S. H., et. al., Phys. Rev. 128, 1668, (1962).
39. Ousset, J. C., et. al., J. Phys. C 9, 2803, (1976).

## References

### Sections 7-8: Laser Annealing

1. Antonenko, A. K., et. al., J. Phys. D: Appl. Phys. 11, 945, (1978).
2. Hill, C., Allen Clark Res. Centre, Plessey Res. (Caswell), Ltd.
3. Hill, C., *ibid.*
4. White, C. W., et. al., Science 204, 461, (1979).
5. Cullis, A. G., et. al., J. Phys. E: Sci. Instrum. 12, 688, (1979).
6. White, C. W., *ibid.*
7. Auston, D. H., et. al., Appl. Phys. Lett. 33, 437, (1978).
8. Antonenko, A. K., *ibid.*
9. Kachurin, G. A., Sov. Phys. Semicond. 9, 946, (1975).
10. Khaibullin, I. B., et. al., Sov. Phys. Semicond. 11, 190, (1977).
11. Gat, A., et. al., Solid State Tech., 59, (1979).
12. Celler, K., et. al., Appl. Phys. Lett. 32, 464, (1978).
13. Hooper, R. C., et. al., Solid State Elec. 8, 831, (1965).
14. Barnes, P. A., et. al., Appl. Phys. Lett. 33, 965, (1978).
15. Cooke, R. A., et. al., J. Phys. D: Appl. Phys 11, 945, (1978).
16. Hester, R. K., et. al., Phys. Rev. B 10, 4262, (1974).
17. Edmond, J. T., J. Appl. Phys. 34, 1428, (1960).
18. van der Pauw, L. J., Phillips Res. Reports 13, 1, (1958).
19. Sealey, B. J., et. al., Symp. on Laser-Solid Interactions and Laser Processing, Boston 1978.
20. Heavens, O. S., Optical Prop. of Thin Solid Films, (Butterworths Publ. Ltd.), chap. 4, 1955.
21. Kachare, A. H., et. al., J. Appl. Phys. 47, 4209, (1976).